A COLLOIDAL NANOPARTICLE FORM OF INDIUM TIN OXIDE:

SYSTEM DEVELOPMENT AND CHARACTERIZATION

A Dissertation
Presented to
The Academic Faculty

by

Richard Allen Gilstrap Jr.

In Partial Fulfillment
of the Requirements for the Degree
Doctor of Philosophy in
Materials Science and Engineering

Georgia Institute of Technology
May 2009

A COLLOIDAL NANOPARTICLE FORM OF INDIUM TIN OXIDE:

SYSTEM DEVELOPMENT AND CHARACTERIZATION

Approved by:

Dr. Christopher J. Summers, Chairman
School of Materials Science and Engineering
Georgia Institute of Technology

Dr. Rina Tannenbaum
School of Materials Science and Engineering
Georgia Institute of Technology

Dr. Ian T. Ferguson
School of Electrical and Computer Engineering
Georgia Institute of Technology

Dr. Brent K. Wagner
Georgia Tech Research Institute
Georgia Institute of Technology

Dr. Hamid Garmestani
School of Materials Science and Engineering
Georgia Institute of Technology

Date Approved: March 5, 2009

This work is dedicated to my late parents, Richard and Ann Gilstrap.

ACKNOWLEDGEMENTS

I would like to express my sincere gratitude to my thesis advisor, Dr. Christopher J. Summers, for his guidance and support throughout the course of my research. His innate curiosity of the physical world around us has been a source of inspiration. I also wish to thank my committee members, Drs. Ian T. Ferguson, Hamid Garmestani, Rina Tannenbaum, and Brent K. Wagner. Each has offered me invaluable guidance of both a theoretical and often, personal nature. Additional thanks to Drs. Meilin Liu, Zhong Lin Wang, and Thomas H. Sanders Jr. for the many discussions about specific topics and the general path of research work. A wealth of assistance were offered me by Drs. Hisham Menkara, Wusheng Tong, and Wounjhang Park over the last several years. The ability to work along side these seasoned scientists during my course of graduate study was indeed a rare opportunity. A special acknowledgement goes to Phillip Graham for the countless discussions about all things materials science. On that note, I would also like to thank the wide variety of Georgia Tech students who have contributed to my educational and research experience. Special thanks to Susan Bowman for calling in a variety of favors on my behalf. Lastly, I must express my most sincere and deep thanks to Tatiana Toteva for her unwavering support, encouragement, and inspiration.

TABLE OF CONTENTS

LIST OF TABLES

LIST OF FIGURES

SUMMARY

A logical progression from the maturing field of colloidal semiconductor quantum dots to the emerging subclass of impurity-doped colloidal semiconductor nanoparticles is underway. To this end, the present work describes the formation and analysis of a new form of Tin-doped Indium Oxide (ITO). The form is that of a colloidal dispersion comprised of pure-phase, 4-6 nanometer ITO particles possessing an essentially single crystalline character. This system forms a non-agglomerated, optically clear solution in a variety of non-polar solvents and can remain in this state, at room temperature, for months and potentially, years. ITO is the most widely used member of the exotic materials family known as Transparent Conductive Oxides (TCOs) and is the primary enabling material behind a wide variety of opto-electronic device technologies.

Material synthesis was achieved by initiating a series of interrelated nucleophilic substitution reactions that provided sufficient intensity to promote doping efficiencies greater than 90% for a wide range of tin concentrations. The optical clarity of this colloidal system allowed the intrinsic properties of single crystalline ITO particles to be evaluated prior to their use in thin-films or composite structures. Monitoring the temporal progression of n-type degeneracy by its effects on the optical properties of colloidal dispersions shed light on the fundamental issues of particle formation, band filling (Burstein-Moss) dynamics, and the very origin of n-type degeneracy in ITO. Central to these studies was the issue of excess electron character. The two limiting cases of ***entirely free*** and ***entirely confined*** electron motion were evaluated by application of bulk-like band dispersion analysis and the effective mass approximation, respectively.

This provided a means to estimate the number of excess conduction band electrons present within an individual particle boundary. The ability to control and optimize the level of n-type degeneracy within the colloidal ITO nanoparticle form by compositional variation was also demonstrated. A key to the widespread adoption of a new material by industry is an ability to produce multi-gram and perhaps, kilogram quantities with no significant sacrifice in quality. Accordingly, a modified synthesis process was developed to allow for the mass production of high-quality colloidal ITO nanocrystals.

CHAPTER 1

INTRODUCTION

Colloidal nanoparticle forms of inorganic materials have been a driving force in nanotechnology dating back to Michael Faraday's study of colloidal gold in 1847.[7] In fact, his observation of a size-property relationship in the system has been characterized as the birth of nanoscience.[8] This material has since been utilized in the treatment of Rheumatoid arthritis[9, 10], Altheimer's disease[11], and as a means to thermally ablate targeted cancer cells.[12, 13] These materials have also attracted attention from the microelectronics community as gold and silver nanoparticles are now used as conductive materials for inkjet printing of fine-line circuits on a variety of substrates.[14, 15]

Research and development of colloidal semiconductor nanoparticles (CSNs) has also experienced tremendous growth in the last 25 years. Much of this can be attributed to the pioneering work of Brus and Efros on CdS in the early 1980's.[16-19] Formation of this material as monodisperse colloidal solutions in the 3-10nm particle size range led to the development of quantum confinement models that can account for the size-dependent optical properties of many semiconductors. Colloidal nanoparticle forms of II-VI (CdS, CdSe, CdTe, ZnS, ZnSe, PbS, PbSe)[20-26] and III-V (InP, InAs, GaP)[27-29] systems are now utilized in a variety of fields from biomedical research to electro-optical devices.

An emerging subclass within this field of research is that of the impurity-doped colloidal semiconductor nanoparticles (doped-CSNs). Substitutional doping of a bulk semiconductor imparts tremendous functionality but, has historically been difficult to achieve in the colloidal nanoparticle form.[30] The low synthesis temperatures (<300C)

typically employed simply do not provide sufficient energy to promote homogeneous bulk diffusion of impurity atoms throughout the crystalline lattice. The development of effective synthesis routes to achieve high quality doping in these nano-structures has become a focus of many research groups and is a major component of the present dissertation work. Xiaogang Peng's group has been very successful in the development of synthesis routes to emissive materials such as Cu-doped and Mn-doped zinc selenide.[31-35] Their specific use of a colloidal epitaxy approach ensures that essentially all particles in solution contain deeply positioned dopants, far from non-radiative surface trap states. This enables both systems to operate efficiently at temperatures well above 250 ˚C; a performance unmatched by undoped CSNs and many bulk powder phosphors as well. Daniel Gamelin's group has similarly made important contributions to the growing field of spintronics through their focus on colloidal nanoparticle forms of diluted magnetic semiconductors (DMSs). Synthesis of ZnO incorporating a variety of dopants (Ni, Co, Mn) has led to the observation and quantitative study of giant Zeeman effects and high-temperature Ferromagnetism.[36, 37] The production of high quality doped semiconductors in the colloidal nanoparticle form can lead to advances in technology and a deeper understanding of the fundamental size-dependent physics associated with these material systems.

The aim of this dissertation work has been to develop and characterize a colloidal nanoparticle form of an important doped semiconductor material, Indium Tin Oxide (ITO). This was motivated by a desire to expand the field of doped-CSNs into the materials class commonly referred to as Transparent Conductive Oxides (TCOs). As the name implies, TCO's combine the seemingly contradictory properties of visible

wavelength transparency with metal-like, free electron conductivity.[38] Conductivity in a transparent solid is achieved by the degenerate doping of a wide band gap (>3eV) semiconductor. The metal oxides of Cd, In, Zn, Sn, Ga, and their various alloys have proven reliable systems for this purpose.[1] Of all the TCOs reported since the first thin film example in 1907,[39] ITO is by far the most successful. Thin film versions of this material have been used as anti-static and defrosting coatings for aircraft, reflective coatings for architectural glass, and transparent electrodes for both solar cells and flat panel displays.[40-43] In fact, it is estimated that over 50% of the Indium metal mined each year, finds its way into display devices.[42, 44]

Successful inkjet printing of conductive metal nanoparticles has driven the search for solution-dispersible forms of TCO nanoparticles as well.[45] ITO nanoparticle synthesis has previously been achieved by a variety of techniques (co-precipitation[46, 47], solvothermal[48], micro-wave assisted[45], etc…). However, varying degrees of agglomeration were observed in each case and particle morphology (size and size-distribution) was often difficult to control. Homogeneous dispersion in solution, high crystallinity, and size less than 10nm diameter are key characteristics for suitable ITO inks.[45] The synthesis process developed in this dissertation work produces an ITO system that displays these specific properties and is among the most advanced yet reported. The colloidal system is composed of <10nm diameter ITO particles which display an essentially, single-crystalline character. They are dispersible in a variety of non-polar solvents and show no signs of agglomeration even after one year in solution at room temperature. The majority of what is known about the ITO material system has been gathered from polycrystalline thin films deposited by various sputter-coating

procedures. Among samples made with the same ITO sputter target composition, an extremely wide variation in electro-optical properties of the resultant films are observed.[49, 50] Sputter procedure and associated process parameters (pO_2, temperature, deposition rate, etc…) often appear to have a greater influence on film quality than the specific sputter target used for deposition. The ITO nanoparticle system developed in the present work forms a stable, optically transparent, colloidal solution of single crystals from the very instant of reaction initiation. This has provided the unique opportunity to investigate intrinsic property evolution and fundamental physics of the particles prior to their application as a thin film or composite filler. The ability to analyze and optimize the intrinsic properties of a colloidal ITO source material prior to its industrial use may be of great benefit. A key to the widespread adoption of a new material by industry is an ability to produce multi-gram and perhaps, kilogram quantities with no sacrifice in quality. The process must be rapid, cost-effective, and impart a minimum of environmental impact. Therefore, an additional process was developed to rapidly produce multi-gram quantities of high-quality colloidal ITO with an acceptable broadening of particle size distribution.

Essential background required for an understanding of experimental results is presented in chapter two where the fundamental physics of transparent conductive oxides, with specific emphasis on ITO, are discussed. Additionally, the potential influence of quantum confinement effects due to the small particle size produced in this work is described. Analysis equipment and procedures utilized are found in chapter three. Details regarding development and implementation of the method utilized for ITO synthesis are presented in chapter four. As the process was a modification of work done

on undoped colloidal indium oxide, this data is briefly discussed as well. In order to verify the production of ITO, basic properties of the system were determined by composition, phase, morphology, and optical analysis. Chapter five presents investigations into the generation and control of degeneracy in colloidal ITO. This work provides information on particle formation, conduction band filling, and the very origin of free-electrons in the material. Basic relationships between composition, structure, morphology, and functional properties are established as well. Chapter six describes the procedure to produce large quantities of high-quality colloidal ITO discussed earlier. This is important for the potential use of any doped colloidal semiconductor nanoparticle system on an industrial scale. A summary of experimental results and discussion of important conclusions is found in chapter seven.

CHAPTER 2

BACKGROUND

2.1 Introduction

The principle aims of this dissertation have been to develop a colloidal ITO nanoparticle system, investigate intrinsic properties of the single crystals of which it is composed, and then establish some fundamental composition-structure-property relationships. While structural investigations involved a variety of techniques, property evaluation relied primarily on the optical analysis of colloidal dispersions. This approach was taken in an attempt to evaluate the intrinsic properties of essentially single-crystalline particles prior to their application as a thin film or composite filler. This background section begins with a presentation of the general physics associated with transparent conductors and specifically, how electron degeneracy is accomplished in ITO. Following this essential foundation, the discussion then moves to a detailed treatment on the interaction of electromagnetic radiation with the ITO lattice and how the quantum confinement of charge carriers may influence this process.

2.2 Transparent Conductivity

Although partial transparency can be obtained in thin metallic films, high transparency with simultaneous high conductivity requires significant degeneracy within a transparent, wide band gap (>3eV) semiconductor. This is typically accomplished by the controlled introduction of non-stoichiometry and/or appropriate dopants.[50] Degeneracy is formed when a dopant species with higher or lower valence than that of the host lattice atoms is

incorporated such that the resultant charge imbalance is neutralized by an abundance of either electrons (n-type) or holes (p-type). This compositional shift serves to pull the Fermi energy E_f towards the conduction or valence band for the case of n-type or p-type systems, respectively. This is displayed by the representative band model in Figure 2.1 for an n-type material.[2] Doping results in the formation of a donor energy level just below the conduction band minimum and its depth E_d, is dependent upon the concentration of electrons and their effective mass in the material of interest. This energy level is composed of impurity atom potentials along with their loosely bound charge compensating electrons. The spatial influence of this potential can be estimated by considering the Bohr radius of the electrons as,

$$a^* = \left(\frac{\varepsilon_\infty}{m_c^*}\right)\left(\frac{\hbar^2}{\pi e^2}\right) \qquad \text{Equation 2.1}$$

where, ε_∞ is the high frequency dielectric constant of the host lattice, $\hbar$ is the reduced Planck's constant $(h/2\pi)$, e is the electron charge, and m_c^* is the electron effective mass. The effective mass of electrons (holes) represents the apparent mass of a free electron (hole) as it moves throughout the lattice potential and is normally expressed in terms of the mass of an electron in vacuum, i.e. $9.11\times10^{-31}\,kg$. There is good acceptance that $\varepsilon_\infty = 8.9\,\varepsilon_0$ and $m_c^* = 0.35\,m_e$ in ITO and thus, the Bohr radius of a free electron in this material can be estimated at ~1.35nm.[38, 49]

At low doping concentration, impurity potentials and their associated electron wavefunctions do not interact and the material will only yield moderate conductivity at

room temperature where thermal ionization of donor electrons occurs. As the concentration increases, states of adjacent impurities interact, split, and ultimately form a band of impurity potentials also shown in Figure 2.1.[2] Upon further doping, the impurity potentials begin to overlap as displayed, which allows electrons to more easily propagate either by hopping conduction or through thermal emission over the potential barrier.[2] The activation energy is thus reduced by increased doping and, at a critical point, will become zero to allow finite conductivity at a theoretical zero degrees Kelvin. This degree of conductivity is indicative of a material that has undergone a semiconductor-to-metal transition.

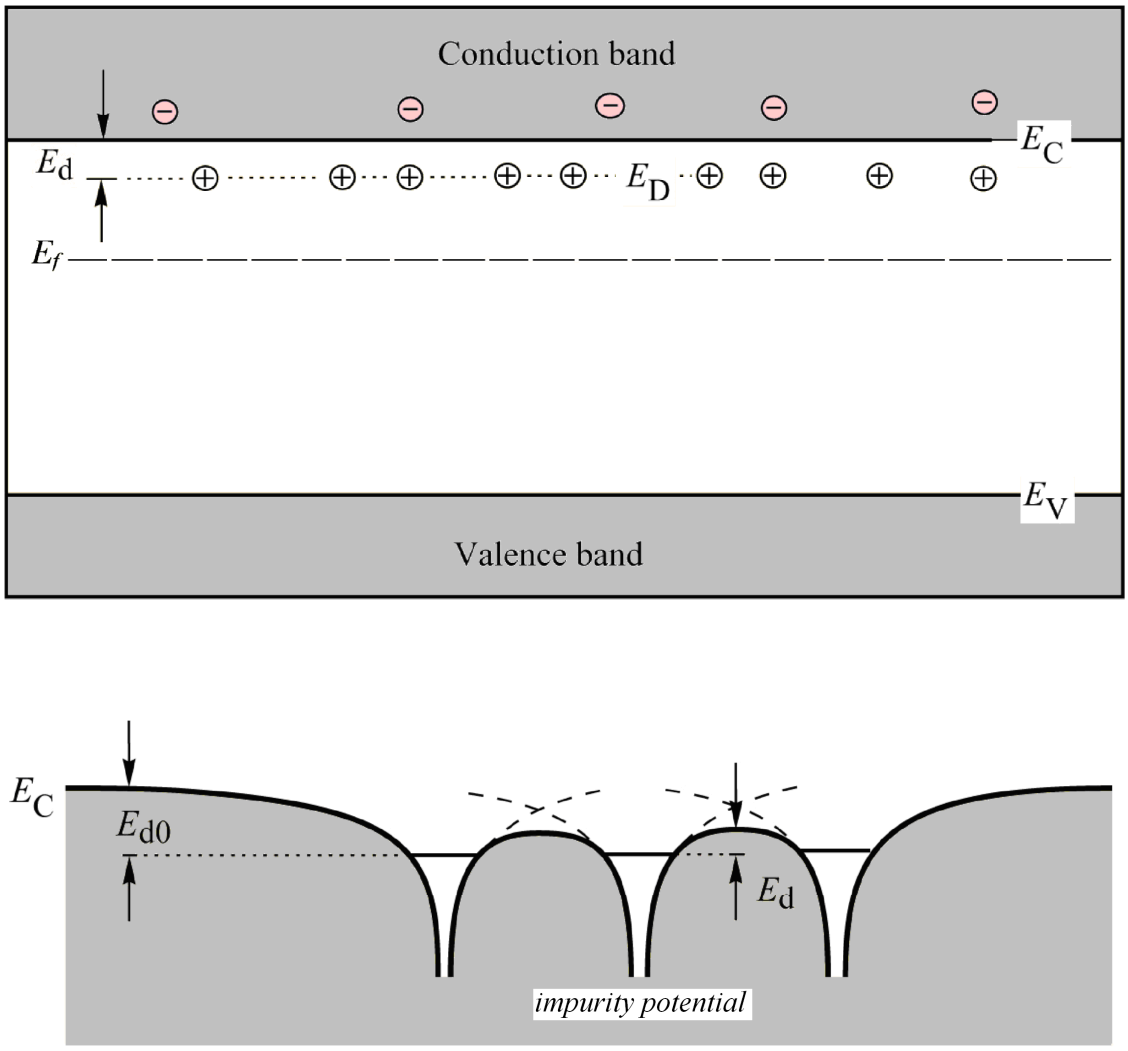

Figure 2.1: Simplified band diagram of an n-type degenerate semiconductor (top) and its associated impurity potentials (bottom). The distance between the electron donor level and conduction band minimum is characterized by the activation energy E_d in electron volts.[2] Degenerate doping has pulled the Fermi level E_f towards the conduction band minimum and created an overlap of the impurity potentials (bottom).

The specific point at which this transition occurs can be determined by calculation of the Mott critical electron donor concentration (N_c).[38, 51] Substitutionally incorporated impurities occupying a simple cubic lattice are spaced $N_D^{-1/3}$ apart.[2] As previously discussed, the transition to a metallic property state occurs when their potential wavefunctions overlap and this will theoretically occur at a separation distance comparable to twice the Bohr radius (a_B^*) of their associated electrons. Due to the random placement of impurities, a Poisson distribution is assumed and the critical electron concentration is now as,

$$2a_B^* = \frac{3}{2\pi} N_c^{-1/3} \qquad \text{Equation 2.2}$$

As will be discussed shortly, the incorporated impurity concentration and actual free electron concentration begin to deviate when the Sn content is increased over just 1% in ITO. Rearrangement of this expression yields the Mott critical free electron concentration for a semiconductor to metal transition,

$$a_B^* N_c^{1/3} \approx 0.24 \qquad \text{Equation 2.3}$$

Using the previously determined Bohr radius of 1.35nm, this relation yields a critical free electron concentration N_c in ITO of $5.62x10^{18} cm^{-3}$. At this point, the donor impurity band will begin to merge with the conduction band, pull the Fermi level above the conduction band minimum, and cause the activation energy E_d to effectively become zero.

Screening of impurity potentials will also reduce the activation energy E_d as a high free-electron concentration reduces electrostatic potentials by spatial redistribution of the charge carriers.[2] This redistribution results in a locally higher concentration of negative charge and these species can effectively screen an impurity potential fluctuation. If the assumption is made that a potential changes very little over the length scale of an electron wavelength, then electrons will experience only the potential at their own locations.[2] The total energy of electrons will now follow a classical sum of potential and kinetic energies,

$$E = eV(r) + \frac{\hbar^2 k^2}{2m_e^*} \qquad \text{Equation 2.4}$$

where, k is a wave number associated with the conduction band dispersion. The expression for this parameter will be fully derived within an upcoming discussion on the optical properties of ITO. Note that bound valence electrons still require energy greater than the semiconductor's band gap for promotion to an available conduction band state and therefore, these materials remain transparent to lower energy frequencies of light. Any transition within the band gap of an oxide host will prevent this transparency and therefore, only cations with filled d-shells are utilized ($3d^{10}$ Cu^+, Zn^{2+}, Ga^{3+} and $4d^{10}$ Ag^+, Cd^{2+}, In^{3+}, Sn^{4+}).[1, 50] Highly dispersed conduction (n-type) or valence (p-type) bands are also desired because they lead to higher electron or hole mobilities, respectively.[1]

Existing TCOs formed by the above elements may be classified into families by their structures as shown in Table 2.1.[1] The first has cations that are tetrahedrally coordinated by oxygen and is n-type in character. ZnO is the only known oxide to possess this coordination exclusively. The second has cations in octahedral coordination and is also

n-type in character. This represents the largest family of TCOs with ITO as its most notable member. The third has cations in linear coordination with oxygen and is p-type in character. Included are $CuAlO_2$ and the closely related Cu- and Ag-based delafossites. $SrCu_2O_2$ is also found within this structure group.

Table 2.1: Families of transparent conductive oxides.[1]

Cation Coordination	Carrier Type	Examples
Tetrahedrally-coordinated	n-type	ZnO
Octahedrally-coordinated	n-type	CdO, In_2O_3, SnO_2, $CdIn_2O_4$, Cd_2SnO_4
Linear-coordination	p-type	$CuAlO_2$, $SrCu_2O_2$

It is often observed that the free electron concentration (n) within a transparent conductor varies with impurity dopant concentration (N_D) as displayed in Figure 2.2. Whereas the majority of dopant impurities at low concentration are electrically active, higher doping concentrations can favor the formation of dopant pairs and precipitates that may not be active. The chemical bonding in these precipitates is generally different from that of the host and as a result, free-electron formation may be compromised.[2] A very similar plot displaying the estimated carrier concentration of colloidal ITO nanoparticles produced in this dissertation work is presented in chapter five.

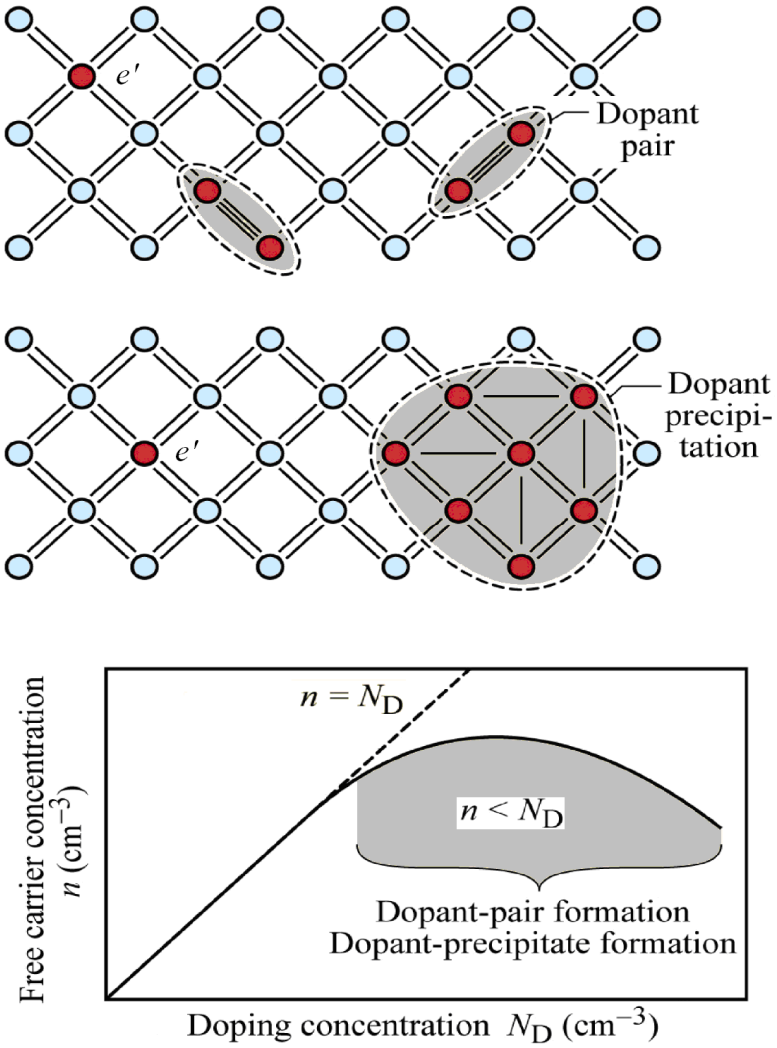

Figure 2.2: Effects of impurity quenching in an n-type semiconductor. Impurity pairs and/or higher order clusters may serve to limit free electron activity within the host lattice. The lower plot shows a relationship between carrier concentration and impurity dopant concentration often observed in such systems.[2]

2.3 Electron Degeneracy in Indium Tin Oxide

The basic mechanisms of how electron degeneracy is generated in n-type transparent conductors, are now reasonably well understood. The high conductivity of these materials is produced by the combination of intrinsic lattice anion vacancies and extrinsic impurity donor doping.[38] Each of these defects promotes the release of free electrons to compensate the induced charge imbalance. Generation of free electrons in the case of ITO is heavily influenced by the In_2O_3 host lattice structure and specifically, the ability of this structure to incorporate interstitial oxygen has been proposed as the predominant factor.[1, 52-54]

Figure 2.3 presents the bixbyite structure of undoped indium oxide.[53] Each unit cell contains 16 units of In_2O_3 or 80 atoms in a defect free crystal. The lattice constant is reported to be 10.117Å leading to a theoretical density of 7.12g/cm^3.[3] Two types of non-equivalent indium sites are present in this structure, denoted as b-sites and d-sites in the figure. For a b-site, the separation distance between indium and oxygen atoms is 2.18Å. Oxygen atoms are positioned at the corners of a body-centered cube with two body-diagonally opposite corners unoccupied. In a d-site, the separations are 2.13, 2.19, and 2.23Å. In this case, oxygen atoms occupy positions at the corners of a body-centered cube with two face-diagonally opposite corners unoccupied. Based on this description, both indium sites can be viewed as incomplete body centered cubic structures with an indium atom located at the center and oxygen atoms at the corners. The system is similar to the fluorite structure with one fourth of the anions missing.[54]

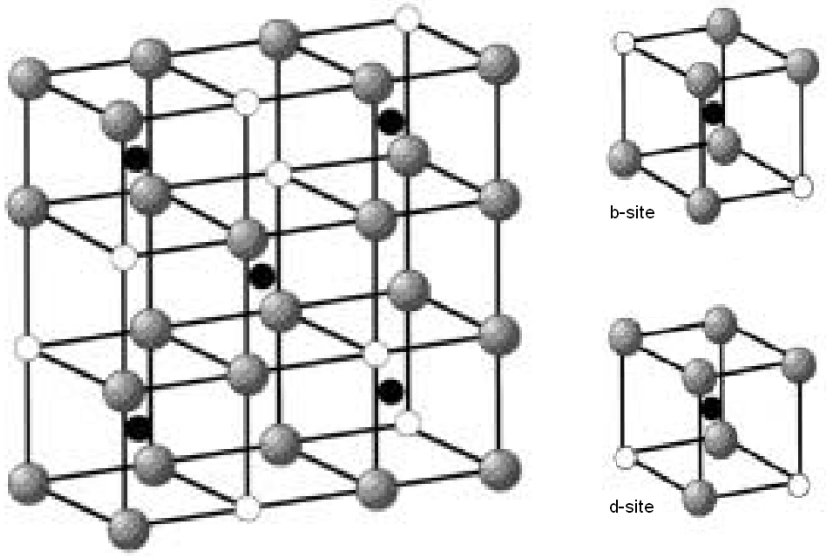

Figure 2.3: Schematic drawing of the C-type rare-earth (bixbyite) In_2O_3 structure. The gray spheres represent oxygen atoms while white spheres denote regular lattice oxygen vacancies which are inherent to the bixbyite structure. Indium atoms are displayed as black spheres.[53]

A defect model proposed by Frank and Kostlin in the early 1980's, asserts that these naturally occurring "structural oxygen vacancies" play a crucial role in the mode of free electron generation within an ITO lattice.[52] According to the Frank and Kostlin model, interstitial oxygen should be present at the unoccupied corner positions due to the substitutional doping of Sn^{4+} for In^{3+}. Interstitial oxygen incorporation will thus, lead to the formation of charge-neutral ($2Sn^{\bullet}O_i^{''}$) associates. The substitutional doping of two Sn^{4+} atoms would favor the additional incorporation of a single oxygen interstitial at a structural oxygen vacancy site to maintain overall charge neutrality. Under reducing conditions, the removal of each interstitial oxygen should release two free electrons into the lattice according to,

$$(2Sn_{In}^{\bullet}O_i^{''})^{x} \rightarrow \frac{1}{2}O_2(g) + 2Sn_{In}^{\bullet} + 2e' \qquad \text{Equation 2.6}$$

The absence of oxygen interstitials in undoped In_2O_3 and their subsequent presence in Sn doped versions of thin films has been experimentally proven through Rietveld analysis of time of flight (TOF) neutron diffraction data.[54] Under oxidizing conditions, the ratio of tin-to-oxygen interstitial ($Sn^{4+}/O_i^{''}$) was found to be ~ 2 which provided strong support to the validity of the ($2Sn^{\bullet}O_i^{''}$) associate model.[1, 54] This defect model was also used to explain the variation in free electron concentration for ITO thin films prepared using sputter targets with different tin concentrations as shown in Figure 2.4. This trend is quite similar to the dopant pair and precipitate model previously described in Figure 2.2.

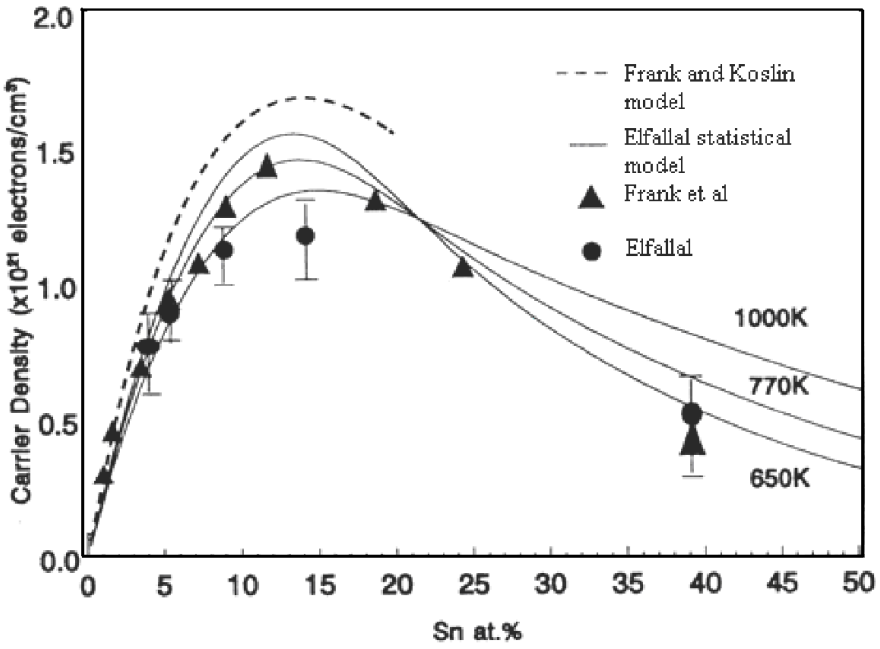

Figure 2.4: Variation of free electron concentration with the Sn content of sputter targets for two different ITO thin film materials.[3] The trend follows the concentration quenching model previously described in Figure 2.2 for a general case. A similar relationship between Sn content and estimated free electron concentration will be presented for the colloidal ITO developed in this dissertation work.

Analysis of highly reduced thin films of this type revealed the presence of a significant amount of interstitial oxygen which was strongly dependant upon the initial Sn concentration used for sample synthesis.[54] For a Sn doping concentration of 10%, approximately 50% of the oxygen interstitials appeared to be "trapped" in the otherwise reduced, ITO lattice.[54] Frank and Kostlin had originally suggested that some of the oxygen interstitials were not reducible due to the tighter bond between nearest neighbor Sn-O_i pairs.[52] As more Sn is incorporated within an ITO lattice, the density of non-reducible oxygen interstitials will increase as these nearest neighbor Sn-O_i pairs become more prevalent. Gonzales et al. later proposed that higher-order ($2Sn^{\bullet}O_i^{''}$) associate clusters played a more determining role in the concentration of non-reducible interstitial

oxygen.[54] With either defect model however, it has been proposed that as more $Sn^{\bullet}$ surrounds an oxygen interstitial, its ability to be reduced is diminished. Additional experimental support for the ($2Sn^{\bullet}O_i^{''}$) associate model in the colloidal nanoparticle form of ITO is discussed in chapter five.

2.4 Analysis of Free Electron Concentration in ITO

Beyond the successful synthesis of colloidal ITO, a major emphasis in the present work has been the study of free electron generation and control within the system. As mentioned in the introduction, the various methods of ITO thin film deposition have historically produced materials with different properties even though the same initial Sn content was utilized in sputter targets.[49, 55] The free electron concentration in thin film forms is able to be directly determined from Hall conductivity measurements that make use of the relation,[38]

$$\sigma = \mu ne = (\frac{e}{m*}\tau)ne \qquad \text{Equation 2.7}$$

where, σ is the conductivity, n is the free electron concentration, μ is the electron mobility, e is the electron charge, $m*$ is the effective mass of free electrons and, τ is the free electron scattering time. Table 2.2 presents the measured conductivity and free electron (carriers) concentration for several thin film samples made by various methods that all utilize ITO sputter targets with a tin content of 10%.[56] The spread in data very well indicates that the properties of ITO thin films become more a function of the deposition process and associated parameters than the intrinsic properties of the source material. For

this reason, the functional properties of colloidal ITO nanoparticles produced in this dissertation work are primarily determined by optical analysis of the dispersed colloidal solution. In this way, fundamental material physics of the essentially single crystal source material can be determined prior to its use in any potential applications.

Table 2.2: Typical electrical and optical properties of ITO (10% at. Sn) thin films.[56]

Deposition Technique	Thick [Å]	Hall Mobility μ_H [$cm^2V^{-1}s^{-1}$]	Carriers N[cm^{-3}]	Resist ρ[Ωcm]	Trans T_r[%]	Ref. No.
r.f. Sputtering	7,000	35	6×10^{20}	3×10^{-4}	90	[57]
r.f. Sputtering	5,000	12	12×10^{20}	4×10^{-4}	95	[58]
r.f. Sputtering	4,000	25	3×10^{20}	8×10^{-4}	-	[59]
Magnetron Sputtering	800	26	6×10^{20}	4×10^{-4}	85	[60]
d.c. Sputtering	1,000	35	9×10^{20}	2×10^{-4}	85	[61]
Reactive Evaporation	2,5000	30	5×10^{20}	4×10^{-4}	91	[62]
r.f. Sputtering	600	26	2×10^{20}	12×10^{-4}	-	[63]
Spray Pyrolysis	3,000	45	5×10^{20}	3×10^{-4}	85	[64]

2.5 Optical Properties of ITO

The optical analysis methods used in this dissertation require a thorough understanding of the interplay between an electromagnetic field and the colloidal ITO dispersion through which it travels. Due to its highly degenerate nature, this interplay involves both bound and free electrons within the lattice. Free electron concentration has a significant and measurable effect on the interaction of light with ITO and this fact constitutes the basis for over 50 years of optical analysis of the material. Figure 2.5 displays the transmission spectra of a typical thin film sample of ITO made by sputter deposition. The spectra is characterized by a transparent window in the visible (350-1000nm) and strongly absorbing regions in the deep UV (<300nm) and far infrared (>1400nm).

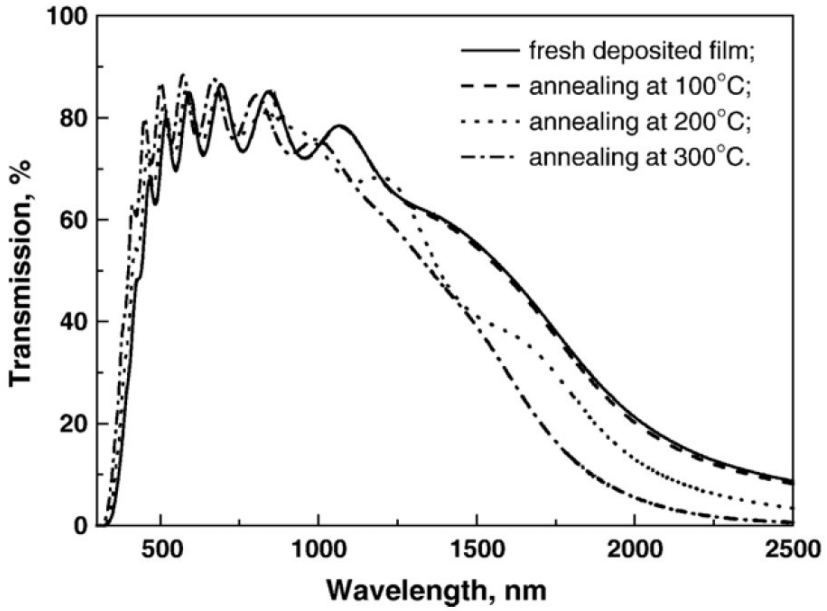

Figure 2.5: Transmission spectra of a typical ITO thin film sample.[65] The material is characterized by an optically transparent window spanning the entire visible range and much of the infrared.

A detailed explanation of how these spectral features are influenced by the free electron concentration within an ITO lattice follows. This will begin with a discussion of the interaction of infrared light with free electrons and then move to a description of the UV band gap absorption edge for this highly degenerate case. All subsequent discussion requires that light be thought of in terms of frequency ω(Hz) rather than wavelength λ(nm) as shown in the above transmission figure. This is achieved by the relation,

$$\omega = \frac{2\pi v}{\lambda} \qquad \text{Equation 2.8}$$

where, v is the phase speed of an EM wave in a material through which it travels.

2.5.1 Influence of Light on Electrons

The frequency dependence of the electric field component of light in a vacuum can be derived from a standard solution to Maxwell's equations,

$$E = E_{\circ} \cos[k(z - \omega t) + \delta] \qquad \text{Equation 2.9}$$

where, E_o is the electric field amplitude, k is the wave vector, z is the field direction, ω is the electric field's frequency, t is time, and δ is the inherent phase shift present at time t. As this electric field component of light interacts with a material's electrons, a portion of its energy is lost through absorption. When this loss is to bound electrons, the Lorentz force oscillator model is used to express the degree of electron reaction with respect to the frequency of light passed through the material. The natural frequency of oscillation ω_o for a bound electron may be modeled as a mass attached to a spring,

$$\omega_o = \sqrt{k_s / m} \qquad \text{Equation 2.10}$$

where, m is the electron mass and k_s is the spring constant of the system. Application of an electric field of the form in equation 2.9 produces a net force F_{net} on the electron as,

$$F_{net} = eE - k_s x \qquad \text{Equation 2.11}$$

where, x represents the distance which the electron is moved from its unperturbed position with respect to the positive ion core. Utilization of Newton's 2nd law leads to,

$$m\frac{d^2x}{dt^2} = eE - k_s x \qquad \text{Equation 2.12}$$

When equations 2.10 and 2.12 are substituted into equation 2.9, an analytical expression for the effect of light with frequency ω on a material's bound electrons with natural frequency ω_o is produced and is of the form,

$$\frac{d^2x}{dt^2} + \omega_o^2 x = \frac{eE_o}{m}\cos(kz - \omega t) \qquad \text{Equation 2.13}$$

A standard solution to this expression is of the form,

$$x = \frac{eE_o}{m(\omega_o^2 - \omega_2)}\cos(kt - \omega t) \qquad \text{Equation 2.14}$$

If the interaction is with free electrons in a metal, a very similar expression is derived,

$$x = \frac{eE_o}{m(\omega^2 + i\gamma\omega)} \qquad \text{Equation 2.15}$$

This relation originates from a combination of the Lorentz oscillator model and Drude theory which treats free electrons as a plasma of weakly interacting, negatively charged species.[66] Unlike the bound electron case of equation 2.14, this new expression lacks any restoring force terms because, electrons are entirely free. The γ term is present to account for frictional forces that act to dampen the movement of electrons and is equal to $1/\tau$. In

this case, τ is a frequency-dependent relaxation time, i.e. the mean time between successive electron collisions. Although individual free electrons may not experience the classic dipole behavior of the bound case, the entire plasma ensemble is able to be polarized and is expressed as,

$$P = -nex \qquad \text{Equation 2.16}$$

where, P is the polarization and again, n is the free electron concentration. For the case of degenerate semiconductors, this free electron plasma is also considered to be a collection of weakly interacting, negatively charged species as in classical Drude theory.[67] The only significant difference being that an effective electron mass associated with the semiconductor material of interest is now required.

2.5.2 Drude Theory Approach to the ITO Reflectance Edge

With this general foundation in place, a detailed description of the interaction of light with ITO in the visible to infrared range as displayed in Figure 2.5 can be presented. The interaction of free electrons with an electromagnetic field influences the relative permittivity, ε, of the material.

$$\varepsilon \equiv \varepsilon' - i\varepsilon'' = (N - iK)^2 \qquad \text{Equation 2.17}$$

In this expression, N and K are the refractive index and extinction coefficient of the material, respectively. The permittivity is also a frequency dependent function that can be written as,

$$\varepsilon(\omega) = \varepsilon_{\infty} - \frac{ne^2}{m_c^*} \frac{1}{(\omega^2 - i\omega\gamma)} \qquad \text{Equation 2.18}$$

where ε_{∞}, m_c^*, e, and n are the high frequency dielectric constant, effective electron mass, its charge, and the density of electrons, respectively. The real (ε') and imaginary (ε") components can therefore, be written as,

$$\varepsilon' = N^2 - K^2 = \varepsilon_{\infty}(1 - \frac{\omega_p^2}{\omega^2 + \gamma^2}) \qquad \text{Equation 2.19}$$

$$\varepsilon'' = 2NK = \frac{\gamma}{\omega} \frac{\varepsilon_{\infty}\omega_p^2}{\omega^2 + \gamma^2} \qquad \text{Equation 2.20}$$

where ω_p is the free electron plasma frequency given by

$$\omega_p = (ne^2 / \varepsilon_0 \varepsilon_{\infty} m_c^*)^{1/2} \qquad \text{Equation 2.21}$$

With $\varepsilon_0 = 8.854 \times 10^{-12}$ F/m denoting the permittivity of free space, equation 2.18 can now be rewritten as:

$$\varepsilon(\omega) = (N - iK)^2 = \varepsilon_\infty \left[1 - \frac{\omega_p^2}{\omega^2 + \gamma^2} - i \frac{\omega_p^2 (\gamma / \omega)}{\omega^2 + \gamma^2} \right] \qquad \text{Equation 2.22}$$

Equation 2.22 is the principal controlling expression with the plasma frequency ω_p marking a transition point between spectral regions of optical transparency and free electron reflectivity.

2.5.3 Transparent Region

Transparency is observed for light with high incident frequencies ($\omega > \omega_p, \gamma$) in the limit where $K \to 0$. Using this approximation, equation 2.22 can be written as:

$$\varepsilon(\omega) = \varepsilon_\infty \left[1 - \frac{\omega_p^2}{\omega^2} - i \frac{\gamma \omega_p^2}{\omega^3} \right] \qquad \text{Equation 2.23}$$

In this limit the refractive index and extinction coefficient take the following forms:

$$N(\omega) \cong \varepsilon_\infty^{1/2} \left[1 - \frac{\omega_p^2}{\omega^2} \right]^{1/2} \qquad \text{Equation 2.24}$$

$$K(\omega) \cong \varepsilon_\infty^{1/2} \left[\frac{\omega_p^2 \gamma}{2\omega^3} \right] \qquad \text{Equation 2.25}$$

The behavior of the material in this frequency regime is that of a dielectric with the refractive index approaching $\varepsilon_\infty^{1/2}$ as ω increases.

2.5.4 Reflective Region

The low frequency (long wavelength) spectral region, where $(\omega < \omega_p, \gamma)$ and $\omega \to 0$, is typified by free electron reflectivity. In this regime, equation 2.22 is approximated as:

$$\varepsilon(\omega) = \varepsilon_\infty \left[1 - \frac{\omega_p^2}{\gamma^2} - i\frac{\omega_p^2}{\gamma\omega} \right] \qquad \text{Equation 2.26}$$

Taking the square root of $\varepsilon(\omega)$ and using the identity[68] $\sqrt{i} = e^{\frac{\pi}{4}i} = \frac{1+i}{\sqrt{2}}$,

$$\varepsilon(\omega) \approx K(\omega) \cong \omega_p \sqrt{\frac{\varepsilon_\infty}{2\omega\gamma}} \qquad \text{Equation 2.27}$$

The normal reflectance *R*, can now be written as:

$$R(\omega) = \frac{(N-1)^2 + K^2}{(N+1)^2 + K^2} \qquad \text{Equation 2.28}$$

and in the very low frequency limit, can be approximated by:

$$R(\omega) \approx 1 - \frac{2}{K(\omega)} \approx 1 - 2(2\rho\omega\varepsilon_0)^{1/2} \qquad \text{Equation 2.29}$$

This indicates that the material behaves like a perfect reflector. Figure 2.6 presents a plot of reflectivity versus complex refractive index which models the behavior of light with frequency ω as it interacts with a metal with free electron concentration n. Again, elucidation of this phenomenon in the case of a degenerately doped semiconductor such as ITO, requires that the mass of a free electron be expressed as an effective mass m_c^*, which takes into account the interaction of a free electron with the specific semiconductor lattice potential in which it is present.

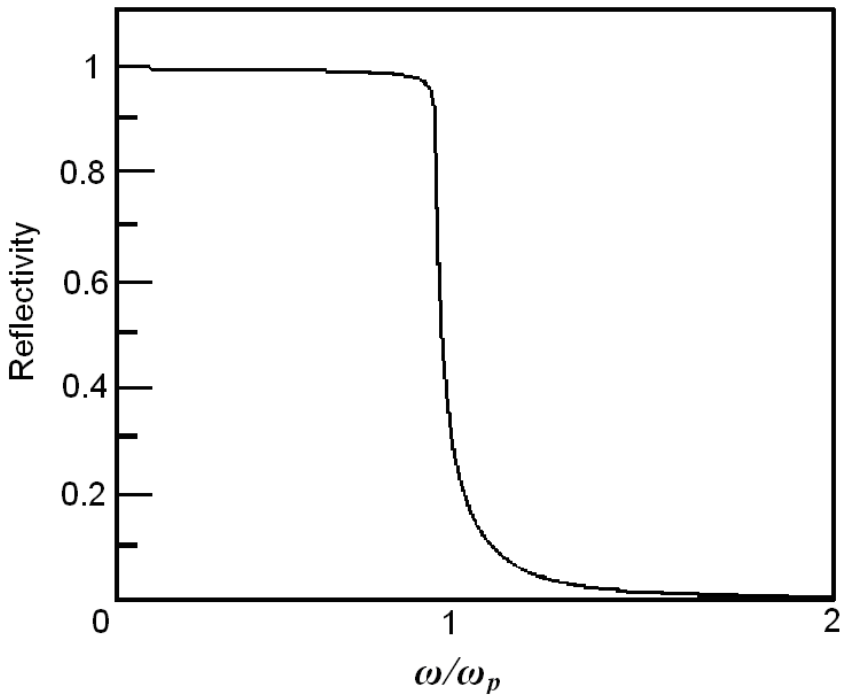

Figure 2.6: Reflectivity of an undamped free electron gas as a function of incident light frequency ω and electron plasma ensemble frequency ω_p. This behavior in a transparent conductor such as ITO leads to a long wavelength reflection edge at $\omega \leq \omega_p$.

These relations enable a quantitative explanation for the optical response of ITO to incident electromagnetic radiation in the visible to infrared region as displayed for the thin film case in Figure 2.5. When ω is greater than ω_p, the relative dielectric constant tends toward ε_∞ and the ITO thin film behaves as an almost perfect dielectric. However, when the incident light frequency ω is less than the material's intrinsic plasma frequency ω_p, the relative dielectric constant is large and negative thus, leading to light reflection. This is purely a function of the ability of a free electron plasma to oscillate with an incident electromagnetic field.[67] When the frequency is high ($\omega>\omega_p$), this free electron plasma is unable to oscillate with the field and light is transmitted. However, when the frequency is low ($\omega<\omega_p$), electron motion leads the field and light is increasingly absorbed in classic Lorentz oscillator fashion.

2.5.5 UV Absorption Edge – Apparent Band Gap of ITO

As can be seen in Figure 2.5, the spectral position of the low-wavelength ultraviolet absorption edge near ~350nm is better defined than the position of the infrared reflection edge. The precise value of this apparent band gap and its variation with free electron concentration is a major component of the analytical portion of this dissertation. The phrase "apparent band gap" has been used here to distinguish this value from the band gap of a semiconductor that does not possess free electrons in any significant concentration. The band gap of a degenerate semiconductor like ITO appears expanded relative to an undoped version of its host lattice. The degree of this expansion is a direct function of the concentration of free electrons in the lattice and has been the subject of extensive research and controversy over the last several decades.

2.5.6 The Burstein-Moss Shift

In the case of an undoped semiconductor at a theoretical zero degrees Kelvin and containing no defects (intrinsic or extrinsic), all valence electrons are properly positioned in their respective orbits. Thus, the valence band is completely filled and the conduction band is completely empty. Photo-excitation from an electromagnetic wave with energy greater than the intrinsic band gap will promote electrons from the valence band to the lowest available energy states in the conduction band (i.e., the 1s-like level). The situation becomes a bit less ideal as the temperature is raised to *RT* but, the concentration of free electrons released due to thermal vibrations is considered negligible. Impurity-induced creation of significant numbers of free electrons within the lattice will alter this ideal picture in an often dramatic fashion. As free electrons enter the conduction band, the Fermi exclusion principal dictates that available energy states must be filled from lowest to highest (1s, 1p, 1d, etc). This means that the energy required for a valence electron to enter the conduction band is rapidly increased because the only available states are at higher energy and the band gap thus, appears expanded.[69] This behavior is commonly referred to as the Burstein-Moss shift and plays a dominant role in the band gap character of transparent conductors.[70, 71] Much of the analysis described in this dissertation makes use of this behavior to gain an understanding of free electron dynamics in colloidal ITO and therefore, analytical expressions for the conduction and valence bands are required. It has been determined that the band structure in ITO is essentially parabolic near the gamma point, which describes the position along the momentum axis **k** where conduction and valence bands are closest.[49, 72]

Analytical expressions for the conduction and valence band dispersions may be derived through consideration of the kinetic energy of free electrons. The propagation of a free electron with mass (m) and momentum ($p = mv$) in a vacuum can be described by classical Newtonian mechanics as,

$$E = \frac{1}{2}mv^2 = \frac{p^2}{2m} \qquad \text{Equation 2.30}$$

Taking the wave nature into account with the de Broglie relationship ($p = h\boldsymbol{k}$), the free electron kinetic energy is as,

$$E = \frac{\hbar^2 k^2}{2m} \qquad \text{Equation 2.31}$$

The wave vector $\boldsymbol{k}$ has components within the Cartesian coordinate system $\boldsymbol{k}=(k_x,k_y,k_z)$ such that each coordinate is a point in k-space with the constant energy surfaces of free electrons in k-space modeled as spheres.[2] These so called, Fermi spheres have a radius k_F, which is dependent upon free electron concentration n. The volume of such a sphere is as,

$$V_{FS} = \frac{4}{3}\pi k_F^3 \qquad \text{Equation 2.32}$$

and contains N electrons. The Pauli exclusion principal dictates that each energy state within this volume can hold at most two electrons (one spin up and the other, spin down).

Energy states may be represented as cubes in k-space with an edge length L such that the volume of a wave function within is as,

$$V_k = \left(\frac{2\pi}{L}\right)^3 \qquad \text{Equation 2.33}$$

Relating these volumes and the number of electrons within them leads to the Fermi wave number k_F as,

$$\frac{V_{FS}}{V_k} = \frac{\mathrm{N}}{2} \qquad \text{Equation 2.34}$$

$$k_F = (3\pi^2 n)^{1/3} \qquad \text{Equation 2.35}$$

Substitution of this relation into the expression for electron kinetic energy yields,

$$E(k_F) = \frac{\hbar^2}{2m^*}(3\pi^2 n)^{2/3} \qquad \text{Equation 2.36}$$

In this case, the effective mass of both electrons ($m^* = m_c^*$) and holes ($m^* = m_v^*$) take account of the lattice periodicity and control the curvature of both conduction and valence band dispersions, respectively. The effective mass is inversely proportional to the second derivative of E with respect to $\boldsymbol{k}$, and accordingly, is also inversely proportional to the curvature of the dispersion relation.[2] As previously discussed, free electrons in ITO begin to fill available conduction band states and as a result, bound

electrons require increasingly higher energy for promotion to this band. The Burstein-Moss effect will not begin until the lowest states in the conduction band become filled and this occurs at a critical free electron concentration n_c, commonly referred to as the effective conduction band density of states.[69]

$$n_c = \frac{2(2\pi m_c^* kT)^{3/2}}{h^3} \qquad \text{Equation 2.37}$$

where, h is Planck's constant, k is the Boltzmann constant, T is absolute temperature, and m_c^* is the effective mass of an electron at the bottom of the conduction band. The dispersion character of both conduction and valence bands becomes critically important when estimating the expansion effects above n_c because this dictates the rate at which available energy states are filled. Figure 2.7 presents a typical parabolic band structure and the effects of free electron release on its properties.

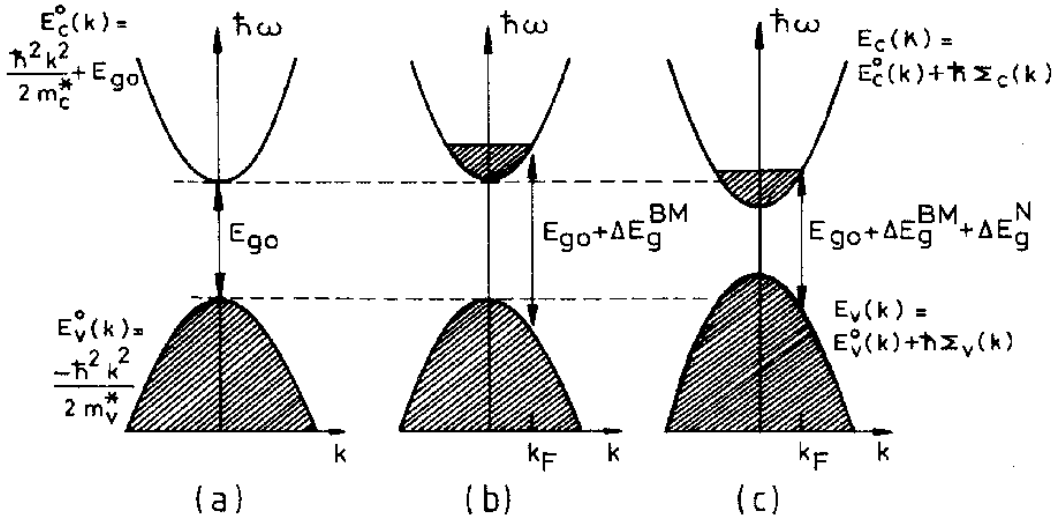

Figure 2.7: (a) Schematic band structure of a degenerate semiconductor (at ground state) typified by parabolic conduction and valence bands with band gap E_{go}. (b) Extrinsic donor doping has caused the apparent band gap to expand due to the Burstein-Moss effect. (c) Many body interactions beyond the semiconductor-to-metal transition cause a renormalization effect that partially offsets the expansion.[73]

The dispersions for both the unperturbed $[E_c^o(k), E_v^o(k)]$ and perturbed $[E_c(k), E_v(k)]$ bands are shown in (a) and (b), respectively. Accordingly, the Burstein-Moss shift is,

$$\Delta E_g^{BM} = [E_c^o(k_F) - E_v^o(k_F)] - E_g^o \qquad \text{Equation 2.38}$$

$$\Delta E_g^{BM} = \frac{\hbar^2 k_F^2}{2m_c^*} + \frac{\hbar^2 k_F^2}{2m_v^*} = \frac{\hbar^2 k_F^2}{2m_{vc}^*} \qquad \text{Equation 2.39}$$

where, m_c^* and m_v^* represent the effective mass of electrons in the conduction band and holes in the valence band, respectively. The reduced effective mass m_{vc}^* is as,

$$m_{vc}^{*} = \left[\frac{1}{m_c^{*}} + \frac{1}{m_v^{*}} \right]^{-1} \qquad \text{Equation 2.40}$$

Using the values determined by Gupta ($m_c^{*} = 0.35m_e$ and $m_v^{*} = 0.6m_e$), m_{vc}^{*} is calculated as $0.22m_e$.[49] Substitution of the Fermi wave number into equation 2.39 leads to the free electron concentration dependent expression for the Burstein-Moss effect in degenerate semiconductors characterized by parabolic dispersions as,[49, 69]

$$\Delta E_g^{BM} = \frac{\hbar^2}{2m_{vc}^{*}} (3\pi^2 n)^{2/3} \qquad \text{Equation 2.41}$$

2.5.7 Optical Effects of the Semiconductor-to-Metal Transition

The apparent band gap in ITO will be a combination of the intrinsic gap E_g^o and the Burstein-Moss widening ΔE_g^{BM} for a free electron concentration up to that established by the Mott criteria N_c, described earlier through Equation 2.3. This critical concentration correlates with a merging of the degenerate donor level and the conduction band. It is common practice to assume that this merging does not alter the **k**-dependence of the conduction band (i.e., rigid shift of the band with no change in the electron effective mass).[69] As will be discussed in chapter five, this assumption of a constant effective electron mass is not strictly valid for highly doped TCOs[43, 74-83] and may therefore, lead to a departure of experimentally determined band gap values from those predicted by classical quantum confinement theory. The effects of free electrons on an n-type conduction band structure are shown graphically in Figure 2.8 for the case of both a

theoretically ordered donor impurity distribution and the more realistic picture of a random distribution. At low doping density, states of adjacent impurities do not interact and their ground states are located at discrete and energetically well-defined levels. As the concentration increases to medium doping, states of adjacent impurities interact, split, and ultimately form an impurity band.[2] Due to their close proximity to the conduction band, these electrons are easily ionized and available for conductivity at room temperature.[38] Upon further increase to high doping, the growing impurity band eventually merges with the conduction band and the Fermi energy is then located above the conduction band minimum.

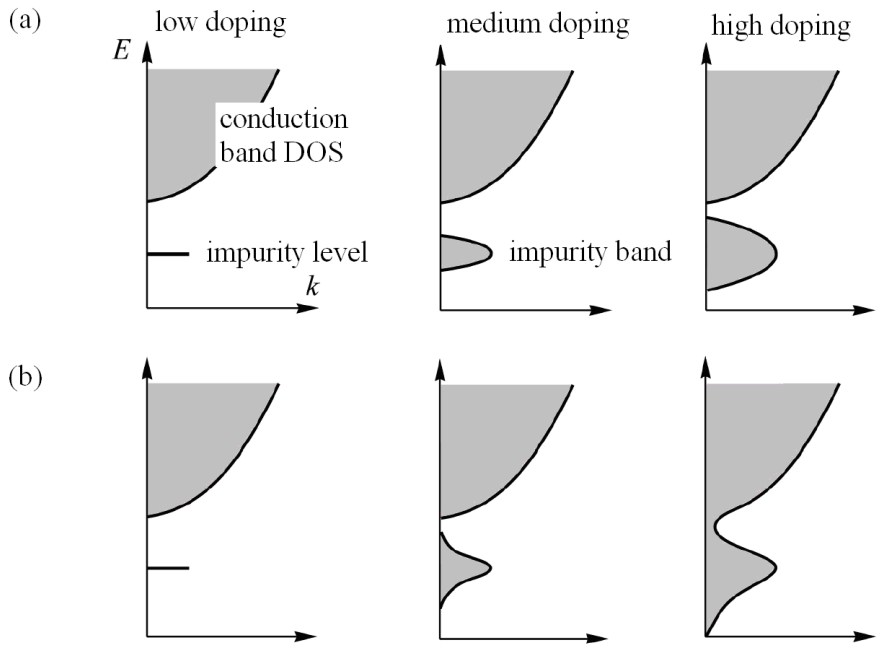

Figure 2.8: Donor impurity level and donor impurity band at low, medium and high doping concentrations for (a) an ordered impurity distribution and (b) a random impurity distribution.[2]

2.5.8 Many-Body Interactions and Band Gap Narrowing

Above N_c, the optical gap expands at a different rate due to the correlated motion of these charge carriers.[77] Coulomb interactions, mutual exchange forces, and attractive impurity scattering of charged electrons and holes create a downward shift of the conduction band and an upward shift of the valence band. These events lead to the adjustment shown in Figure 2.7c. The dependence of this band gap narrowing on free electron concentration has been considered for many materials. Most calculations of the effect are based on a weakly interacting electron-gas model, in which the gap shrinkage is proportional to $n^{1/3}$.[84] This is simply the dependence of n seen in the Fermi wave number of equation 2.35 and accordingly, the band gap narrowing due to exchange interactions only is given by,

$$\Delta E_g^{BGN} = \frac{e^2}{2\varepsilon_\infty \pi^2}(3\pi^2 n)^{1/3} \qquad \text{Equation 2.42}$$

As this expression specifically neglects the effects of screening, the $n^{1/3}$ law should be regarded as empirical. Calculations using the random-phase approximation may be required for more highly accurate models of the band gap renormalization effect.[73]

2.6 Potential Influence of Quantum Confinement

The total measured band gap expansion, which is the apparent band gap minus that of an undoped material, is given by $\Delta E_g^m = \Delta E_g^{BM} - \Delta E_g^{BGN}$. Analysis of the colloidal ITO nanoparticle system disclosed in this dissertation will utilize this expression for the

determination of free electron concentration, n. Implicit in this analysis, is the ability to identify the degree to which a measured bandgap expansion has been caused by something other than free electrons in the lattice. Therefore, quantum confinement is a factor that must be considered in the present case due to the small size of particles developed. Spatial confinement of free electron motion in any dimension will eliminate momentum terms and alter the kinetic energy dispersion to directly affect the density of states as shown in Table 2.3 and graphically in Figure 2.9.[2] As the position of a free electron becomes better defined within a small sphere, the Heisenberg uncertainty principal dictates that its momentum must become increasingly uncertain.[85] We may now consider the idea that there are essentially, no "free" electrons in the colloidal ITO nanoparticles produced in this dissertation work and thus, no band dispersion in the classical free-electron-dependent momentum sense. "Excess conduction electrons" are present but, their motion and kinetic energy are confined. The Fermi wavenumber k_F, will then become only a function of particle size and quantum number. An understanding of this may be achieved through the particle-in-a-box exercise.

Table 2.3: Density of states for a semiconductor with 3, 2, 1, and 0 degrees of freedom for the propagation of electrons in its lattice.[2]

Degrees of freedom	Dispersion (kinetic energy)	Density of states	Effective density of states
3 (bulk)	$E = \frac{\hbar^2}{2m^*}(k_x^2 + k_y^2 + k_z^2)$	$\rho_{\mathrm{DOS}}^{\mathrm{3D}} = \frac{1}{2\pi^2}\left(\frac{2m^*}{\hbar^2}\right)^{\frac{3}{2}}\sqrt{E - E_{\mathrm{C}}}$	
	$N_{\mathrm{c}}^{\mathrm{3D}} = \frac{1}{\sqrt{2}}\left(\frac{m^* kT}{\pi\hbar^2}\right)^{\frac{3}{2}}$		
2 (slab)	$E = \frac{\hbar^2}{2m^*}(k_x^2 + k_y^2)$	$\rho_{\mathrm{DOS}}^{\mathrm{2D}} = \frac{m^*}{\pi\hbar^2}\sigma(E - E_{\mathrm{C}})$	$N_{\mathrm{c}}^{\mathrm{2D}} = \frac{m^*}{\pi\hbar^2}kT$
1 (wire)	$E = \frac{\hbar^2}{2m^*}(k_x^2)$	$\rho_{\mathrm{DOS}}^{\mathrm{1D}} = \frac{m^*}{\pi\hbar}\sqrt{\frac{m^*}{2(E - E_{\mathrm{C}})}}$	$N_{\mathrm{c}}^{\mathrm{1D}} = \sqrt{\frac{m^* kT}{2\pi\hbar^2}}$
0 (box)	–	$\rho_{\mathrm{DOS}}^{\mathrm{0D}} = 2\delta(E - E_{\mathrm{C}})$	$N_{\mathrm{c}}^{\mathrm{0D}} = 2$

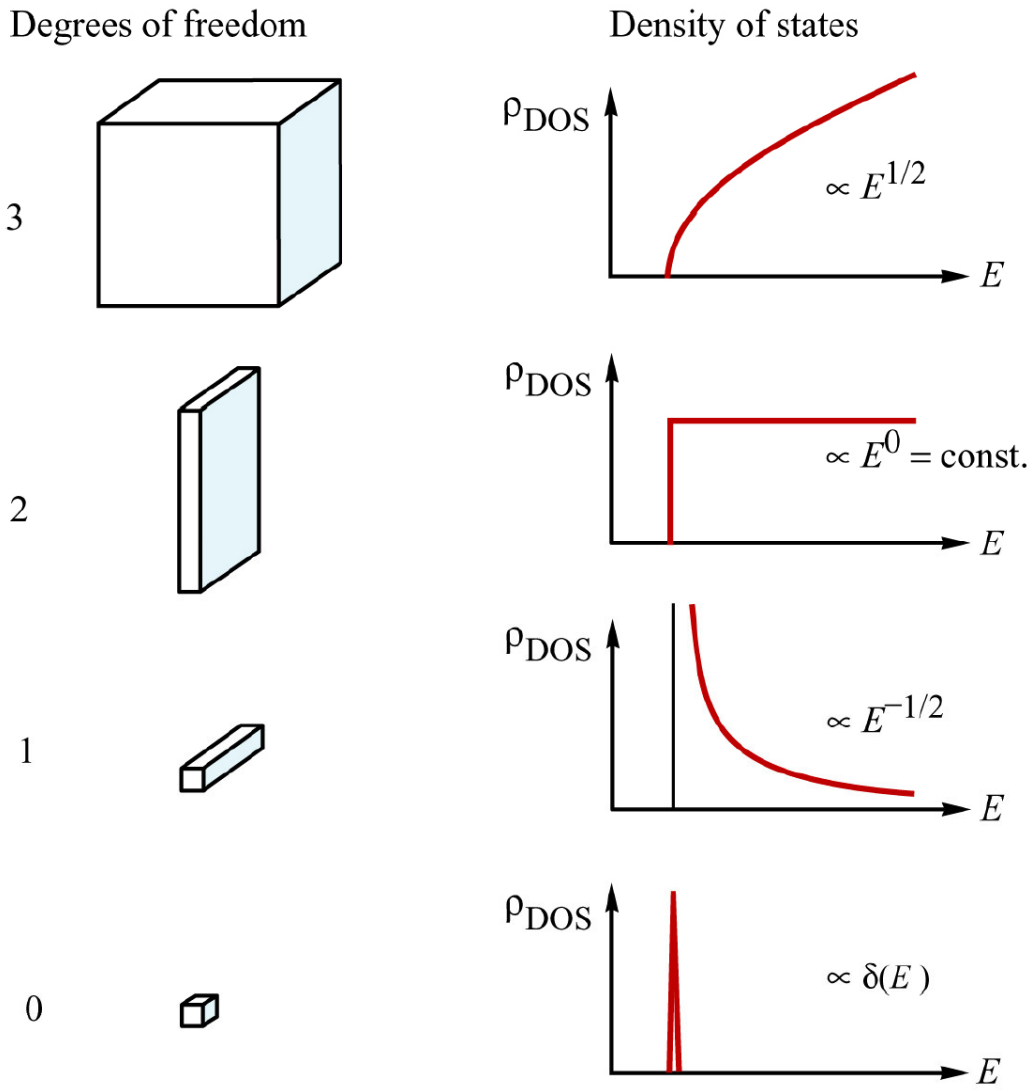

Figure 2.9: Graphical depiction for the density of states in a semiconductor with 3, 2, 1, and 0 degrees of freedom for the propagation of electrons in its lattice. The colloidal ITO produced in the present work should be represented by the 0-D case with density of states displaying the delta-function.[2]

2.6.1 Fundamental Quantum Confinement Theory

Consider the case of a single electron trapped within a box of length *L*, made with walls of infinite potential as shown in Figure 2.10 (top). In order to obtain specific values for the energy of this electron, a quantum mechanical Hamiltonian operator is applied to its wavefunction. This Hamiltonian contains the operations associated with both potential and kinetic energies as,

$$H_{operator} = \frac{-\hbar^2}{2m}\frac{\partial^2}{\partial x^2} + U(x) \qquad \text{Equation 2.49}$$

where, *U(x)* is the potential energy. The result of this treatment is the Schrodinger equation which can be separated into a time evolution component and a time-independent expression commonly presented as,

$$\frac{-\hbar^2}{2m}\frac{d^2\psi(x)}{dx^2} + U(x)\psi(x) = E\psi(x) \qquad \text{Equation 2.50}$$

where, *E* represents the electron energy. Solutions to this equation will only exist at certain eigenvalues $\Psi(x)$ as shown for the harmonic oscillator used to approximate the conduction band of a direct band gap semiconductor in Figure 2.10 (bottom).[86]

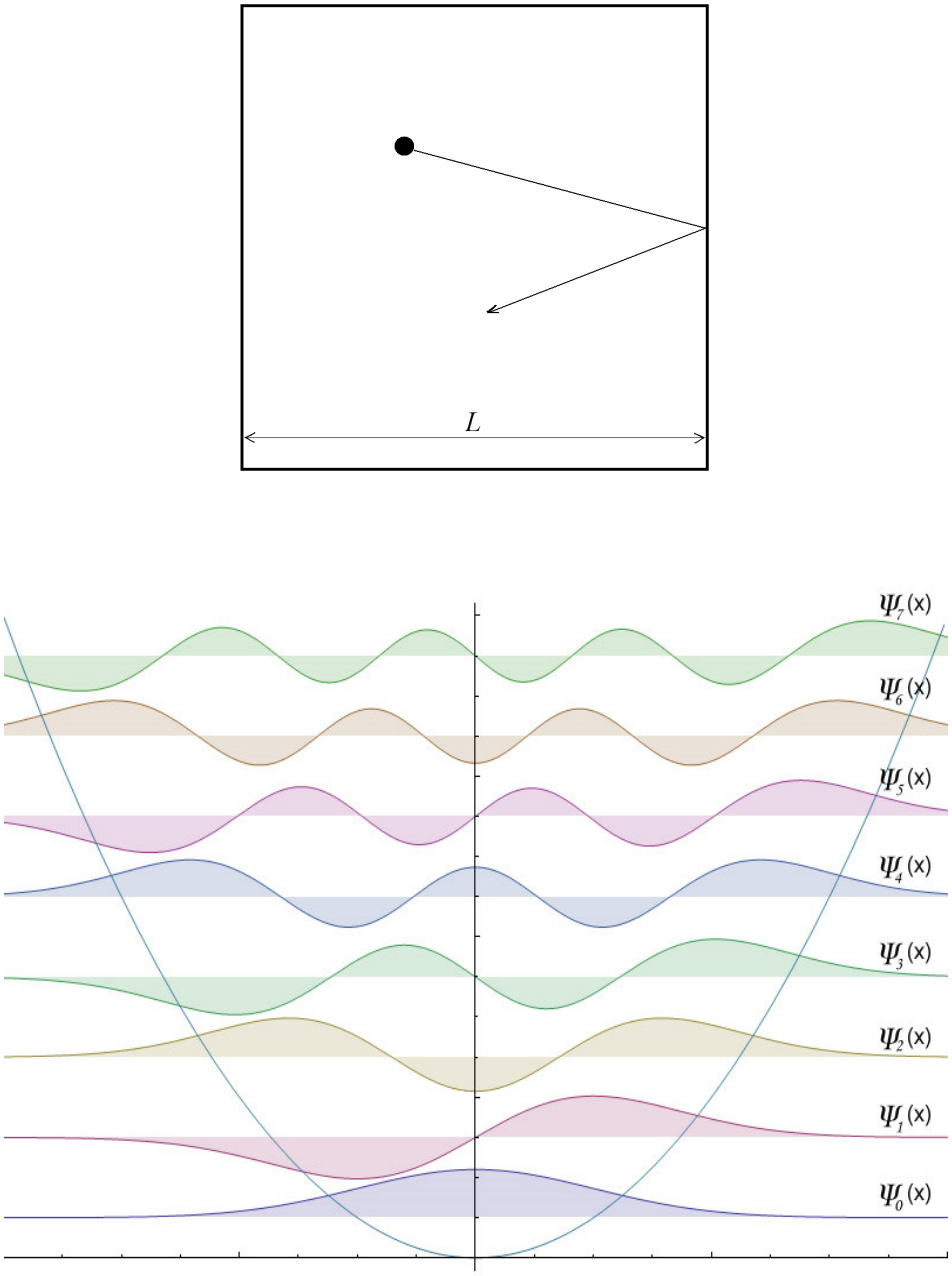

Figure 2.10: (top) Single free electron trapped inside an empty box of length L composed of walls with infinite potential such that no wave-modes exist outside. The bottom figure displays wavefunction representations for the first eight bound eigenstates, n = 0 to 7 of this electron.[86] Note that only sine waves are possible solutions within the confined volume.

The potential of the trapped electron both at x < 0 and x > L is infinity and therefore, the time-independent Schrodinger equation is reduced to,

$$\frac{-\hbar^2}{2m}\frac{d^2\psi(x)}{dx^2} = E\psi(x) \qquad \text{Equation 2.51}$$

$$\frac{d^2\psi(x)}{dx^2} + k^2\psi(x) = 0 \qquad \text{Equation 2.52}$$

where, $k^2 = \frac{2mE}{\hbar^2}$

A general solution to this treatment is of the form, $\psi(x) = A\sin(kx) + B\cos(kx)$. At $\psi(0) = 0$, B=0 and at $\psi(L) = 0$, $kL = n\pi$. Accordingly, the bound solution inside this potential box yields only sine waves with the largest wavelength being equal to $\lambda = 2L$ and the wavenumber k is now as, $k = \frac{n\pi}{L}$. Higher modes will have wavelengths given by, $\lambda = \frac{2L}{n}$ where n = 1,2,3,4, etc… Substitution of this expression into the DeBroglie equation relating wavelength to momentum p yields, $p = \frac{h}{\lambda} = \frac{nh}{2L}$. These expressions may now be used to determine the energy associated with a single electron trapped inside the box shown in Figure 2.10 as,

$$E_n = \frac{1}{2}mv^2 = \frac{p^2}{2m} = \frac{h^2}{2m\lambda^2} = \frac{h^2}{2m}\left[\frac{k}{2\pi}\right]^2 = \frac{h^2}{2m}\left[\frac{n}{2L}\right]^2 = \left[\frac{h^2}{8mL^2}\right]n^2 = \frac{n^2\hbar^2\pi^2}{2mL^2}$$

Equation 2.53

As the box dimension L is decreased, the energy of an electron trapped within is increased. As shown in Figure 2.11, the separation between quantum states is also increased and is an effect that will prove particularly important for the case of colloidal ITO nanoparticles produced in this work.

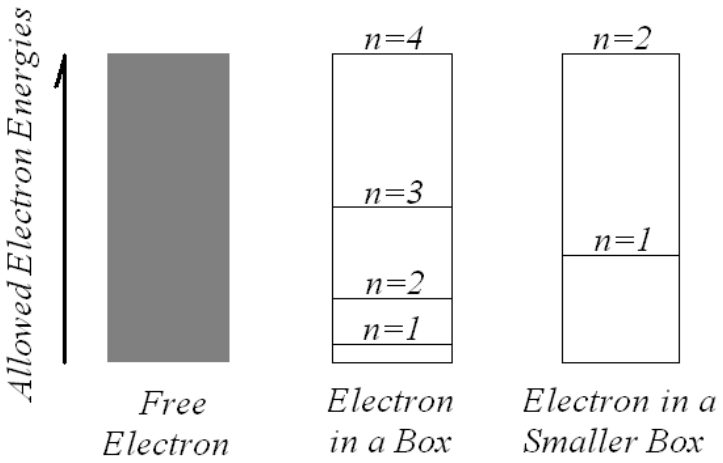

Figure 2.11: Allowed energy levels for free electrons in a bulk material and a single electron trapped within an increasingly smaller box as that displayed in Figure 2.10.

2.6.2 Confinement in Colloidal Semiconductors – EMA Theory

In the case of colloidal semiconductor nanoparticles, Equation 2.53 must be modified to account for shape and electron-hole, Coulomb interactions. Brus formulated an expression to estimate a size-dependent separation between the highest occupied molecular orbital (HOMO) and lowest unoccupied molecular orbital (LUMO) levels in a non-degenerate semiconductor.[16-18] This transition is that of a valence electron to the *1s-like* energy states of the conduction band where the quantum number n, is equal to one. The form most often cited is commonly termed the Effective Mass Approximation,

$$E(R) = E_g + \frac{h^2\pi^2}{2R^2 m_{cv}^*} - \frac{1.8e^2}{\varepsilon_\infty R} \qquad \text{Equation 2.54}$$

where, E_g is the band gap of a corresponding bulk material, R is the radius of a roughly spherical particle and m_{cv}^* is the reduced effective mass of the electron-hole pair (exciton). Note the inclusion of a Coulomb attraction term with dependence on R^{-1}. In this case, the band gap of a semiconductor nanoparticle will change principally with a variation in particle radius of R^{-2}. A typical Mott-Wannier exciton has a radius much larger than the lattice spacing through which it travels and can be calculated by the following expression;

$$a_B = \frac{h^2\varepsilon_\infty}{\pi e^2}\left(\frac{1}{m_c^*} + \frac{1}{m_v^*}\right) \qquad \text{Equation 2.55}$$

where h is Planck's constant, ε_∞ is the bulk optical dielectric constant, e is the electron charge, and m_c^* and m_v^* the effective masses of the electron and hole, respectively. Using the previously discussed values ($\varepsilon_\infty = 8.9$, $m_c^* = 0.35m_0$, and $m_v^* = 0.6m_0$)[49], the Bohr radius of a Mott-Wannier exciton within In_2O_3 is calculated to be ~2.13nm. The effects of spatial confinement will be initially observed at particle sizes less than approximately twice this value (~8.5nm diameter); the onset of a weak-confinement regime.[87] Reduced particle dimensions force the electron and hole wavefunctions to progressively overlap; making exciton formation increasingly difficult and this is at the heart of quantum confinement theory.

This treatment will suffice for estimation of transitions from the valence band maximum to the conduction band minimum or 1s level. However, transitions to higher conduction band states (1p, 1d, 2s, 1f, etc…) require that the roughly spherical nature of a colloidal nanoparticle be considered. In this case, the eigenfunctions $\psi(x)$ of the time-independent Schrodinger equation are no longer sinusoidal but, are the product of spherical harmonics ϑ_l^m and a radial spherical Bessel function $R(r)$,[88]

$$\psi(r) = \vartheta_l^m(\theta, \varphi)R(r) \qquad \text{Equation 2.56}$$

For a spherical potential well of diameter D with an infinite potential barrier, the wave functions must vanish at the well's edge and the energy levels are therefore, found by identifying the roots χ_{nl} of the Bessel function shown in Table 2.4 and the expression,

$$E_{nl} = \frac{2\hbar^2 \chi_{nl}^2}{mD^2} \qquad \text{Equation 2.57}$$

Table 2.4: Roots of the Bessel function χ_{nl}[89]

l	$n = 1$	$n = 2$	$n = 3$
0	π	2π	3π
1	4.493	7.725	9.425
2	5.764	9.095	10.904
3	6.988	10.417	
4	8.183		
5	9.356		
6	10.513		

Using equation 2.57, the variation of energy levels for an undoped In_2O_3 colloid with particle diameter were calculated and are displayed in Figure 2.12. It is this potential size-effect that must be considered when estimating excess conduction electron concentration from a measured band gap expansion for a specific colloidal ITO sample. It is important to note that this quantum confinement model begins to break down at particle diameters less than approximately 2nm. At this point, transitions to the conduction band states are increasingly located in regions where a parabolic dispersion estimate is no longer valid. This is the case for a 1s-like state and may certainly be expected for those higher positioned (1p, 1d, 2s, 1f, etc…) as well.

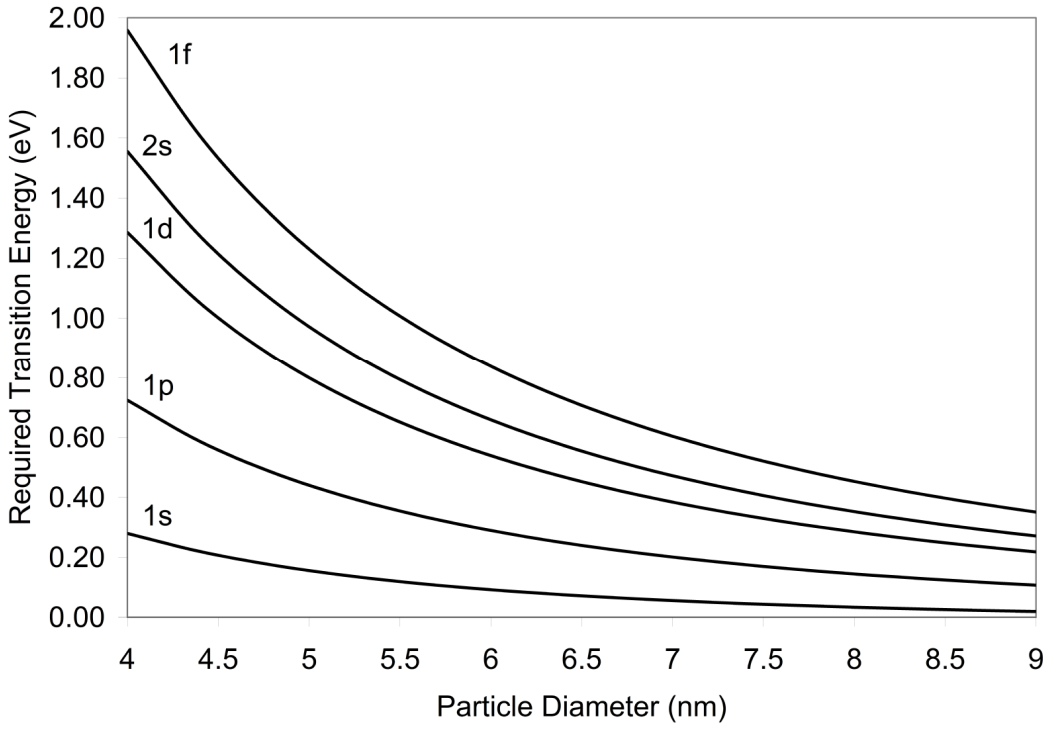

Figure 2.12: Theoretical variation of the available electron energy levels with particle size for a colloidal In_2O_3 nanoparticle system.

A central issue faced in this dissertation work is the question of how degenerate n-type doping may alter these confinement characteristics. A variety of groups have reported electron injection studies within initially undoped (non-degenerate) colloidal semiconductor nanoparticle (quantum dot) systems.[90-94] Accordingly, their results involved the so-called "single electron" energy levels with each electron produced having an associated hole present in the valence band. It is unclear how the significant numbers of extrinsically produced electrons already present in an ITO system will alter the confined exciton binding energy. To the best of our knowledge, extensive studies of the quantum confinement effect in a colloidal transparent conducting system have not yet been reported. In the absence of an accepted theory of confinement in highly degenerate systems, free electron concentration will be calculated from the optical spectra within the bounds of two limiting extremes (no quantum confinement and EMA quantum confinement theory).

CHAPTER 3

ANALYSIS METHODS

3.1 Introduction

Experimental analysis of the colloidal ITO nanoparticle system produced in this work was aimed at investigating basic material physics and establishing some fundamental composition-structure-property relationships. The reaction progression, elemental composition, internal lattice structure, and overall morphology were determined with a variety of techniques. Information gained from these efforts, were correlated with electro-optical properties determined from both static and in-situ optical methods.

3.2 Fourier Transform Infrared Spectroscopy (FT-IR)

FT-IR was utilized to monitor the synthesis process by analyzing the absorption signature of reactants and by-products at various time points. Hot aliquots of the reaction solution were injected between CaF_2 windows and analyzed with a Nexus 870 Infrared spectrometer operating with $2cm^{-1}$ resolution. Molecular bonds vibrate in various modes (stretch, twist, wag) when they interact with specific frequencies of electromagnetic radiation. These frequencies correspond to the ground state E_0 and several excited states E_1, E_2, E_3, E_n of a specific bond.[95] For a given transition between two states, the frequency of light absorbed must precisely equal the energy difference between those states as,

$$E_1 - E_0 = \frac{hc}{\lambda} \qquad \text{Equation 3.1}$$

The energy corresponding to transitions between vibrational states is on the order of 1-10 kilocalories/mole and thus, corresponds to the infrared regime.

Unlike grating spectrometers in which spectral data are acquired sequentially at individual wavelengths, FT-IR is based on a Michelson interferometer. As the schematic setup in Figure 3.1 shows, a typical FT-IR spectrometer consists of a light source, interferometer, sample, and detector. The Michelson interferometer configuration produces an interference pattern by splitting a beam of light into two paths, reflecting those beams back, and recombining them. While one beam is reflected off a fixed mirror, the other interacts with a moving mirror that introduces a time delay allowing the temporal coherence of light to be measured at each specific time delay setting. This effectively converts the time domain into a spatial coordinate. By making measurements of the signal at many discrete positions of the moving mirror, the spectrum can be reconstructed using a Fourier transform of the light's temporal coherence.[95]

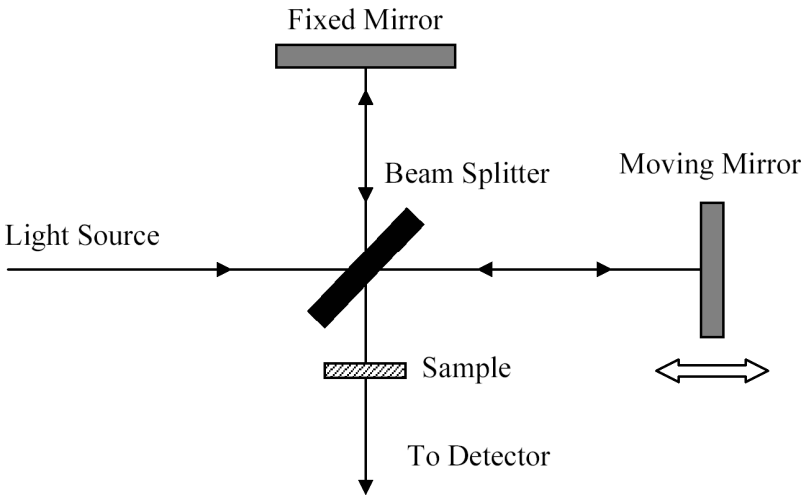

Figure 3.1: Schematic setup for a FT-IR spectrometer in the Michelson interferometer configuration.

3.3 Inductively Coupled Plasma Mass Spectrometry

The percentage of tin doping achieved (Sn:In ratio) in each sample was determined using Inductively Coupled Plasma Mass Spectrometry (ICP-MS). ICP-MS uses an inductively coupled plasma to produce ions which are then detected and analyzed with a mass spectrometer. More sensitive than standard graphite furnace atomic absorption methods, ICP-MS is capable of identifying a range of metals at concentrations below one part in 10^{12} (one-trillionth).[96] The system produces a high-temperature plasma (~10,000K) that consists primarily of argon atoms with a small fraction of free electrons and argon ions. Samples to be analyzed are introduced into this plasma as a mist formed by their passage through a nebulizer. As a droplet of nebulized sample enters the central channel of the ICP, it evaporates and any solids that were dissolved in the liquid vaporize and break down into constituent atoms. A significant proportion of these atoms are ionized within the high temperature plasma environment. The singly charged ions are then extracted through a series of cones into a quadrupole mass spectrometer where they are separated on the basis of their mass-to-charge ratio.[96] A schematic of the ICP-MS system utilized in this dissertation work is presented in Figure 3.2. Dopant concentrations were determined through calibration with elemental standards of indium and tin. Samples were weighed in teflon digestion vessels, allowed to dry, then dissolved in 5 mL of trace metal grade HCl. Following microwave digestion in sealed teflon containers for 20 min at 400 watts and 20 min at 200 watts, the solutions were diluted with de-ionized water up to 10 mL in total volume.

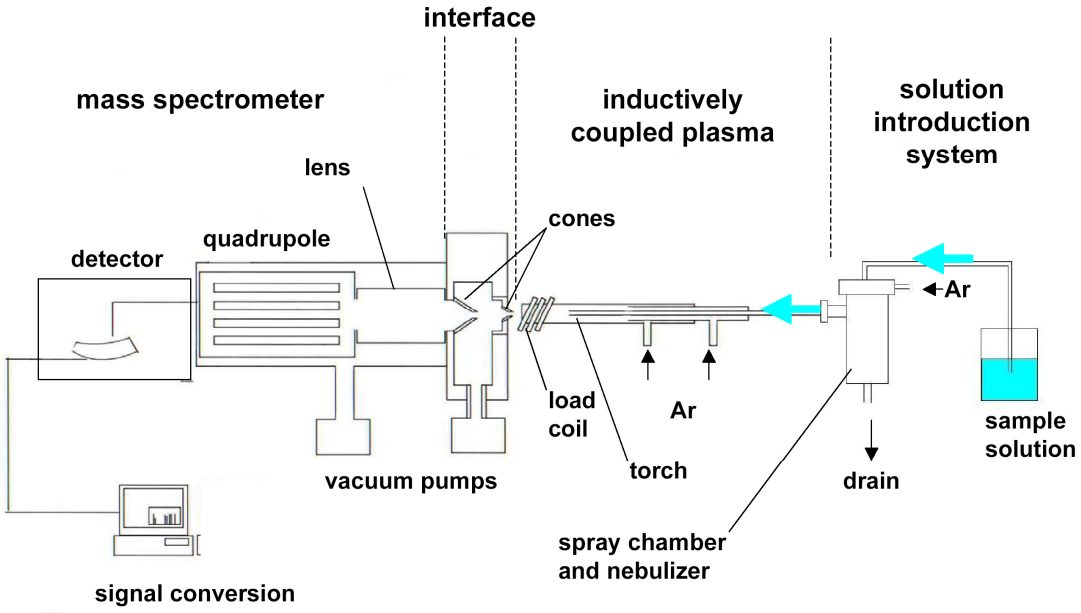

Figure 3.2: Schematic of an Inductively Coupled Plasma Mass Spectrometer ICP-MS.

3.4 Thermogravic Analysis (TGA)

TGA was used to determine the minimum temperature required to remove organic ligands from the surface of colloidal ITO particles as well as the ratio of ligand to nanoparticle. Measurements were performed with a Thermal Analysis (TA) Model XY TGA at a heating rate of 10˚C/min to 500 ˚C in both air and oxygen environments.

3.5 X-ray Diffraction Analysis

Particle phase, lattice structure, and size were determined through the use of an X'Pert Pro Alpha-1 diffractometer equipped with a Cu Kα X-ray tube emitting at 1.54 angstroms. Colloidal solutions of ITO nanoparticles were dropped onto a Si(510) zero-background sample plate for the analysis. A 2θ step-size of 0.002 with a continuous scanning angular rate was employed to record diffraction peaks from 20 to 80 degrees. The x-ray spectra produced displays the intensities of the diffraction peaks as a function

of the detecting angle 2θ. The d-spacing of these peaks may be calculated from Bragg's diffraction law, $\lambda = 2d \sin\theta$, in the first order.[97] The assignment of Miller indices to each reflection peak was accomplished by consultation of published data obtained from the International Center for Diffraction Data. Application of the Scherrer equation to diffraction data for the purpose of particle size estimation is described in chapter four.

3.6 Electron Microscopy

Particle imaging was accomplished with a JEOL 100CX II transmission electron microscope (TEM) operating at 100 kV. Additional structural information on selected samples was also determined with a selected area electron diffraction (SAED) attachment. High resolution (HR-TEM) imaging was achieved with a Scanning Transmission Electron Microscope STEM (model HB603UX) operating at 300 kV and equipped with a Nion aberration corrector. Specimens were prepared by placing a single drop of heavily diluted ITO in a chloroform solution onto a carbon-coated copper grid. A LEO Low-Voltage scanning electron microscope (SEM) was used to image the surface morphology of pressed pellets of ITO nanoparticles following high-temperature annealing.

3.7 Four-Point Probe

Electrical characterization of pellet specimens was conducted using the DC four-point probe resistivity method. The four-point probe consists of two current carrying probes (1 and 4), and two voltage measuring probes (2 and 3). Very little contact and spreading resistance are associated with the voltage probes. Accordingly, one can obtain a fairly accurate measurement of the sheet resistance.[98] The specific system utilized consisted of

a Signatone model SP4-40045TFS probe head mounted on a Signatone model S301-6 station. Leads from the probes were connected to a Keithley 2182A nanovoltmeter and Keithley 6221 AC/DC current source meter.

3.8 Optical Spectroscopy

Optical properties of the colloidal ITO solution were analyzed using a Cary 5000 spectrophotometer operated from the UV to NIR (200 - 2000nm) spectral regions at a step size of 5Å. This specific equipment is capable of dual beam operation in which incident light is split into two paths such that transmission data from the ITO sample and a pure sample of dispersing solvent can be gathered simultaneously. ITO samples were dispersed in solution with variable dilution and placed in a 1cm square quartz cuvette for analysis at room temperature.

In-situ optical analysis during ITO synthesis was achieved using a high-temperature dip probe assembly (Figure 3.3) coupled with an Ocean Optics USB2000 spectrometer. The USB2000 utilizes a linear charge coupled device (CCD) array for photon counting and is capable of full spectra from 300nm to 800nm at 3ms intervals.

Figure 3.3: High-Temperature dip probe assembly used for In-Situ transmission analysis during colloidal ITO nanoparticle synthesis. A mirror is found inside the lower tip of the probe heads shown to the right. This reflects incident white light back through the colloidal solution and into a receiving optical fiber for transference to the USB2000 spectrometer.

CHAPTER 4

PROCESS DEVELOPMENT AND SYSTEM PROPERTIES

4.1 Introduction

The production of colloidal particles at sizes small enough to produce three dimensional electron confinement has flourished over the last two decades. While our synthesis approach relied on much of this previous work, some aspects of the specific route taken are novel for doped metal oxides and in particular, for the ITO system. This chapter begins with a discussion of nucleation and growth theory in light of the influence that impurity doping has on the formation of primary nuclei. The methods of producing these structures with an emphasis on "greener" synthetic approaches are then highlighted. The specific reaction pathway developed for ITO synthesis is described and analyzed by FT-IR. Verification of ITO production is then accomplished through the identification of key physical and functional properties.

4.2 Fundamental Theory of Nucleation and Growth

The most cited models of colloidal nanoparticle formation in solution follow the now classic studies of La Mer and Dinegar which dictate that the production of a monodisperse colloidal system requires temporally discrete events of rapid embryo nucleation followed by slower growth of those initial nuclei.[27, 99-101] When the concentration of reactive precursors in a solvent solution reaches a critical level of supersaturation (C_{SS}), spontaneous phase segregation occurs.[4] The dissolved precursor concentration is then gradually depleted to a level below that required for further

homogeneous nucleation. Provided the reactive precursor level remains above a critical saturation concentration (C_S), these initial embryos will continue to grow by absorption of diffusing atomic matter.[4] This process is displayed in Figure 4.1a. The driving force for phase transition is characterized by the difference in free energy change between solvated and crystalline forms of the material, ΔF_V.[4] For initial nuclei characterized by extremely large surface to volume ratios, this volumetric lattice energy is offset by a surface free energy, γ, which destabilizes the particle toward solvation in proportion to its total surface area.[4] The Gibbs free energy change for the reaction is thus, described by the following equation and graphically in figure 4.1b,

$$\Delta G = 4\pi R^2 \gamma - \frac{4}{3}\pi R^3 \Delta F_V \qquad \text{Equation 4.1}$$

Under conditions of diffusion limited growth, the first derivative of this equation with respect to the nuclei radius R, can be related to the growth rate ($-dR/dt$). The activation barrier shown in Figure 4.1b, defines the critical radius ($R=R^*$) for nuclei stability. Below this value ($dR/dt<0$), nucleated particles will re-dissolve and above it ($dR/dt>0$), grow into larger crystals.[4, 101] The critical radius is determined by taking the derivative of Equation 4.1, setting it to zero, and then solving for R as,

$$R^* = \frac{2\gamma}{\Delta F_V} \qquad \text{Equation 4.2}$$

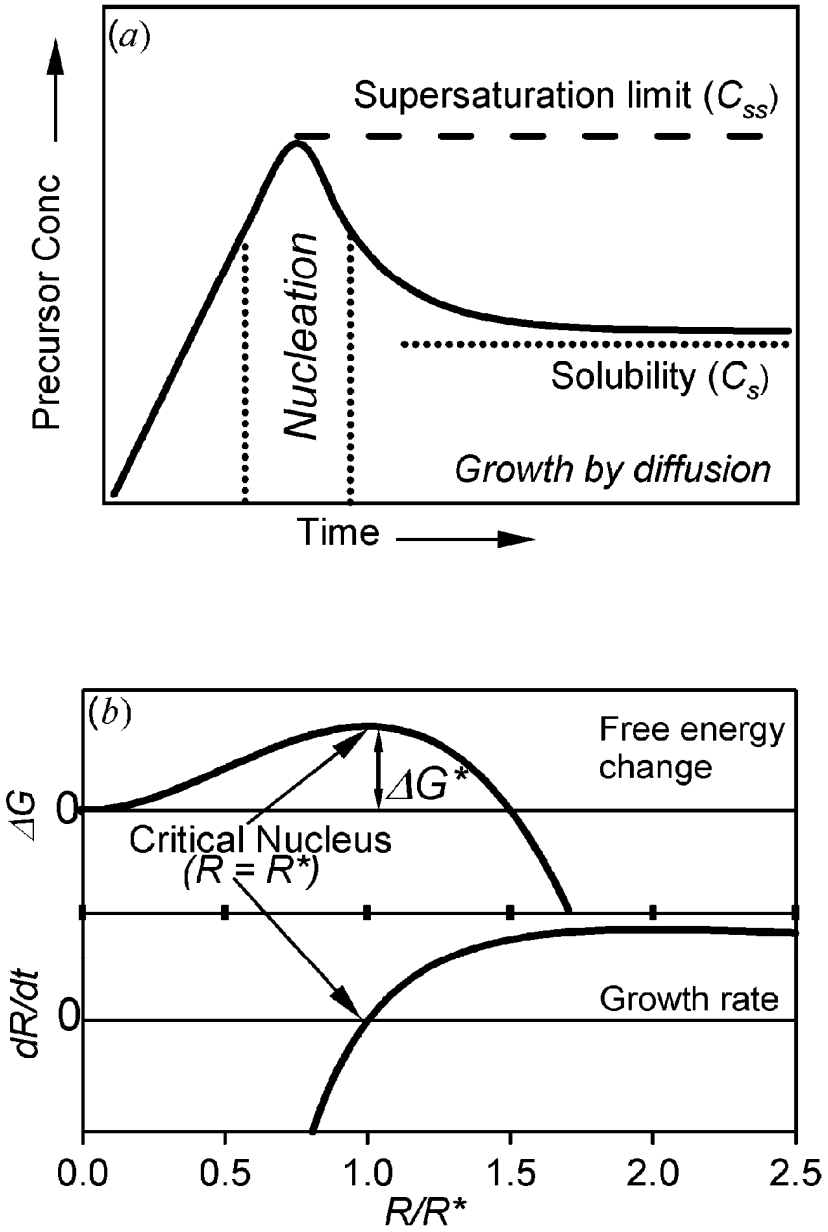

Figure 4.1: (a) LaMer model describing nucleation and growth of crystallites versus time for a constant influx of reactive precursor. A short nucleation time $\delta(t)$, ensures a narrow particle size distribution. (b) Classical nucleation model showing the Gibbs free energy change (ΔG) and growth rate (dR/dT) versus crystallite size, R. The critical size R^* marks a point of nuclei stability.[4]

4.3 Influence of Impurity Doping

There is growing evidence that in many cases, the nucleation process described above proceeds by a two-step mechanism. Amorphous aggregates are formed in the first step, and the second step involves structural reorganization of these clusters into the crystalline form.[4] The ability of these few-atom aggregates to organize into the crystalline form will be influenced by the presence of impurity dopant atoms that induce lattice strain. This strain is manifest in Equation 4.1 as a reduction in some of the driving force for lattice formation, and hence a reduction in the magnitude of ΔF_V.[36] As shown in Figure 4.2, reducing ΔF_V increases the activation barrier for nucleation and accordingly, the required dimension of the critical radius. Consequently, it should be considerably more difficult for the doped nuclei lattice to stabilize than it was for the pure host crystal lattice in the absence of impurities. Within a heated solvent solution containing a mixture of host and impurity precursors, nucleation of doped particles may not be as kinetically favorable as the nucleation of pure host particles. Accordingly, the critical nucleus which becomes a crystalline particle, is likely to be composed of the pure host material.[4]

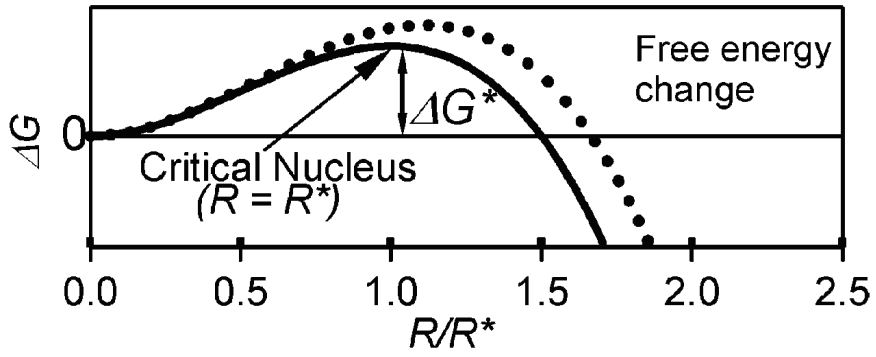

Figure 4.2: Particle nucleation model showing how the Gibbs free energy change (ΔG) is altered by the presence of impurity atoms within a critical nuclei. Dopant incorporation causes lattice strain which destabilizes the nuclei thus increasing the critical radius, R^*.[4]

As the majority of a nanoparticle's mass is not formed during nucleation, the factors affecting incorporation of dopants during diffusional growth from the reaction solution are important. Per the previous discussion, dopant atoms are not generally competitive with solvated host atoms for open surface coordination sites under conditions equally favorable to the diffusional attachment of either species.[4] As the reaction progresses however, the ratio of dopant-to-host precursors improves to the point that dopant attachment becomes competitive enough that lattice incorporation can occur. What results is a concentration gradient and its characteristics are dictated by the kinetic competition between irreversible attachment of host versus dopant ions to the surfaces of growing nanoparticles. Evidence of such a gradient has been previously observed in colloidal nanoparticle forms of both Co-doped ZnO and Sb-doped SnO which were made using reaction solutions of both host and dopant cations.[36, 102] As will be shown in chapter five, in-situ reaction monitoring indicates that a similar structure comprised of a pure indium oxide core surrounded by a tin-doped indium oxide shell may have been formed in the present work.

4.4 Preparation of Colloidal Semiconductor Nanoparticles

The temporal separation of nucleation and growth steps is best achieved by rapid injection of reactive precursors into a solvent solution which is pre-heated above the critical nucleation temperature.[21, 103-105] Soon after a critical level of supersaturation is reached, the resultant nucleation event is quenched by an abrupt reduction in solution temperature below that required for homogeneous nucleation yet high enough for heterogeneous attachment kinetics. The nucleation event time $\delta(t)$, which dictates the

resultant particle size-distribution, is now a function of both precursor concentration and solution temperature. This method has been utilized to produce extremely narrow size distributions in several II-VI and III-V semiconductor nanoparticle systems.[22, 23, 27, 106-109] It is possible to initiate the formation of nanoparticles by simply heating a supersaturated solution of all constituents up to the critical nucleation temperature, however, this often results in an extended nucleation event time and wider size distribution.[101, 110] Both approaches to the synthesis of colloidal ITO nanoparticles were explored in the present work.

Formation of a highly dispersible colloidal nanoparticle system requires the prevention of agglomeration and precipitation due to Van der Waals forces. These attractive forces arise from to the interaction between dipoles in adjacent particles which can be either permanent or induced.[111] Fluctuations in the electron density of particles without a permanent dipole can still give rise to temporary dipoles which may induce additional dipoles in nearby particles. Temporary dipoles and the induced secondary dipoles are then attracted to each other over relatively short spatial ranges. Brownian motion of particles dispersed in a solvent solution ensures close contact and thus, Van der Waals forces will cause agglomeration if some electrostatic or stearic hindrance is not present. This stearic hindrance is routinely accomplished by the attachment of organic ligands to individual nanoparticles as a monolayer through covalent, dative, or ionic bonds, as displayed in Figure 4.3.

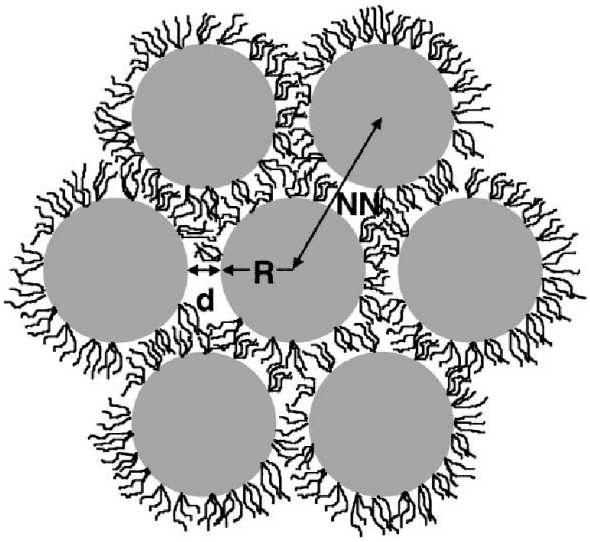

Figure 4.3: Local arrangement of colloidal nanoparticles covered by organic ligands.[103] These structures promote stearic hindrance against attractive Van der Waals forces which would otherwise tend to cause agglomeration and precipitation in solution.

The coupling of ligands to each nanoparticle surface requires that synthesis be performed in a precursor solution containing these organic compounds. Synthesis of this type previously relied on the use of highly toxic organometallic compounds in combination with ligand-based coordinating solvents such as trioctylphosphine oxide (TOPO).[106, 107] Within the last decade, "greener" approaches that utilize simple metal carboxylates with the non-coordinating solvent, octadecene (ODE) have been developed as alternatives to these procedures.[108] The benefits of ODE over other solvents are its lower toxicity due to simple hydrocarbon chains (formula $C_{18}H_{36}$) and a relatively high boiling point of ~315 ˚C. A metal carboxylate is composed of a metal cation and carboxylate anion. As the conjugate base of carboxylic acid, carboxylates contain COO^- groups and are derivatives of characteristic fatty acids (acetic acid, stearic acid, oleic acid, myristic acid, etc…).[112] Metal acetates, metal stearates, metal oleates, and metal

myristates are all common metal carboxylate forms. The key to these procedures is initial production of stable metal carboxylate compounds that can be reacted with anion precursors in a high-temperature solvent solution to initiate the nucleation event. The hydrocarbon chains of these fatty-acid derivatives provide a built-in stearic hindrance against the attractive Van der Waals forces previously discussed. Peng's group was among the first to report successful synthesis of colloidal nanoparticle (quantum dot) versions of both II-VI and III-V semiconductor systems with this general materials class.[23, 27, 113] Within the last 5-10 years, use of metal carboxylates for the successful synthesis of CdS, CdSe, ZnS, ZnSe, InP, and InAs in the colloidal nanoparticle form have been reported.[22, 23, 27, 33, 35, 109, 114, 115]

4.5 Synthesis of Colloidal Indium Oxide Nanoparticles

Metal carboxylates can also be used to form metal oxide nanoparticles by the inclusion of an initiator species that serves to break the C-O bonds in the carbonyl groups.[116-121] The ability to produce highly crystalline, colloidal indium oxide (In_2O_3) nanoparticles by this approach was first observed by our group when attempting to form InN quantum dots. A complex tertiary amine precursor, tris(trimethylsilyl)amine $N[Si(CH_3)_3]_3$, was injected into a heated ODE solvent solution of indium myristate in an attempt to liberate the nitrogen ion for InN formation. Amines are organic compounds and functional groups that contain a basic nitrogen atom with a lone electron pair. They are derivatives of ammonia, wherein one or more hydrogen atoms are replaced by organic substituents such as alkyl or aryl groups.[112] A 1:3 molar ratio of indium acetate to myristic acid was used to form indium myristate. This is just the theoretical amount needed to replace the three

acetic acid groups with myristic acid. A 2:1 ratio of indium acetate to amine was utilized in similar fashion to an indium to phosphorus ratio used in InP quantum dot synthesis by Battaglia and Peng.[27] Rather than producing InN, our process lead to the formation of ~20nm single crystals of colloidal In_2O_3 as displayed in Figure 4.4. The electron diffraction pattern shown in the inset was correlated to the bixbyite crystal structure of pure indium oxide (ICDD Card No. 06-0416) with no evidence of separate tin oxide phases.

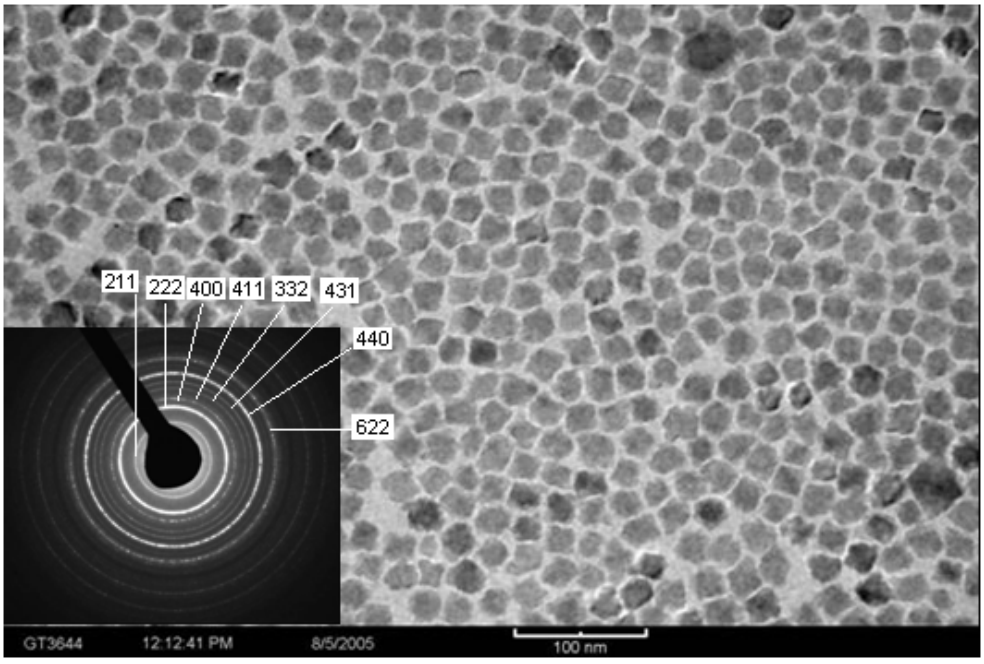

Figure 4.4: TEM image of colloidal In_2O_3 formed by reaction of a complex tertiary amine with indium myristate precursors. The system is highly dispersible within a variety of non-polar solvents. Inset presents an electron diffraction pattern indexed to the bixbyite structure of pure In_2O_3.

A similar approach to produce colloidal In_2O_3 nanoparticles was reported by Narayanaswamy and co-workers one year later in which an alcohol was injected at high temperature to initiate the nucleation and growth event.[122] Each of these precursors (amine and alcohol), had initiated formation of indium oxide through the same general reaction, nucleophilc substitution. As a typical metal carboxylate, indium myristate contains C-O bonds associated with the carbonyl group. Oxygen is the most electronegative of the pair and thus, pulls electron density away from carbon to increase the bond's polarity.[112] As a result, the carbonyl carbon becomes electrophilic and will readily bond with typical nucleophiles such as amines and alcohols. A nucleophile is a reagent that forms a chemical bond to an electrophile by donation of both bonding electrons.[112] In general, the lower electronegativity of nitrogen ions associated with amine compounds makes them more nucleophilic than alcohols. However, tertiary amines such as that used in our initial indium oxide synthesis display a reduced nucleophilic character as compared to primary or secondary amines. This is a result of steric hindrance caused by bulky R groups around the nitrogen and an inability to generate neutral species.[123] As will be shown, a switch to primary amines for the synthesis of colloidal indium oxide and ITO produced for the present work resulted in greatly reduced nanoparticle dimensions. While amines readily form bonds with a variety of materials to act as surfactants, alcohols do not. Due to this non-binding characteristic of alcohols, the synthesis of individual In_2O_3 particles by Narayanaswamy was primarily focused on a variation in the amount of myristic acid as a means to prevent particle agglomeration.[122] In contrast, our synthesis route relied on the concentrations of both myristic acid and amine for individual particle formation.

4.6 Synthesis of Colloidal Indium Tin Oxide Nanoparticles

The synthesis of colloidal Indium Tin Oxide involved some key alterations to the above process. A tin carboxylate precursor was included to achieve the desired In-to-Sn ratio and a more nucleophilic, primary amine *octadecylamine* was utilized. Additionally, six times the amount of this amine relative to that utilized in our previous work on indium oxide was injected. What follows are detailed steps for the synthesis of an ITO system with an In:Sn ratio of 90:10; similar to that found in sputter targets used for thin-film sample preparation. In order to verify that the reaction had progressed as theorized, Fourier Transform Infrared (FT-IR) spectroscopy measurements were taken and this data is presented in Figure 4.5. Hot aliquots of the reaction solution were taken just prior to amine injection and then again, 60 minutes following the event. These solutions were quickly injected between calcium fluoride plates for subsequent analysis.

Materials: Indium acetate (99.99%), tin acetate (99.99%), myristic acid, octadecylamine, and 1-octadecene were obtained from Sigma-Aldrich and used without further purification. Chloroform, acetone, and n-hexane were obtained from VWR Scientific and used as-received.

Synthesis: $In(Ac)_3$ (0.9 mmol), $Sn(Ac)_2$ (0.1 mmol), and myristic acid (MA) (3 mmol) were combined with 30 ml of octadecene (ODE) in a 3-neck, 125ml round bottom flask. It is imperative to prevent significant hydrolysis and associated oxide formation from occurring prior to amine injection at high temperature. Accordingly, this carboxylate solution was attached to a standard Schlenk line assembly, purged with argon several times, and degassed under vacuum at 110 °C for two hours. The Schlenk line is a dual manifold system wherein one manifold is attached to an inert gas source while the other

leads to a vacuum pump. Repetitive purge and fill cycles can reduce the oxygen content of an attached reaction flask to just a few parts per million. While the cation solution degassed, a similar preparation was performed on an amine solution composed of octadecylamine (ODA) (3 mmol) in 1 ml of ODE. The (In+Sn) metal carboxylate solution was then heated to 295 °C under argon flow. This argon atmosphere is important because it prevents an extensive hydrolysis reaction which, as will be shown, is of the reversible type. At this high temperature, one would expect that all acetic acid compounds in 1mmol of $In(Ac)_3$ had been replaced by the 3mmol of myristic acid to form indium myristate, $In(Mt)_3$.[122] However, FT-IR data taken just prior to amine injection at 295 ˚C, displayed a signal corresponding to the COOH stretch of free carboxylic acid at ~1710cm^{-1} which indicates that acetic acid was only partially pyrolized and replaced by myristic acid (Figure 4.5).[122] Therefore, a more proper description of the metal carboxylates present in the reaction flask at this time may be $In(Ac)_{3-x}(Mt)_x$ and $Sn(Ac)_{2-x}(Mt)_x$. The spectra also shows the asymmetric COO^- stretch of indium and tin carboxylate groups from 1510cm^{-1} to 1630cm^{-1} prior to amine injection with the prominent signal at ~1642cm^{-1} being attributed to the ODE solvent.[122] The formation of ITO was visibly apparent as the solution became faint yellow in color within 2-3 seconds of amine injection. This color changed to orange and finally dark green as the reaction progressed over the next five minutes. The FT-IR spectra taken 60 minutes after primary amine injection indicates that the signals corresponding to metal carboxylates and free carboxylic acid have been reduced as the nucleophilic substitution progressed. A weak amide peak near ~1690cm^{-1} may be present but, is difficult to establish with the spectral noise in that region.[124]

The finished product was collected by standard polar/non-polar solvent precipitation techniques utilizing a high-speed centrifuge. The energetic barrier to aggregation provided by the organic capping groups is strongly dependent upon the energy of mixing between tethered ligands and the solvent in which they are dispersed.[103] Addition of a non-solvent which is miscible with the original dispersing solvent, destabilizes the colloidal nanoparticle dispersion allowing aggregation and subsequent precipitation. Following precipitation and washing with acetone and chloroform to remove any side products, the particles were re-dispersed in the non-polar solvent, n-hexane. This colloidal dispersion can be stored at room temperature within a variety of similar non-polar solvents (chloroform, toluene, etc…) for months and potentially years, with no significant particle agglomeration.

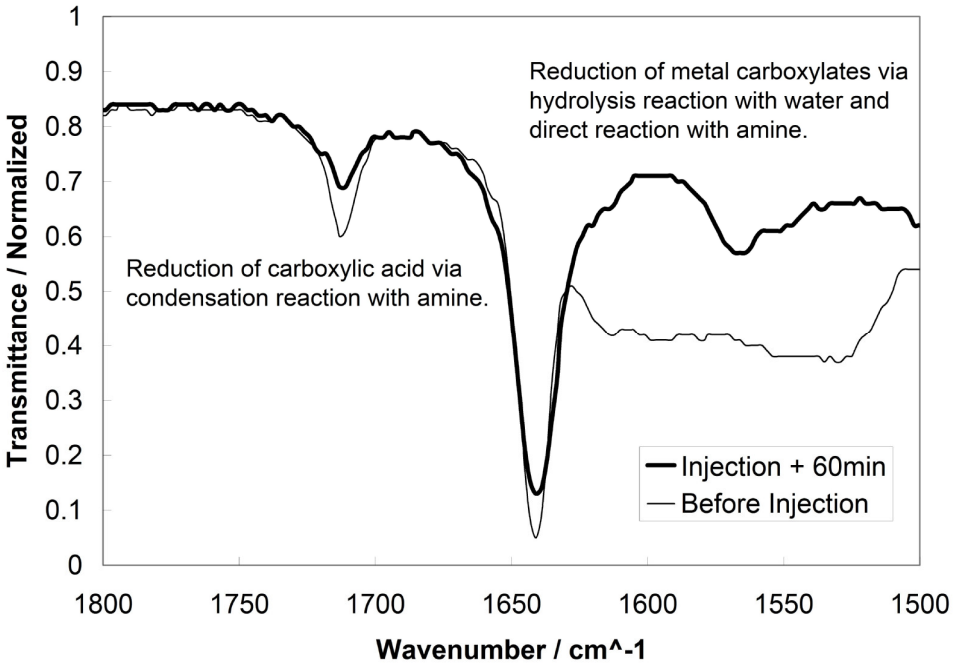

Figure 4.5: FTIR spectra taken before and after primary amine injection. Levels of both free carboxylic (myristic) acid and metal carboxylate precursors are reduced due to the nucleophilic substitution process.[5]

While a general nucleophilic substitution reaction has been described thus far, the presence of free carboxylic acid prior to amine injection indicates that the complete process may be comprised of three interrelated nucleophilic reactions (aminolysis, condensation, and hydrolysis). Figure 4.6 presents the proposed reaction scheme at work in the synthesis of colloidal ITO. The initial reaction of amine with indium myristate results in the cleavage of C-O bonds on the carbonyl group as nitrogen atoms donate both electrons to the electron deficient carbons. This aminolysis reaction produces ITO and an amide as shown.[116] The amine may also react with any free carboxylic acid in solution to produce additional amide and water through a condensation process.[112] The presence of condensed water was observed in cooler regions of the flask where a glass thermowell was attached. The occurrence of this reaction in the present case is important because it may support a secondary condensation-hydrolysis reaction cascade which compliments the primary aminolysis reaction. Due to their formation in a high temperature environment, water molecules will immediately deprotonate and become effective nucleophiles that can react with metal carboxylates as well.[112] A reaction of this type is commonly referred to as hydrolysis and, in the present case, is expected to produce ITO and additional free carboxylic acid, typically written as R-COOH.[122] Free carboxylic acid produced in this hydrolysis process will again react with amine through condensation to produce additional water and thus, a condensation/hydrolysis cascade ensues.

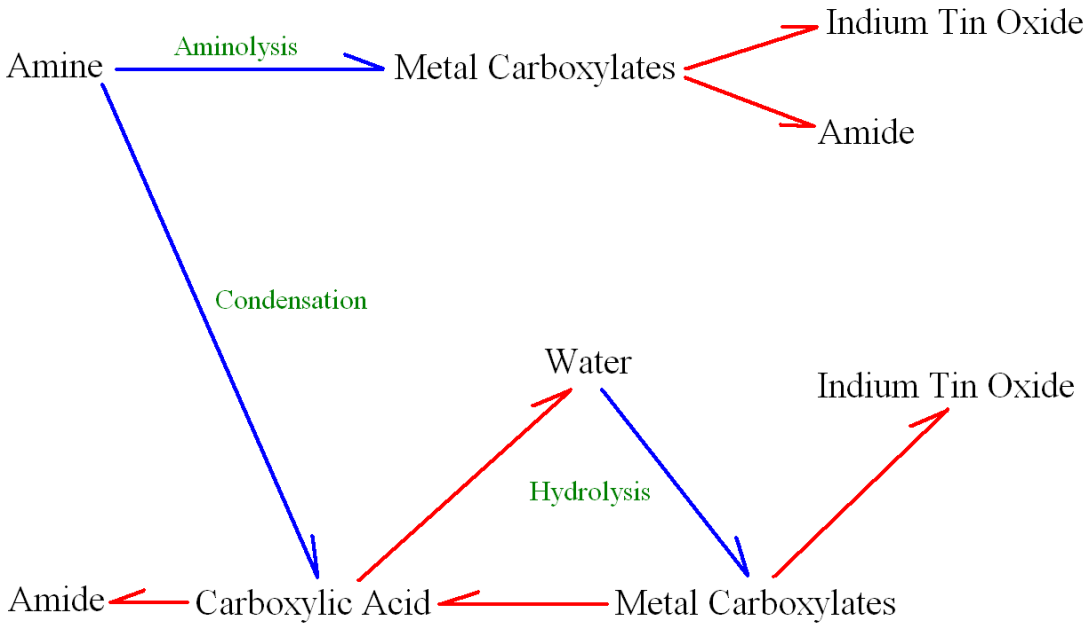

(1) $R'NH_2 + In(RCOO)_3 + Sn(RCOO)_4 \rightarrow ITO + RNHCOR'$ …. **Aminolysis**

(2) $R'NH_2 + RCOOH \rightarrow RNHCOR' + H_2O$ …… **Condensation**

(3) $H_2O + In(RCOO)_3 + Sn(RCOO)_4 \leftrightarrow ITO + RCOOH$ …..... **Hydrolysis**

Figure 4.6: Proposed reaction pathway for the synthesis of colloidal ITO nanoparticles. A combination of rapid nucleophilic substitutions (aminolysis, condensation, and hydrolysis) are displayed in the flow chart with their specific chemical reactions below.

4.7 Verification of Indium Tin Oxide Synthesis

Due to the similarity in atomic masses of indium (114.82) and tin (118.71), one can not rely only on x-ray diffraction and/or electron diffraction analysis to accomplish the task of definitive material identification. As will be shown in section 5.5, the x-ray pattern of undoped indium oxide and a colloidal nanoparticle lattice that incorporates even 20% tin appear essentially identical. All characteristics of the material (composition, structure, and functional properties) must be observed for a definitive identification.

4.7.1 Solution Body Color

An early indication that the material produced in this reaction is ITO can be found by simply observing its body color relative to that of undoped indium oxide. As a wide band gap semiconductor (Eg > 3eV) with absorption edge near ~350nm, In_2O_3 is completely transparent in the visible range (400-700nm).[38, 49] While the absorption edge of ITO is found at even lower wavelengths due to the presence of free electrons, the long wavelength plasma edge associated with these electrons results in some absorption in the visible which produces a green to blue material body color. This difference is clearly observed in the dispersions of colloidal In_2O_3 and ITO displayed in Figure 4.7. The undoped In_2O_3 sample was made using the same synthesis technique but, simply lacking any tin precursor. As will be discussed in detail within chapter five, the green to blue color shift of the ITO displayed in this figure is indicative of the gradual release of free electrons into the material and a filling of available conduction band states. The optical clarity of these solutions is due to a complete lack of particle agglomeration achieved by

the organic compounds utilized in their formation. The samples displayed in Figure 4.7 have shown no signs of agglomeration or turbidity after one year at room temperature.

It was noted that this color shift to blue did not occur when the synthesis process was performed in ambient air rather than the pure argon atmosphere described above and was to be expected. As shown in the reversible reaction of Figure 4.6 above, hydrolysis of metal carboxylates is an efficient route to oxide formation and accordingly, will occur at even mildly elevated temperature. Therefore, a very large amount of oxide nanoparticles will have already been produced via simple hydrolysis prior to any amine injection. The continuous attack of metal oxides by free carboxylic acid produced through hydrolysis will pose problems with proper tin adsorption, lattice incorporation, and associated free electron generation.[122] While more detailed analysis of material formed in an ambient air atmosphere may fully explain the lack of color change observed, no practical reason exists to produce colloidal ITO under these conditions.

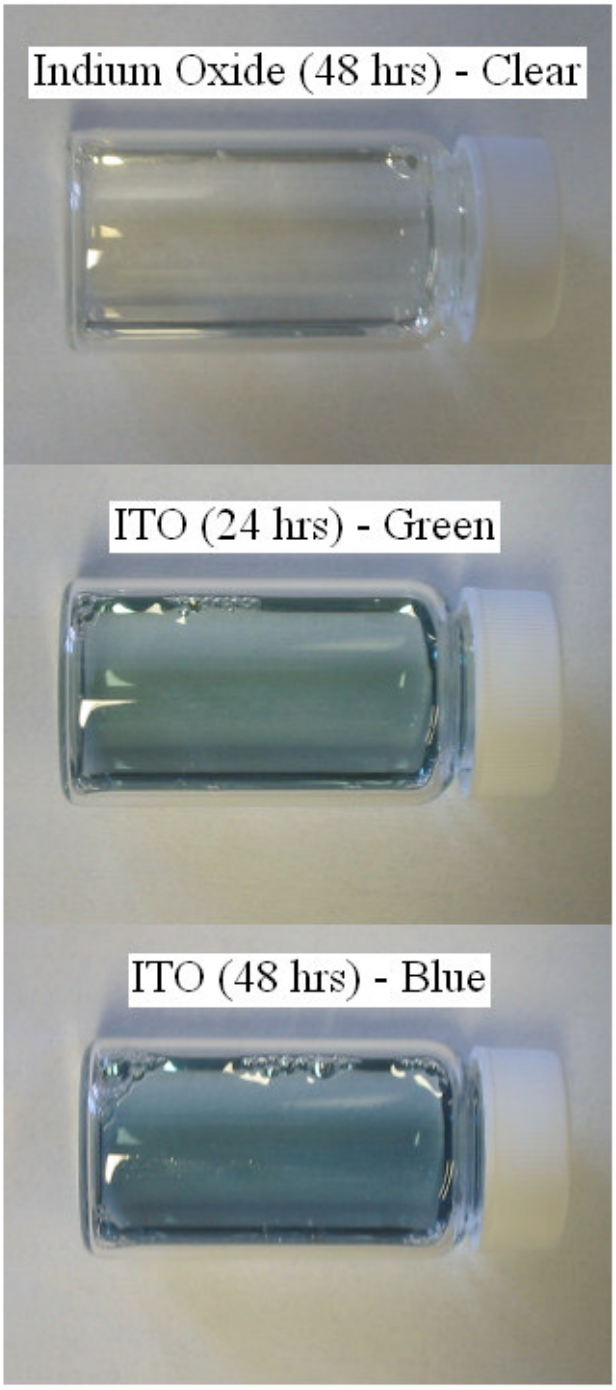

Figure 4.7: Clear undoped In_2O_3 (top), Green ITO 24 hours following synthesis (middle), and Blue ITO 48 hours following synthesis (bottom). All colloidal nanoparticle samples are dispersed in the non-polar solvent, hexane. The observed color change is indicative of progressive free electron generation.

4.7.2 Composition and Structure

The colloidal ITO (48hr) material was analyzed with inductively coupled plasma mass spectroscopy (ICP-MS) in order to determine how much of the 10% tin used for its synthesis had actually been incorporated within the lattice. As discussed in the experimental methods section, ICP-MS is capable of very high resolution measurement of dopant concentrations and was previously utilized for the analysis of manganese-doped ZnSe quantum dots in which Mn concentrations on the order of 0.5% were readily detectable.[30] In the present work, a commercial ITO nano-powder (Sigma Aldrich, ~40nm diameter) was utilized as an internal standard to verify the accuracy of this measurement. Analysis of the colloidal ITO sample displayed in Figure 4.7 indicated that 9.3% Sn was present. This 93% doping efficiency is extremely high as compared to the <10% doping efficiency reported by Erwin and co-workers in their work on ZnSe:Mn quantum dots.[30] Their synthesis method also relied on injection of an anion precursor (selenium) into a hot solvent solution composed of both host and dopant cation precursor compounds (diethylzinc and dimethylmanganese). Verification that the tin was fully incorporated into the indium oxide lattice was achieved by x-ray diffraction analysis of this 9.3%-doped sample. Figure 4.8 displays a comparison to the commercial (40nm) ITO nano-powder used as an ICP-MS standard. The peak positions of these materials are well correlated to the ICDD card (06-0416) associated with the bixbyite structure of In_2O_3. No signals from impurity phases associated with tin oxide (SnO or SnO_2) are observed.

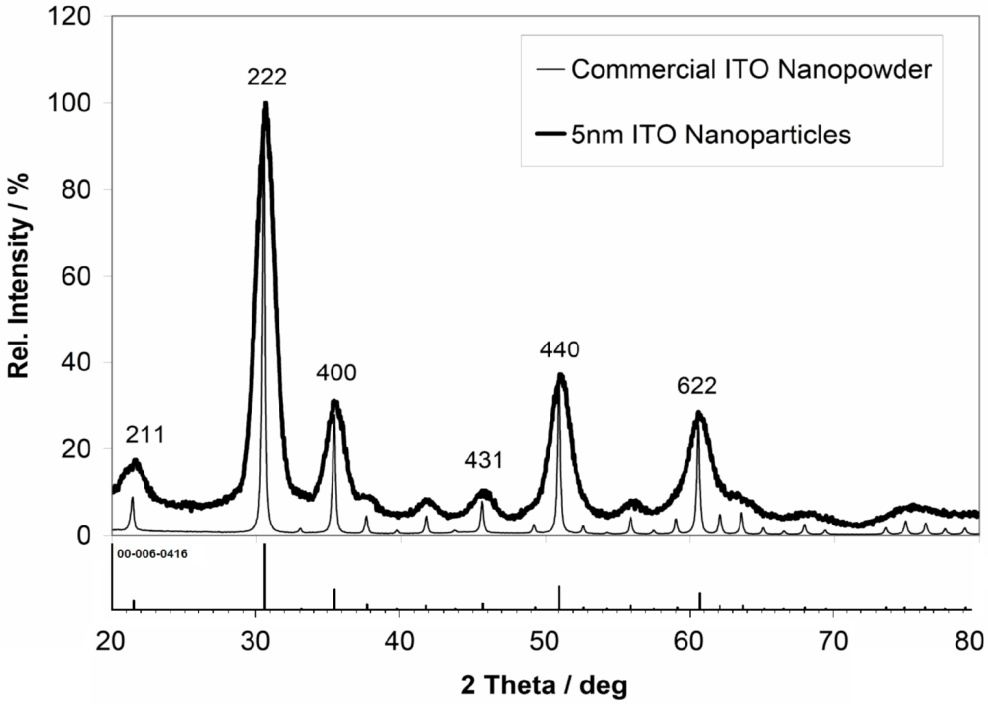

Figure 4.8: X-ray diffraction spectra of the colloidal ITO (9.3% Sn) produced in this work compared to ~40nm commercial ITO nano-powder. The peak positions associated with pure indium oxide (ICPP Card No. 06-0416) are shown as well.[5]

An estimate of average particle size can be achieved by application of the Scherrer equation to the primary reflections observed in the above x-ray spectra. The Scherrer equation can predict crystallite thickness if average diameters are smaller than 1000Å. Small differences in angle are associated with large spatial distances (inverse space). Therefore, broadening of a diffraction peak is expected to reflect some large scale feature in the crystal.[97] The Scherrer equation is obtained by taking the first derivative of Bragg's law while holding the wavelength constant and allowing both the diffraction angle and Bragg spacing to vary. Bragg's law is as,

$$2d \sin\theta = \lambda \qquad \text{Equation 4.3}$$

where, d is the lattice spacing in angstroms, θ is the diffraction angle in radians, and λ is the wavelength of x-ray utilized. Taking the derivative of both d and θ yields,

$$2(\Delta d)\cos\theta(\Delta\theta) = \lambda \qquad \text{Equation 4.4}$$

As $\Delta\theta$ can be positive or negative, the absolute value is taken to reflect the half-width of the peak. Accordingly, $2\Delta\theta$ is the peak full-width at half-height, B. As Δd reflects the crystallite thickness, the diameter of a colloidal nanoparticle is as,

$$diameter = \Delta d = \frac{\lambda}{B\cos\theta_B} \qquad \text{Equation 4.5}$$

A Gaussian function is typically used to describe the peak and accordingly, a pre-factor of 0.9 occurs and the Scherrer equation is given as,

$$diameter = \Delta d = \frac{0.9\lambda}{B\cos\theta_B} \qquad \text{Equation 4.6}$$

Application of this expression to the 222 reflection observed in Figure 4.9 indicates an average crystallite size of 5.4nm in diameter.

4.7.3 Particle Morphology

This average particle size was verified by the Transmission Electron Microscopy (TEM) image shown in Figure 4.9. The sample was prepared by placing a drop of heavily diluted colloidal ITO solution onto a carbon coated, copper grid plate. Low and high-resolution TEM micrographs along with an analysis of the particle size-distribution are presented. This image is one of three that were taken at a magnification of $290{,}000X$. The size-distribution was compiled by measuring 300 randomly selected particles from each of the three images followed by a simple averaging of the results. The size of roughly spherical particles observed is 5.2±1 nm in diameter with a slight preference for larger particles as shown in the distribution plot. As will be discussed in chapter five, the ~75% reduction in size of these particles relative to the 20nm particles of undoped In_2O_3 shown in Figure 4.5 is partially a function of tin incorporation. However, it is also likely that differences in the coordination characteristics of the specific amines used (octadecylamine vs. tris(trimethylsilyl)amine), their associated ability to mediate particle size, and differences in the amount of each used, played a role. The high-resolution scanning transmission electron microscope (STEM) image shown in the upper left inset provides evidence of the single-crystalline nature of this material as clear lattice fringes are observed. The ~2.5Å spacing seen here can be correlated to the 400 planes of the bixbyite lattice.[125] An additional high-resolution image shown in Figure 4.10 also indicates that many particles are irregularly shaped which is a potential sign of lattice distortion. Details on this will be discussed in chapter five within the context of an analysis on the effects of tin incorporation within the indium oxide lattice.

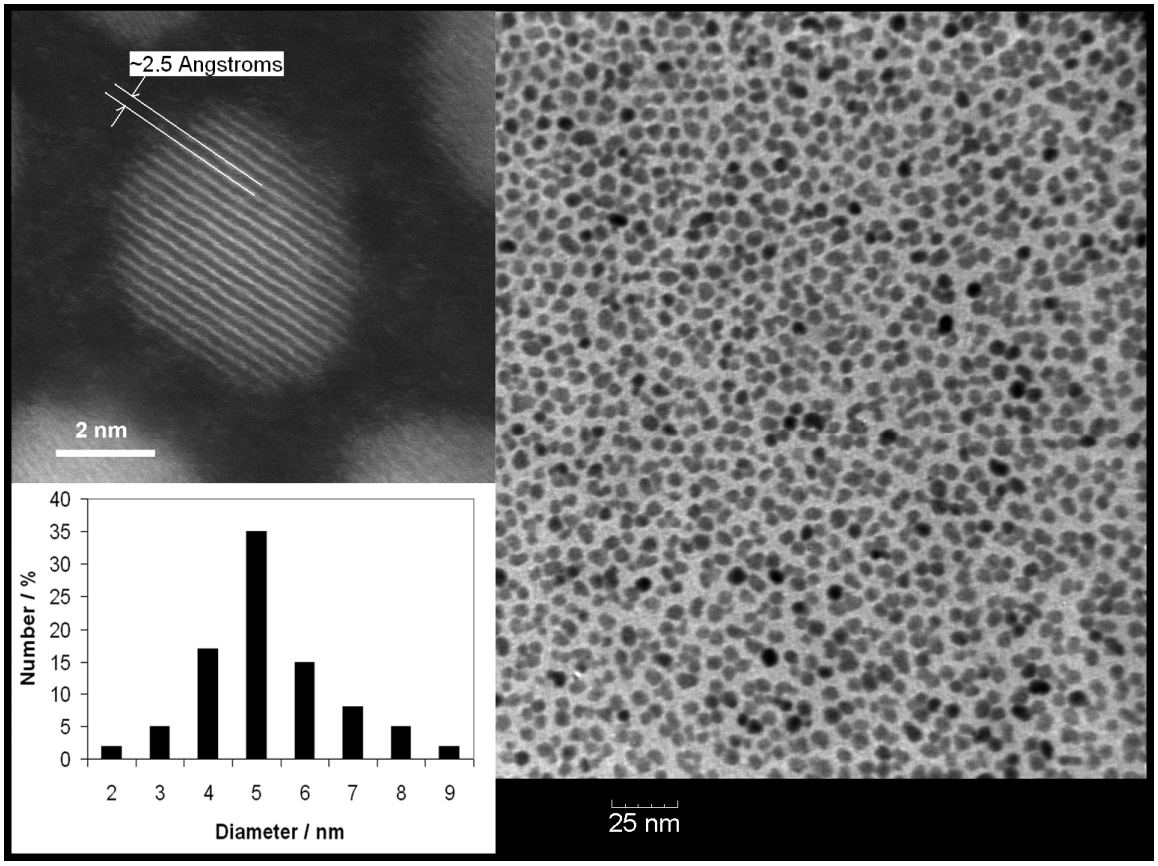

Figure 4.9: TEM analysis of the colloidal ITO dispersion shown in Figures 4.8 and 4.9. The upper and lower left insets present a high-resolution image of a single particle and the size distribution of the dispersion, respectively.[5]

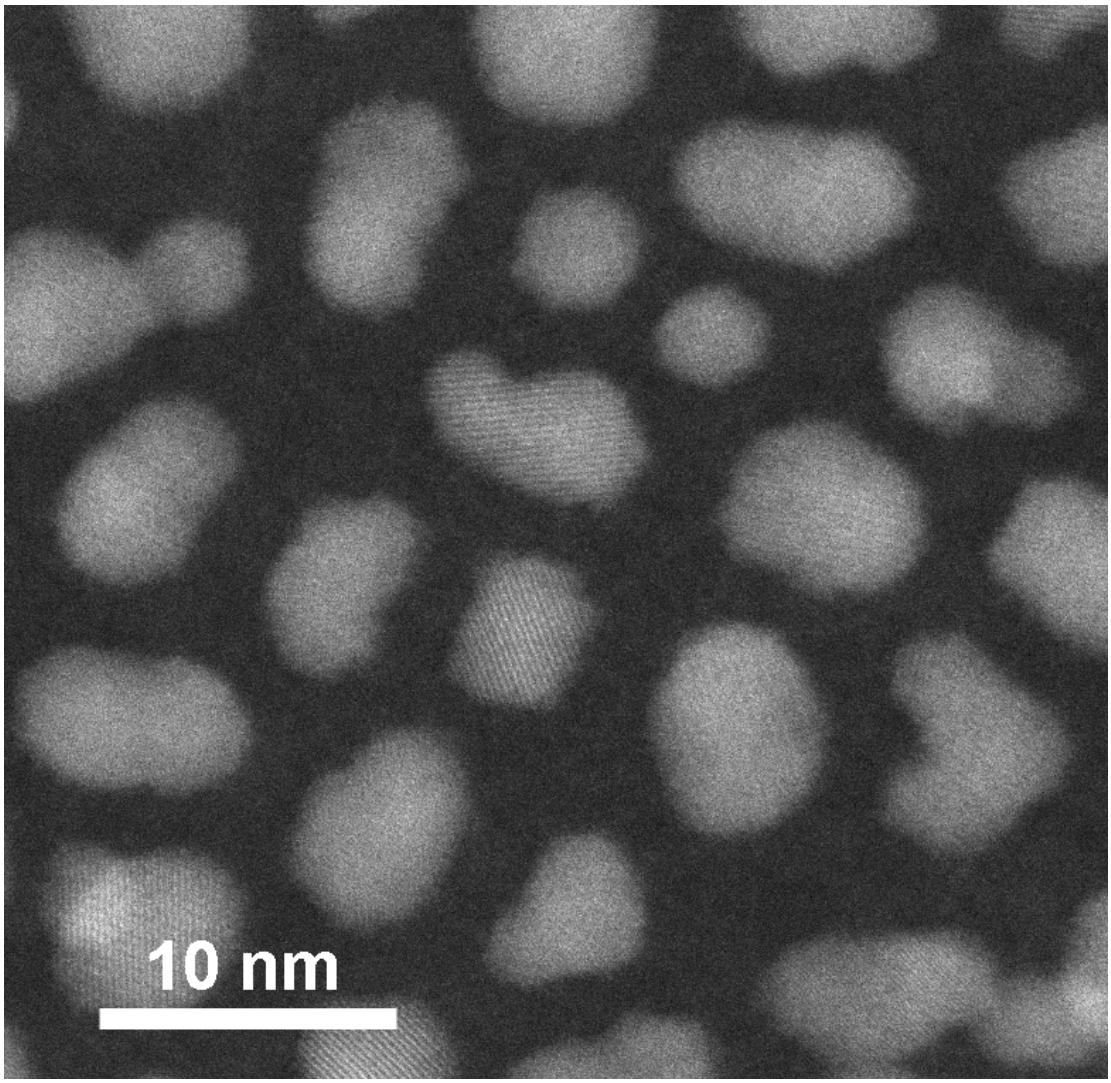

Figure 4.10: Additional High-Resolution Z-contrast STEM image of the colloidal ITO nanoparticle dispersion shown in Figure 4.10 above. The presence of distorted particles may be a consequence of dopant-induced lattice strain of the type previously discussed in section 4.3.

4.7.4 Surface Ligand Character

FT-IR analysis was used to determine surface characteristics of the colloidal ITO formed (Figure 4.11a). A dilute solution of purified particles dispersed in chloroform was again injected between calcium fluoride plates for subsequent analysis. The C-O stretch (1700 cm^{-1}) and C-H stretch (2850 – 3100 cm^{-1}) of carboxylic acid are both clearly observed in the spectra and indicate the presence of myristate ligands.[126, 127] Thermogravimetric analysis (TGA) was performed on this system to estimate the ratio of ligand to crystalline ITO particle. The sample was heated in an air atmosphere from room temperature to 500 ˚C at a rate of 10 ˚C per minute and then held at that final temperature for approximately 10 minutes to ensure complete removal of all volatile materials. The TGA plot presented in Figure 4.11b indicates a volatile mass loss of 18.7% which represents the organic ligand content with a minor contribution from adsorbed water.

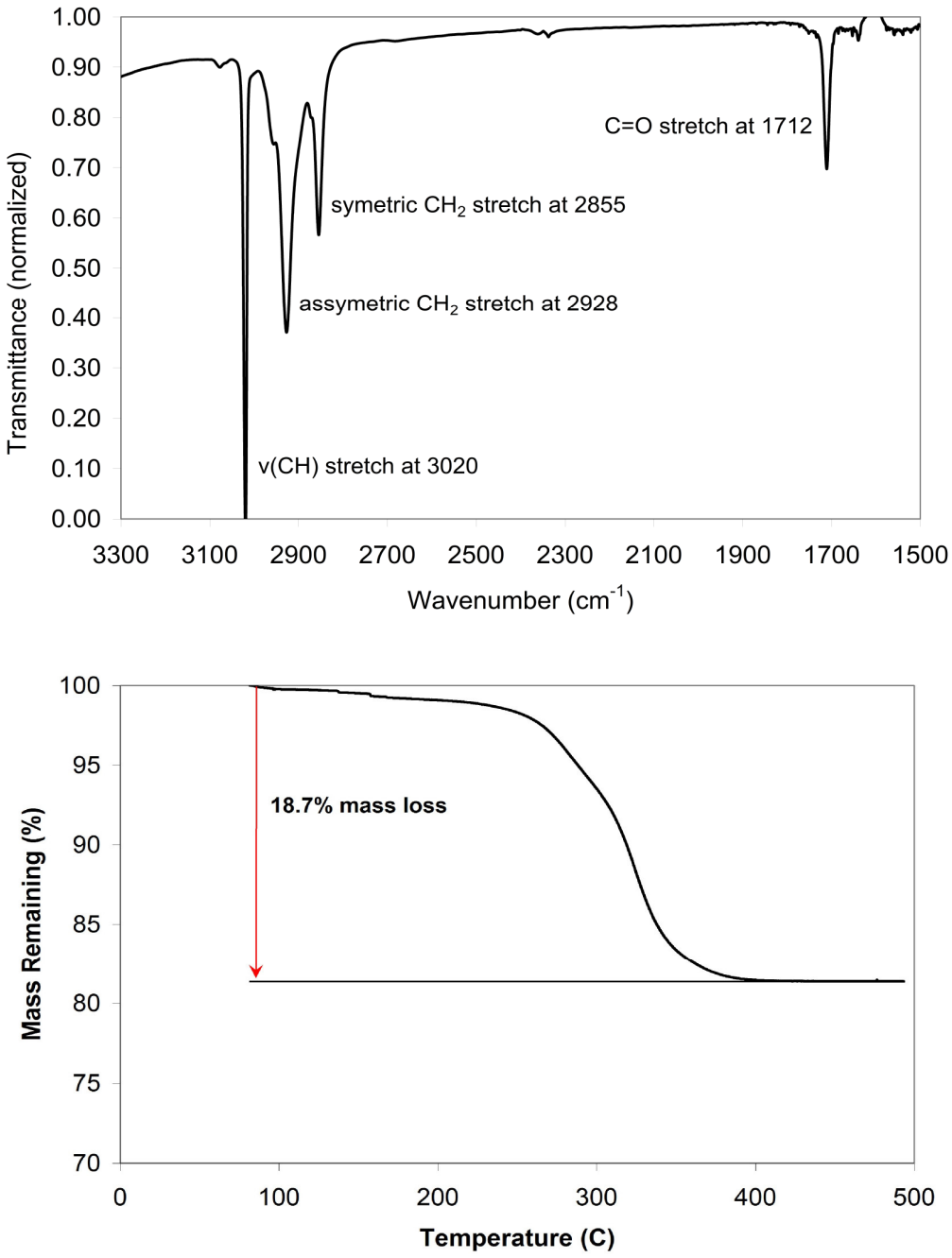

Figure 4.11: (a) FT-IR spectra of colloidal ITO dispersed in chloroform. The C-O stretch (1712 cm^{-1}) and C-H stretch (2850 – 3000 cm^{-1}) indicate the presence of myristic acid ligands. Also present is a prominent N-H stretch from the amine group at 3020 cm^{-1} which points to a mixed ligand character. (b) TGA analysis indicates ~19% of the dispersed particle mass is composed of these organic structures.

4.7.5 Optical Properties

As discussed in the background section, the presence of free electrons in ITO can be identified by their effect on the material's optical properties. This has traditionally been determined by analysis of thin-film forms of the material which are greatly influenced by deposition procedures.[49] The optical clarity of a colloidal ITO dispersion as displayed in Figure 4.8 however, allows direct optical analysis of single crystalline particles using a standard UV-VIS-NIR spectrophotometer. Transmission spectra of this material and an undoped indium oxide colloidal nanoparticle dispersion are presented in Figure 4.12a. The presence of a high free electron concentration in the ITO material is immediately apparent by the strong reflection edge observed in the long wavelength (>800nm) regime. Recall that this is due to the motion of free electrons in phase with lower frequency light and is definitive proof of their presence in the material.[38] The spectral position of the absorption edge of ITO is also influenced by free electrons which produce a blue shift with respect to the undoped In_2O_3 shown. Specific steps were taken to ensure that the concentration of particles in solution was the same for both materials shown and accordingly, this shift is purely a function of intrinsic material properties rather than a Beer-Lambert optical effect.[128] When continuously diluted with additional hexane, the Beer-Lambert effect expands the transparent optical window as shown in Figure 4.12b. This simple behavior of the colloidal ITO dispersion may lead to its incorporation within a variety of novel composite materials requiring wavelength filtering.

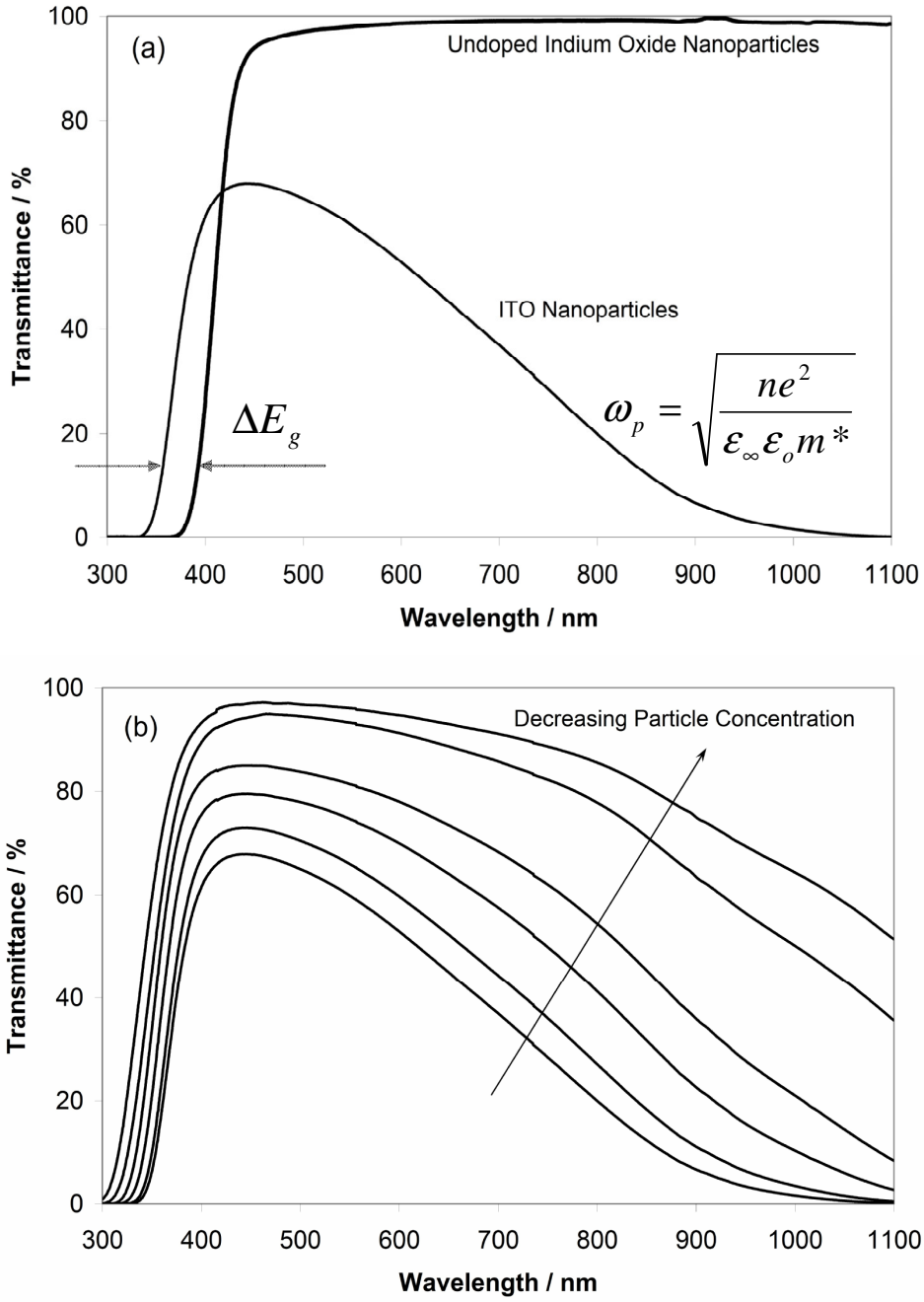

Figure 4.12: (a) Transmission spectra of colloidal dispersions of undoped Indium Oxide and ITO nanoparticles dispersed in hexane. The long wavelength reflection edge and blue-shift in the absorption edge are both an indication of free electrons in the ITO lattice. (b) Progressive solvent dilution of the ITO dispersion creates a classic Beer-Lambert effect.[5]

4.8 Summary

A definitive identification of ITO has been made for the colloidal nanoparticle dispersion produced in this work. ICP-MS analysis of a 10% doped sample shows that the nanoparticles are composed of 90.7% indium and 9.3% tin. X-ray diffraction indicates that this tin is fully incorporated into the indium oxide bixbyite lattice with no occurrence of separate tin oxide phases. TEM imaging indicates that these particles possess an essentially single crystal character and display a very narrow size-distribution. Evidence of excess conduction band electrons was found in the colloidal ITO system through the appearance of an infrared reflection edge and ultraviolet band gap absorption blue-shift in optical transmission spectra. The formation of this colloidal nanoparticle form was achieved by a solution-based synthesis protocol which relies on metal fatty-acid salts, primary amines, and a non-coordinating hydrocarbon solvent. FT-IR analysis of this reaction indicated that the entire process is driven by a series of intense nucleophilic substitution reactions (aminolysis, condensation, and hydrolysis).[116, 122]

CHAPTER 5

INTRINSIC PROPERTY ANALYSIS

5.1 Introduction

As previously discussed in the introduction and background sections, a majority of what is known about ITO is based on measured properties of sputter-coated thin film samples which are significantly affected by various deposition parameters (temperature, pO_2, sputter rate, etc…).[49] The colloidal nanoparticle form developed in the present dissertation work affords the unique ability to analyze the intrinsic material properties of single crystals of ITO prior to any film deposition procedures or other treatment. In contrast to polycrystalline thin-film forms of the material, an individual colloidal ITO particle may be able to entirely confine excess conduction band electrons within its boundaries. Monitoring the generation of these charge carriers by their influence on the optical properties of colloidal dispersions allow the fundamental issues of individual particle formation and conduction band filling to be addressed. In fact, the very origin of these excess electrons may be investigated by correlating the optical properties of ITO particles to variations in their internal lattice structure. The evolution of optical properties, free electron concentration, and lattice structure can also be correlated to the system composition by a variation in Sn dopant concentration.

5.2 Colloidal ITO Particle Formation

From the very instant of amine injection, a solution of colloidal ITO nanoparticles is optically transparent which offers an opportunity to analyze the system formation by

evaluating the evolution of its absorption and reflection edges. In-situ spectroscopy was used to monitor the transmission spectra of a colloidal ITO dispersion from the point of reaction initiation through the next thirty (30) seconds. A high-temperature dip probe was immersed into the reaction solution and full spectra were recorded with a high-speed spectrometer at 30ms intervals. Due to an equipment limitation, samples were made with a concentration of precursors high enough to ensure the appearance of the reflection edge within the 300-800nm spectral window. Figure 5.1 presents the series of transmission spectra taken directly from the reaction solution during the 30 seconds immediately following amine injection.

The period between 0 and 3.5 seconds is characterized by a clear nucleation and growth process. While there may be an element of Beer-Lambert effects due to a rapid increase in particle concentration during this time, the progressive absorption edge shift to longer wavelength (lower energy) is consistent with a semiconductor moving from a highly confined state (100s of atoms) to one of lower confinement (1000s of atoms).[16] This behavior has previously been noted for the nucleation and growth of CdSe quantum dots in which similar in-situ analysis was performed.[129] While it is possible that the formation of a reflectance edge at longer wavelengths has begun, its absence from the 300-800nm region shown within the 0-3.5 second interval indicates the material is not yet highly degenerate in nature.[67] It is tempting to speculate that this is indicative of a pure In_2O_3 core and thus, added verification of the model for doped nanoparticle composition proposed by Schwartz and co-workers.[36] However, it will be shown in the next section that the generation of free electrons in this colloidal form, continues over a period of

several days. Accordingly, it is also possible that incorporated Sn dopants have not yet become electrically active in the 0-3.5 second period following reaction initiation.

The first indication of a reflection edge within the spectral window probed is observed from 3.5 to 4 seconds and coincides with an abrupt halt of further absorption edge red-shift for the period from 4 to 9 seconds. This may be due to competing forces of continued particle growth which reduces the band gap energy and progressive conduction band filling which serves to expand its apparent value. The period from 9 to 30 seconds displays the continued formation of the reflection edge and a clear blue-shift of the absorption edge in classic Burstein-Moss fashion.[70, 71] It is unknown at this point whether particle growth has subsided completely or if the effects of conduction band filling on the apparent absorption band edge position now dominate.

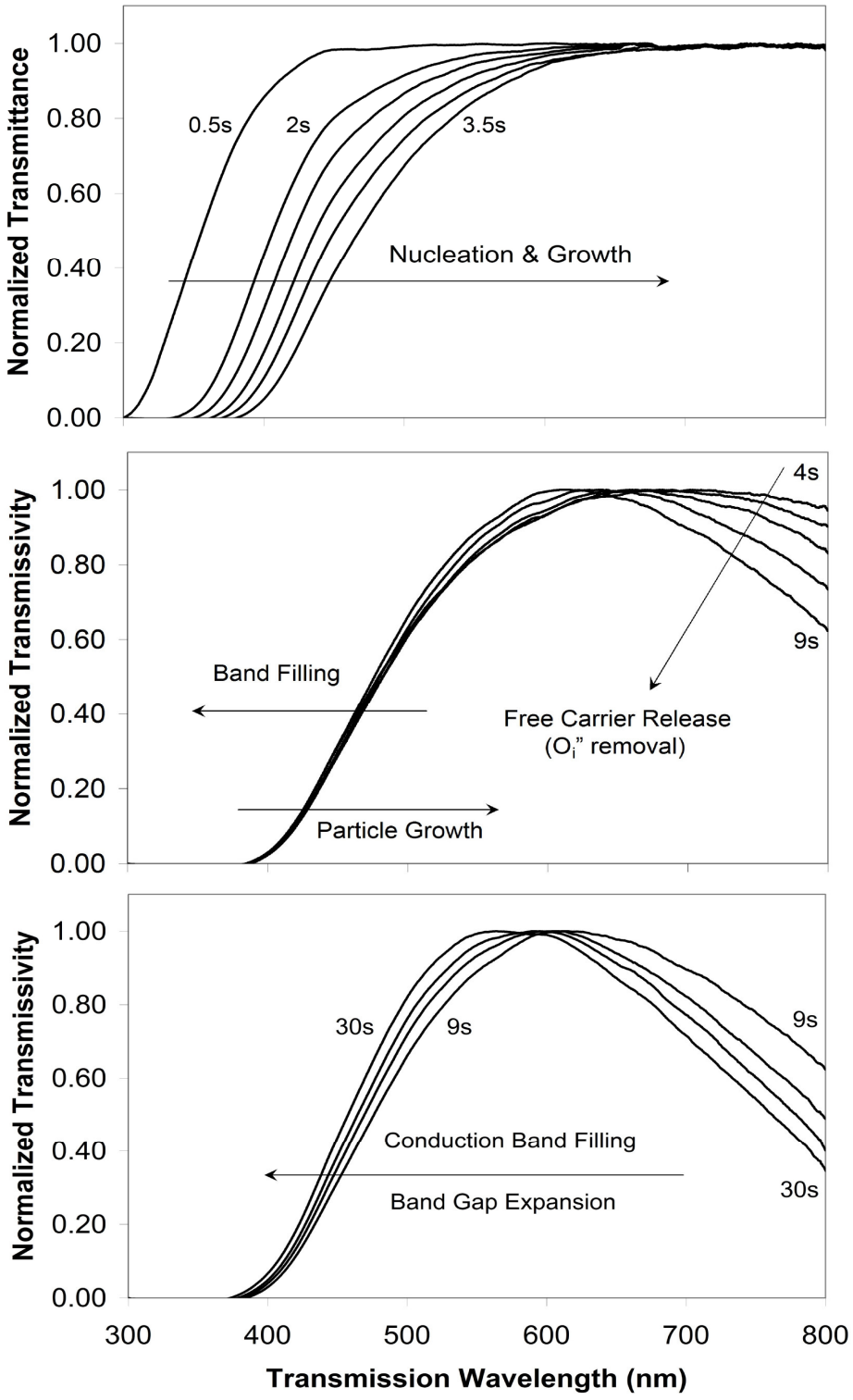

Figure 5.1: In-situ spectroscopic monitoring of colloidal ITO nanoparticle formation. Normalized transmission spectra correspond to optical behavior over the first 30 seconds following primary amine injection and associated reaction initiation.

5.3 Analysis of Conduction Band Filling

As described in section 4.8.1 and again in the previous discussion, the absorption edge of colloidal ITO continues to shift progressively to lower wavelength (higher energy) as excess conduction band electrons are generated in the material over a two to three day period. Valence to conduction band transitions are therefore, forced into progressively higher energy states as described by the Burstein-Moss model.[70] This behavior is displayed in the transmission spectra of Figure 5.2 and is also readily observed by a change in the dispersion body color from green to blue. Following collection and purification, transmission spectra of the colloidal ITO system were collected at various time points over the 48 hours following synthesis with a UV-VIS-NIR spectrophotometer. Great care was taken to ensure that the concentration of particles in solution remained unchanged between measurements. Note however, that any evaporation of the dispersing solvent would produce a higher concentration of solute resulting in a red-shift of the measured absorption edge position rather than the blue-shift observed. The absorption edge shift first observed at 9 seconds in Figure 5.1 continued to progress over the next 48 hours. Advantage was taken of this behavior for an analysis of conduction band filling and any potential influence of electron confinement. Analytical expressions describing the relationship between free-electron concentration and band gap expansion are known for carrier concentrations both below and above the Mott criteria for a semiconductor-to-metal transition in ITO (equations 2.41 and 2.42). Accordingly, one may estimate the specific free electron concentration required to produce an experimentally measured band gap expansion. Absorption spectra were taken at three hour intervals to develop a detailed record of this expansion over the 120 hours following reaction initiation.

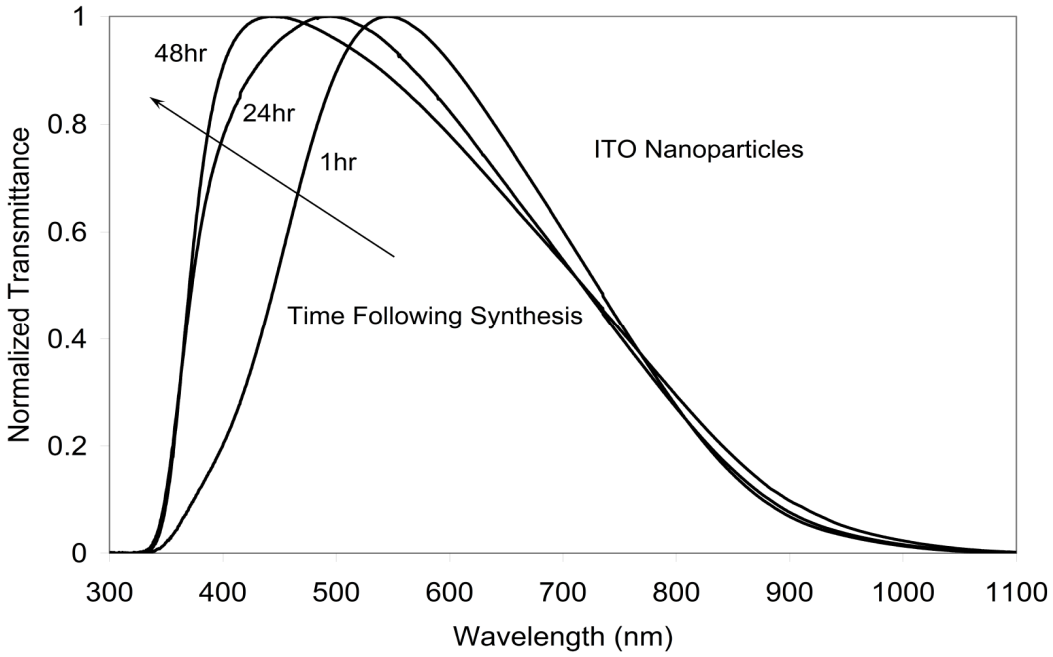

Figure 5.2: Normalized transmission spectra of a colloidal ITO sample containing ~9.3% Sn doping. The spectral shift over 48 hours indicates progressive generation of excess electrons within the materials conduction band structure. The change in solution body color associated with this shift was previously displayed in Figure 4.8.

The method used for the calculation of any band gap shift must be both accurate and consistent because estimation of free electron concentration will rely solely on this value. A standard equation used to determine band gap E_g from optical spectra is,[130, 131]

$$\alpha h\nu = C(h\nu - E_g)^n \qquad \text{Equation 5.1}$$

where $n=1/2$ for a direct gap semiconductor like In_2O_3, C is a material based constant, $h\nu$ is the incident photon energy in electron volts eV, and α is the absorption coefficient in cm^{-1}. A plot relating the square of the absorption coefficient (α^2) to the incident photon energy ($h\nu$) is often used for a fairly accurate estimate of the dispersed material's intrinsic

band gap by extending the linear portion of the curve to $\alpha^2=0$. Implicit in this estimate-based approach is the assumption that α has been properly determined for each incident photon energy. A standard method often used is the Beer-Lambert approximation as,

$$A = \alpha l \qquad \text{Equation 5.2}$$

where, A is the measured absorbance and l = 1cm for the typical quartz cuvette used in this type of measurement. This expression is valid only under the strict condition that a minimum of shadowing effects have occurred.[128] This phenomenon is caused when photons are absorbed by two or more particles positioned in a row which is parallel to the incident beam path and results in a greater absorptivity value than actually warranted. Accordingly, it is common practice to use a heavily diluted colloidal solution and the results of this treatment are sufficient for the majority of analyses. In the present case however, there must be an absolute minimum of error present in band gap measurement and this requires application of the full material-concentration-dependent form of the Beer-Lambert law as,

$$A = \in lc \qquad \text{Equation 5.3}$$

where, $\in$ is the molar absorptivity and c is the molar concentration in solution. The present work utilizes an expression derived by Kormann and co-workers for application to colloidal TiO_2 nanoparticles in solution,[132]

$$\alpha = \frac{2.303\rho 10^3}{lc} A \qquad \text{Equation 5.4}$$

where, ρ is the material density in g/cm^3 and c is its concentration in solution as g/L. The 2.303 factor is a consequence of the derivation and is equal to *ln(10).* As the atomic masses of tin and indium are almost identical, the density of undoped indium oxide was used for calculations as 7.18 g/cm^3. Figure 5.3 shows an example of analysis done for the system displayed in Figure 5.2 at 48 hours following reaction initiation. The concentration in solution *c*, was determined by precisely weighing the amount of ITO (minus ligands) present in ~1ml of dispersing solvent. The colloidal dispersion was then diluted with measured quantities of the solvent as transmission/absorption spectra were taken at each step (Figure 5.3a). A fundamental feature of the (α^2 *vs hv*) plot is that it tends to a single curve for the limiting case of *c=0* as shown in Figure 5.3b. The measured band gaps, for undoped In_2O_3 and ITO (9.3% Sn), were determined as ~3.55eV and ~3.88eV, respectively. If treated as a bulk material, this indicates that the apparent band gap of this colloidal ITO sample has experienced an expansion ΔE_g of ~0.33eV due to the generation of excess electrons within its conduction band structure.

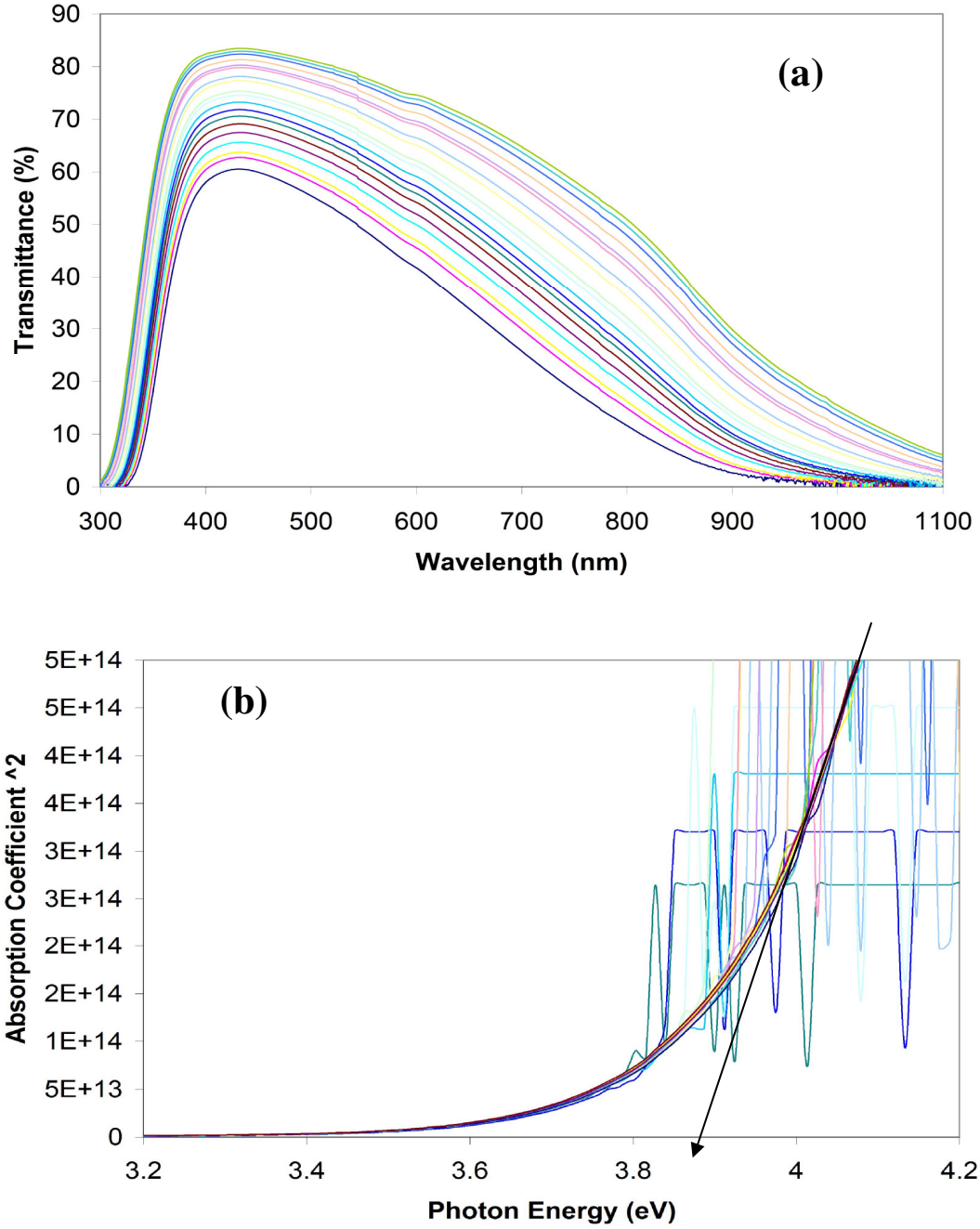

Figure 5.3: Estimate of the band gap for a colloidal ITO nanoparticle dispersion using a material-dependent form of the Beer-Lambert law. (a) Transmission spectra showing the effects of progressive dilution with additional solvent. (b) The effects of this dilution on the (α^2 vs. $h\nu$) plot used to determine the system band gap. Extending the linear portion of the curve to $\alpha^2 = 0$, yields an estimate of the band gap value in electron-volts.

The temporal variation in apparent band gap expansion for the colloidal ITO dispersion is presented in Figure 5.4. Again, all data points are with respect to the measured band gap of an undoped colloidal dispersion of In_2O_3 nanoparticles made using the same synthesis approach. An initial band gap expansion of 0.18eV is already present approximately two hours following reaction initiation. This expansion continues to progress over the next 118 hours with a steady state of 0.34eV reached after approximately 72 hours. As determined by high resolution x-ray diffraction, the particle size (~5.5nm) was unchanged during the analysis period and thus, any increase in band gap expansion observed is purely a function of free carrier generation in the lattice rather than some quantum confinement effects. In other words, this band gap expansion did not occur due to a shrinking particle size. However, the degree to which upper conduction band states (1s, 1p, 1d, etc…) are stretched apart could certainly influence the results (refer to Figures 2.11 and 2.13). As discussed in the background (section 2.6.3), an accepted analytical treatment on the effects of quantum confinement in heavily degenerate semiconductors like ITO is currently unavailable. Accordingly, analysis was performed in the present dissertation work assuming the two limiting cases:

No Quantum Confinement. This assumes that excess conduction band electrons are entirely free and their concentration in the ITO lattice can be estimated using the established relationships to conduction and valence band dispersions previously described in section 2.5 of the background chapter.

Classic Quantum Confinement. This assumes that excess conduction band electrons are entirely confined within each nanoparticle boundary. Energy levels are now located at discrete positions and hold a finite number of electrons depending upon degeneracy.

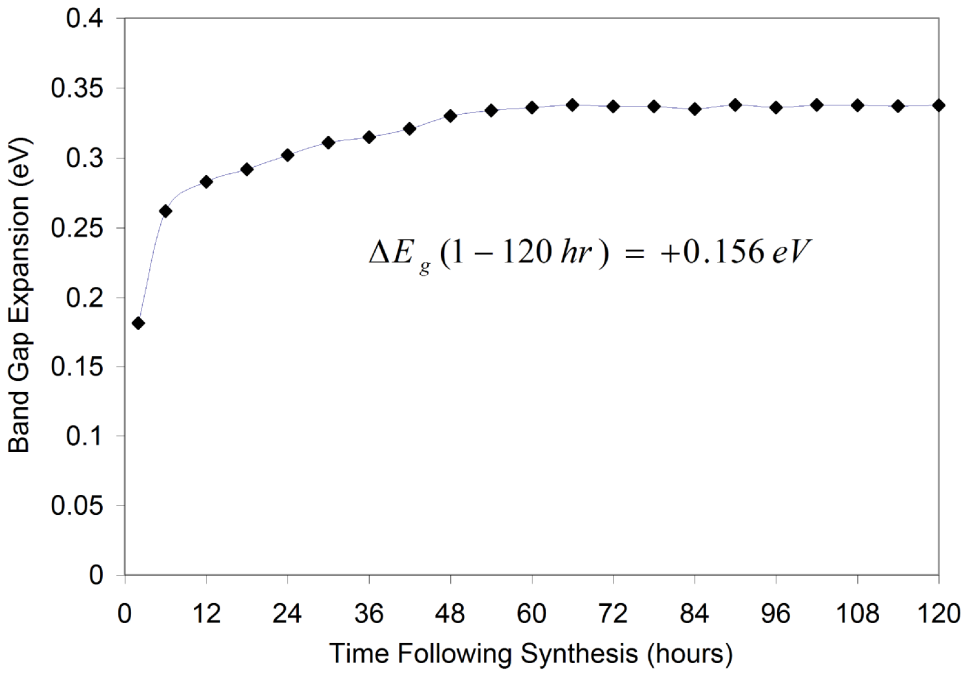

Figure 5.4: Temporal evolution of the measured band gap expansion for a colloidal ITO sample containing ~9% Sn doping. The expansion values given were determined by subtracting the band gap of an undoped colloidal In_2O_3 nanoparticle system from the measured band gap of the ITO sample at each time point.

5.3.1 Analysis Assuming No Quantum Confinement

Utilizing ΔE_g data to estimate intrinsic ***free*** electron concentration relies on the fundamental expressions for conduction band filling and many-body interactions described in the background section 2.5.3. As previously determined, the Mott critical free electron concentration N_c in ITO is on the order of $5.62x10^{18}\,cm^{-1}$. It is at this point, that a semiconductor-to-metal transition takes place and the material begins to exhibit highly degenerate characteristics like low temperature conductivity.[2] For free electron concentrations just below this value, the associated degree of band gap expansion, relative to an undoped material, can be estimated using the Burstein-Moss band filling effect only (Equation 2.41). This treatment indicates that the value of N_c described above

for ITO would produce a band gap expansion ΔE_g of ~0.05eV. Accordingly, for all cases in which the band gap expansion utilized for free carrier estimation is greater than this 0.05eV value, the effects of many-body interactions must be included. For a first approximation that includes band gap narrowing due to exchange interactions only, the following expression for the effects of free electron concentration *n* has been utilized,

$$\Delta E_g = \frac{\hbar^2}{2m_{vc}^*}(3\pi^2 n)^{2/3} - \frac{e^2}{2\varepsilon_\infty \pi^2}(3\pi^2 n)^{1/3} \qquad \text{Equation 5.5}$$

This was derived by a combination of equations 2.35, 2.41, and 2.42 in the background section. It has been shown that use of an expression such as this which neglects screening may result in a slight over-estimation of the band gap narrowing effect and accordingly, an under-estimation of the associated free electron concentration.[69] It has been used for the present work in an effort to be conservative in calculations. Noting the quadratic form provided by $(n^{1/3})^2$ and $(n^{1/3})$, this expression can be re-written for the calculation of *n* as,

$$n = \frac{(m_{vc}^*)^3}{874.82\hbar^6}\left\{\frac{0.157e^2}{\varepsilon_\infty} + \sqrt{\left(\frac{0.157e^2}{\varepsilon_\infty}\right)^2 + 4\left(\frac{4.782\hbar^2}{m_{vc}^*}\right)\Delta E_g}\right\}^3 \qquad \text{Equation 5.6}$$

The process of ***free*** electron estimation assuming no quantum confinement (bulk) is then,

1. Determine the absorption coefficient from transmission data using equation 5.4.
2. Estimate the band gap widening using the (α^2 *vs* $h\nu$) plot.
3. Calculate free electron concentration n using equation 5.6 above.

As displayed in Figure 5.5, this procedure indicates that a free electron concentration of $\sim 1.75\times10^{20}\,cm^{-3}$ is capable of producing the experimentally observed band gap shift at 120 hours following synthesis. It is important at this point to note that this estimated value is within the range of measured free electron concentrations found in sputter coated ITO thin-film polycrystalline samples. When the average particle size of ~5.5nm is considered, this value can be converted to an average of ~14 ***free*** conduction band electrons per colloidal particle. The increase in free electron concentration and average number of free conduction band electrons per particle over the analysis period of 118 hours was $\sim 9\times10^{19}\,cm^{-3}$ and ~7, respectively.

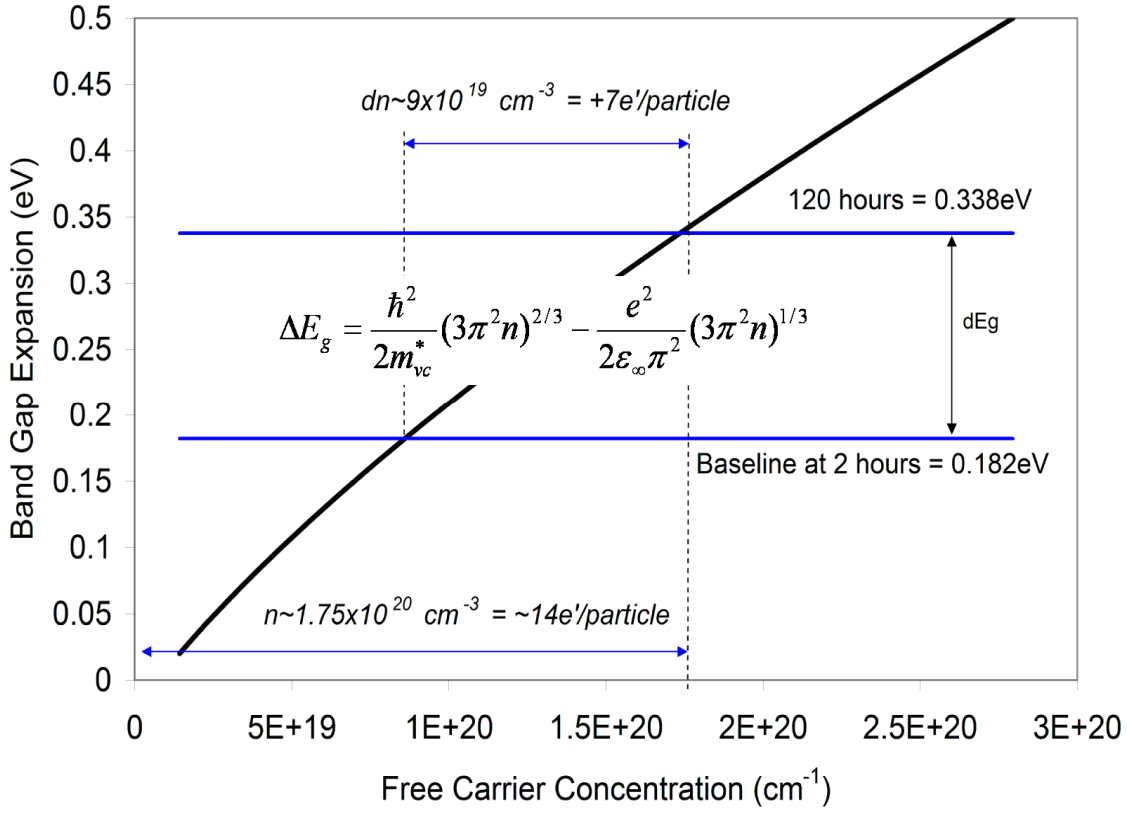

Figure 5.5: Estimation of free electron concentration in colloidal ITO from the measured band gap expansion observed over the 120 hour analysis period. The thick-lined curve represents equation 5.5 with the effective masses and dielectric constant characteristic of bulk ITO. It is estimated that approximately 14 ***free*** conduction band electrons per particle are capable of producing the observed band gap expansion at 120 hours (relative to an undoped colloidal In_2O_3 sample). It is also estimated that approximately 7 free conduction band electrons per particle were generated during the analysis period. The above analysis assumes that excess electrons are "entirely free" within the nanoparticle lattice and that bulk-like band dispersions may be applied.

5.3.2 Analysis Including Quantum Confinement

The inclusion of quantum confinement in the estimation of ***confined*** excess electron concentration relies on the effective mass approximation (EMA) discussed in section 2.6.2 of the background chapter.[16-18] As previously displayed in Figure 4.10, the size of colloidal ITO particles for this sample ranges from ~4.5nm to ~6.5nm in diameter. Accordingly, the theoretical position of conduction band energy levels calculated with the EMA approach will display a rather wide variation as shown in Figure 5.6 below. When this potential effect is overlaid onto the plot of ΔE_g versus time, an estimate of energy level location within the resultant conduction band structure of the colloidal ITO dispersion is achieved (Figure 5.7). The transition energy in electron volts may now correspond directly to the number of confined excess conduction band electrons per particle. As discussed in section 2.6 and displayed in Table 2.3, the effective density of states for the 1s conduction level in a 3-dimensional confined sphere is a scalar quantity and equal to 2.[2] This corresponds to the two allowed spin states (i.e., spin up and spin down). Similarly, the number of electrons allowed in the 1p and 1d levels is 6 and 10, respectively. Figure 5.7 indicates that an average of 8 excess electrons (2 in 1s + 6 in 1p) confined within each colloidal ITO particle is capable of producing the observed band gap expansion at 120 hours. This value differs significantly from the 14 electrons per particle estimated using a bulk-like band dispersion approach and it is likely that the true number is found somewhere in between these two limiting cases. It is however, interesting to note that the sharp rise in band gap expansion observed between 3 and 6 hours following synthesis precisely coincides with a separation between calculated 1s and 1p energy levels. As will be discussed, this may instead be a jump between 1p and 1d.

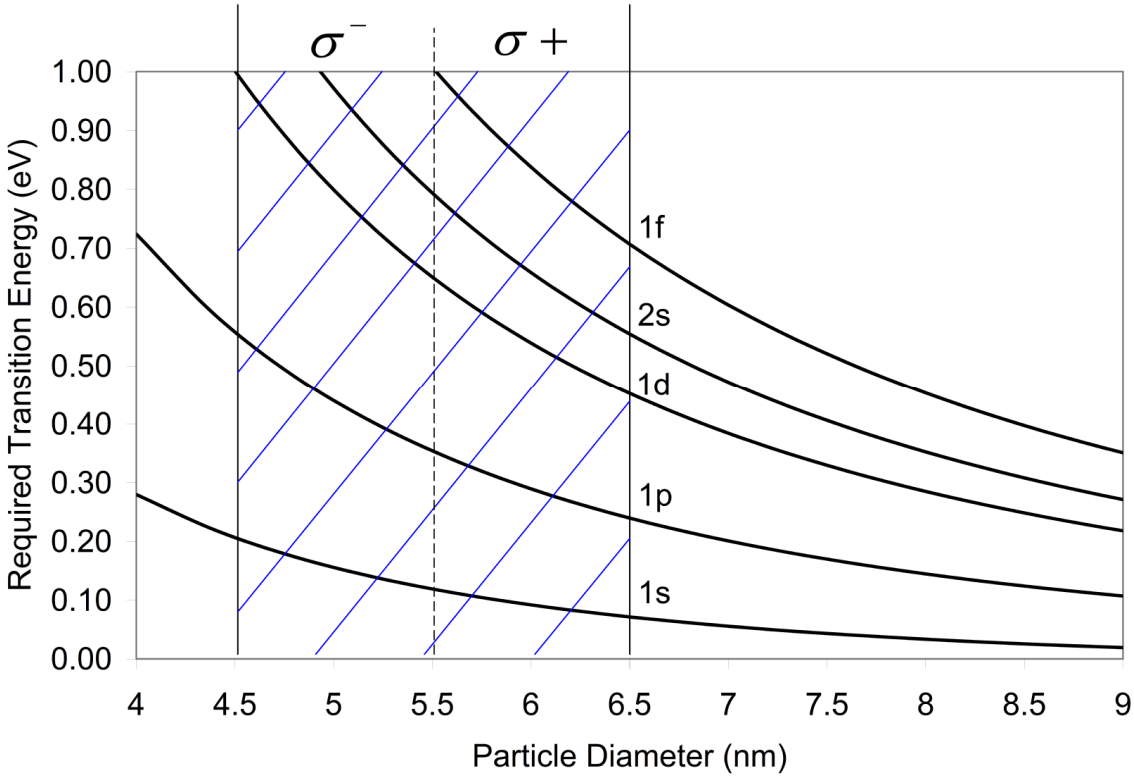

Figure 5.6: Theoretical variation of the available conduction band electron energy levels with diameter for a ~5.5nm colloidal In_2O_3 nanoparticle system that displays a 2nm size distribution. This region is highlighted by the hatched area shown.

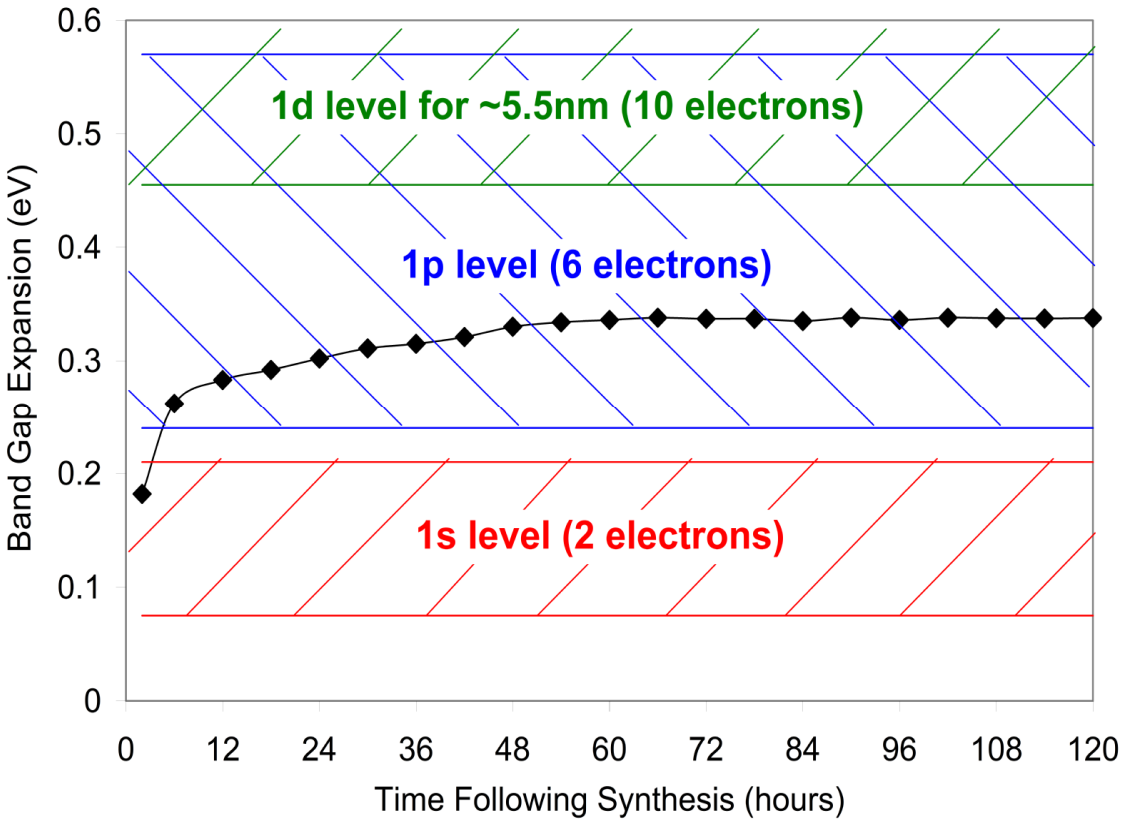

Figure 5.7: Comparison of the experimentally determined colloidal ITO band gap expansion to the confined conduction band energy levels calculated using EMA theory and displayed in Figure 5.6 above. The hatched areas display the estimated width of these theoretical regions in light of a 2nm particle size distribution. This data indicates that an average of 8 ***confined*** excess conduction band electrons per particle is capable of producing the observed band gap expansion. Note the potential level jump from 1s to 1p between 3 and 6 hours following reaction initiation.

Although it is well known that the effective mass of conduction band electrons increases as their concentration is increased in a semiconductor lattice,[43, 74-83] general use of the Burstein-Moss model makes a key assumption that the effective mass of electrons and holes are a constant regardless of their concentration. While this treatment is not significant for bulk materials, its influence in the case of a quantized system may be important.[69] The effective electron mass, m_c^*, is found in the denominator of Equation 2.55 describing the Bohr radius of a semiconductor. Accordingly, an increase in the electron effective mass will reduce the Bohr radius and produce a shift in the onset of quantum confinement effects to even smaller particle dimensions. Additionally, it is also well known that the effective mass approximation routinely over-estimates the quantum confinement phenomena because it assumes a hard sphere model and does not take into account surface defect states in individual crystallites.[133] A more accurate description of electron confinement within a semiconductor nanoparticle is based on a consideration that the potential barrier is finite with a tunneling decay length r_t of approximately 0.5nm for a typical system. Because the kinetic energy strongly depends on the volume in which the electron is confined, penetration outside the crystallite may reduce the energy of the electron considerably (20-25% for semiconductors with a diameter from 2-7nm).[88] The finite nature of a particle's surface potential barrier and the influence of a periodic lattice containing defects are taken into consideration through the Tight Binding Model. This approach models nanoparticle electronic states starting from the limit of isolated atomic orbitals.[94, 133] The difference between EMA and TB models is highlighted in Figure 5.8 which shows the 1s, 1p, 1d, 2s, and 1f conduction band energy levels calculated for the ZnO system by Roest.[6, 91, 93] Note that where the EMA dictates a given

transition energy is to the 1p state, the TB model indicates the 1d state has already been reached. These factors indicate that the 1d conduction band energy state shown in Figures 5.6 and 5.7 may have become available for filling at the ~5.5nm ITO particle size produced. This would increase the potential number of electrons per particle from 8 to 18. A colloidal ITO dispersion displaying an even more monodisperse size-distribution and application of the Tight Binding method are required for a more precise analysis.

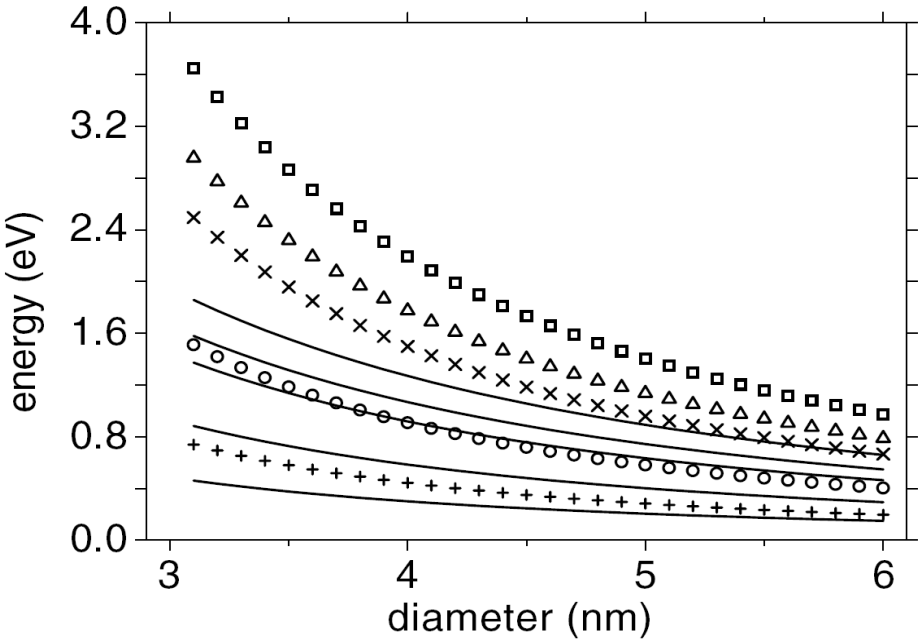

Figure 5.8: Kinetic confinement energies of the conduction band levels for a ZnO quantum dot, as a function of particle diameter. Solid lines were calculated with the tight-binding model (bottom to top; 1s, 1p, 1d, 2s, 1f). Symbols represent energy level predictions using the effective mass approximation: 1s(+), 1p(○), 1d(×), 2s(Δ), and 1f(□).[6]

5.4 Origin of Excess Electrons in Colloidal ITO

According to the Frank and Kostlin defect model of ITO, free electron generation is caused by the progressive removal of "reducible" interstitial oxygen.[52] Evidence of this removal has previously been gathered by neutron diffraction data obtained from both thin films and commercial nanopowders treated under reducing atmospheres.[54] The present work makes use of the influence that tin doping has on internal lattice structure to offer additional support for the Frank and Kostlin defect model. It is known that the indium oxide lattice parameter expands beyond the undoped value of 10.117Å as tin is incorporated.[52, 134-137] Although the radius of Sn^{4+} (0.71Å) is smaller than the In^{3+} (0.81Å) for which it substitutes, the net positive charge associated with its incorporation results in an electrostatic repulsive force that serves to expand the doped lattice.[54] It has been suggested that incorporated oxygen interstitials, which are present to accommodate this charge imbalance, would partially screen the repulsive force.[52] Accordingly, it was theorized that the removal of these screening species could be identified in colloidal ITO by an observed lattice expansion due to progressively stronger electrostatic repulsive forces.

With this in mind, the degree of both band gap and lattice parameter expansion were compared for the sample displayed in Figure 5.4 above. High-resolution x-ray measurements were taken within 30 minutes of selected transmission measurements and a Pseudo-Voigt peak profile fitting regime was utilized, in conjunction with JADE software, to determine the lattice parameter at each time point. As shown in Figure 5.9, an expansion from ~10.131Å to 10.137Å occurred over the analysis period and its trend is very well correlated to the observed band gap expansion.

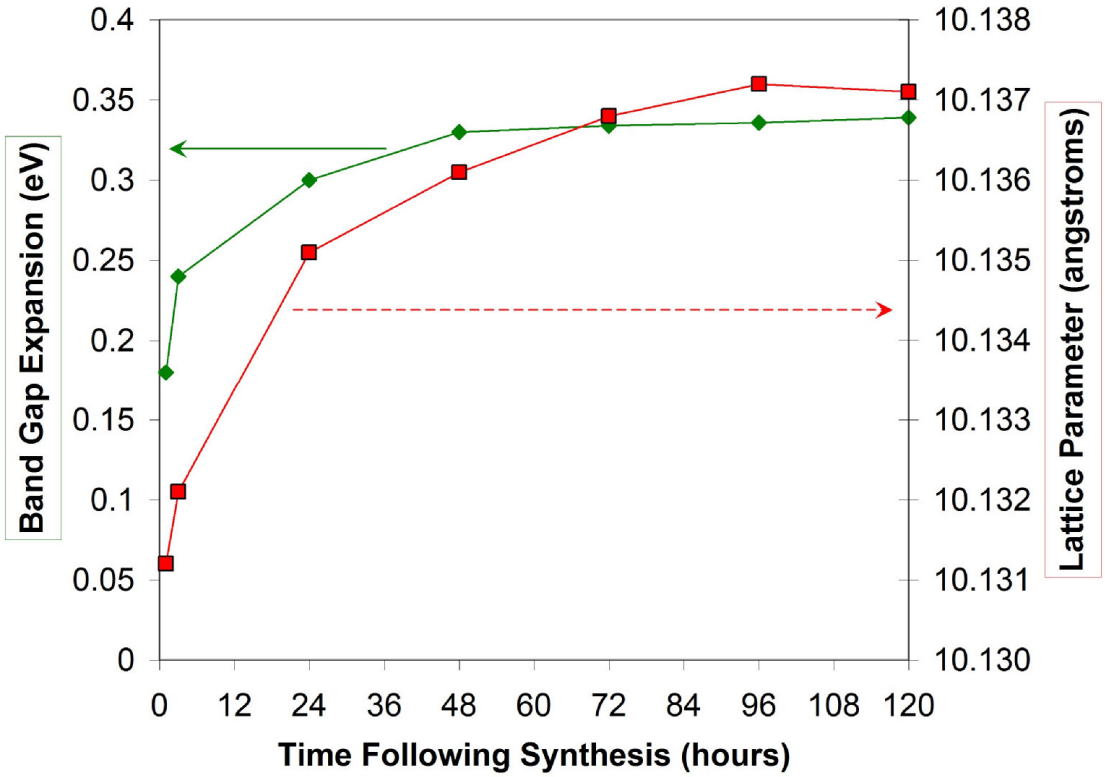

Figure 5.9: Time variation of the measured band gap expansion and measured lattice parameter for colloidal ITO over the 120 hour analysis period. The good correlation between these two trends lends support to the Frank and Kostlin defect model which dictates that removal of interstitial oxygen is the primary source of free electrons in ITO. The removal of interstitial oxygen may promote lattice expansion as the shielding which they provide against electrostatic repulsion of incorporated $Sn^{\bullet}$ dopants is removed.

In order to provide further verification for the relationship between free electron variation and lattice parameter change, this sample was then heated in an oxidizing atmosphere as a means to forcibly incorporate interstitial oxygen. Precisely 3ml of the dilute ITO solution was slowly heated up to 150 ˚C in a drying oven under an air atmosphere. After the original dispersing solvent was evaporated, exactly 3ml of hexane was added to the sample vial and gently shaken until the ITO was once again, re-dispersed in solution. An immediate difference in body color was observed as the solution had changed from blue to green. Transmission spectra were recorded and high resolution x-ray diffraction analysis was performed within an hour to determine any lattice parameter change. The results of these measurements are presented in Figure 5.10. The observed color change was due to a band gap contraction of ~0.2eV which is consistent with a loss of free electrons from the ITO conduction band. High-resolution x-ray diffraction indicated that although the particle size was unchanged, its lattice parameter had contracted by ~0.005Å. This analysis indicates that band structure and interstitial oxygen content may be correlated to the internal lattice structure of colloidal ITO and thus, offers additional support to the Frank and Kostlin defect model.

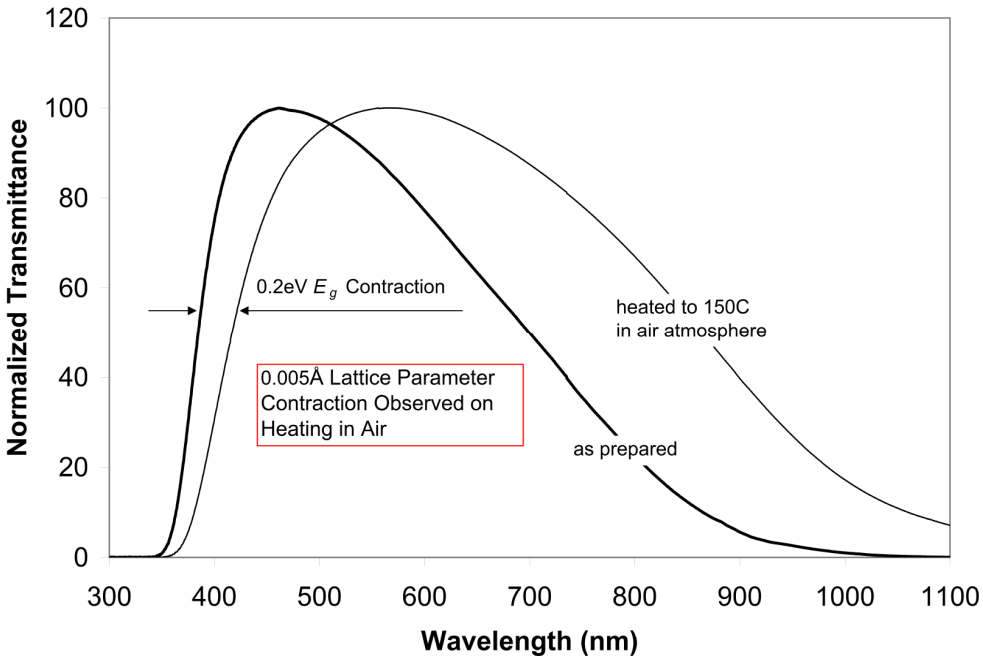

Figure 5.10: Normalized transmission spectra of a colloidal ITO sample containing ~9% Sn doping both before, and after heating in an air atmosphere. The spectral shift displayed is indicative of the removal of excess electrons from the conduction band structure. The lattice parameter is found to contract as a result of this treatment.

5.5 Composition-Structure-Property Relations

The variation in free electron concentration with ITO sputter target composition most often reported for thin films is as previously displayed in Figure 2.1. This well documented relationship is in fact, the principal reason that ITO sputter targets with 10% Sn are typically utilized by thin-film manufacturers. As discussed in the background section, this behavior is entirely consistent with the Frank and Kostlin defect model for ITO which asserts that Sn doping beyond an optimum level will result in an increasing prevalence of nearest neighbor $Sn^{\bullet} - O_i^{''}$ pairs which tend to trap interstitial oxygen and decrease free electron concentration.[1, 138] It was desired to know how this relationship of Sn content versus excess conduction band electron concentration is manifest in the

colloidal ITO nanoparticle system developed for this dissertation. Synthesis process parameters such as carboxylic acid to amine ratio, reaction temperature, and reaction time were held constant while the concentration of Sn used in solution was varied from 0 to 20% (by molar weight of cation). Table 5.1 displays this variation with the results of ICP-MS (composition) and x-ray diffraction (phase, particle size, lattice parameter) analyses. As was done for the material discussed in chapter four, a combination of ICP and x-ray analysis was utilized to verify that ITO had been formed in all reactions. In each case, a pure bixbyite phase is indicated with no measureable traces of SnO or SnO_2 impurities even at a measured doping content of ~18% Sn as shown in Figure 5.11. The doping efficiency was greater than 90% across the composition range produced.

Table 5.1: Composition and structural properties of colloidal ITO prepared with different initial Sn concentrations. All other process parameters have been held constant.

Sn (%) Used	Sn (%) ICP	Doping Eff. (%)	Phase ID	SnO or SnO_2	Particle Diamter (nm)	Lattice Parameter (Å)
0	0	n/a	In_2O_3	none	9.5	10.1225
2	1.97	98.51	In_2O_3	none	8.5	10.1282
4	3.93	98.36	In_2O_3	none	7.6	10.1301
6	5.64	93.97	In_2O_3	none	6.8	10.1327
8	7.42	92.70	In_2O_3	none	6	10.1351
10	9.34	93.43	In_2O_3	none	5.4	10.1369
12	10.93	91.08	In_2O_3	none	4.9	10.1381
14	12.60	90.03	In_2O_3	none	4.5	10.1392
16	14.41	90.05	In_2O_3	none	4.2	10.1399
18	16.24	90.21	In_2O_3	none	4.1	10.1414
20	18.03	90.17	In_2O_3	none	4.1	10.1419

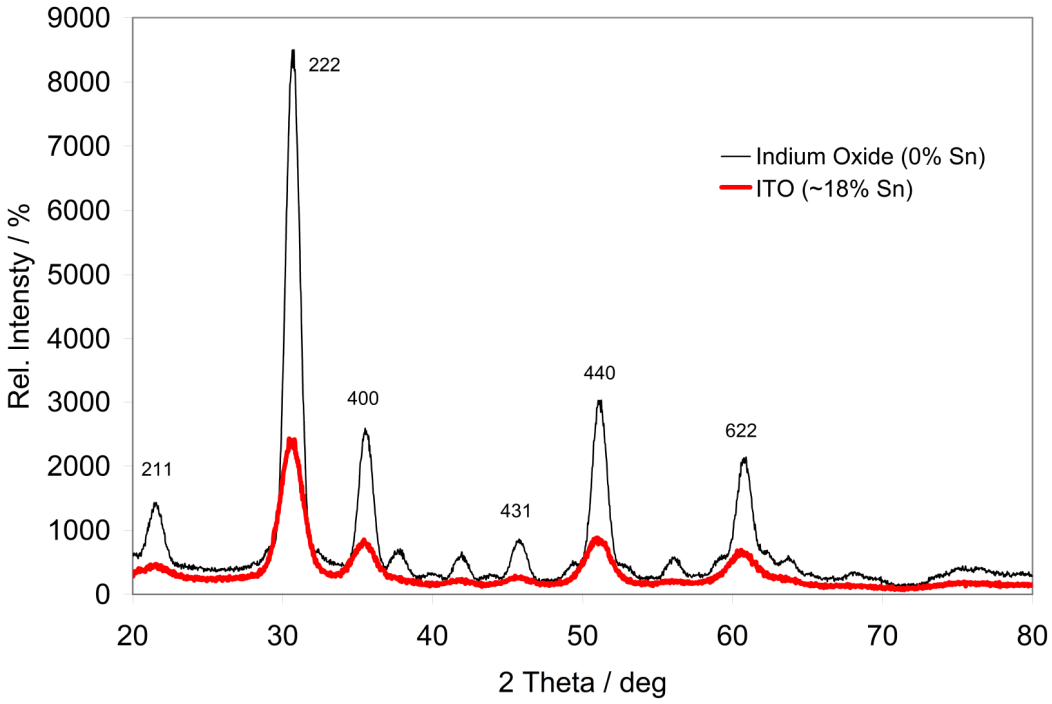

Figure 5.11: X-ray spectra comparing the phase purity of undoped colloidal In_2O_3 and colloidal ITO that incorporates greater than 18% Sn (as determined by ICP-MS analysis). The presence of primary diffraction peaks for SnO and SnO_2 are absent from the spectra.

It was immediately apparent by a progressive broadening of x-ray diffraction peaks (Figure 5.12), that the particle size was being reduced as the concentration of Sn increased in the lattice. Pseudo-Voigt peak-fitting routines and Scherrer equation calculations were performed using JADE software to attain values of the average particle diameter for each sample. These results are displayed in Table 5.1 and presented with respect to the incorporated Sn concentration in Figure 5.13 below. A decreasing particle size with increasing Sn content has previously been reported for solvothermally synthesized ITO nanoparticles.[48] An attempt is made here to offer a reasonable explanation for the observed trend in the case of colloidal ITO developed for the present dissertation work.

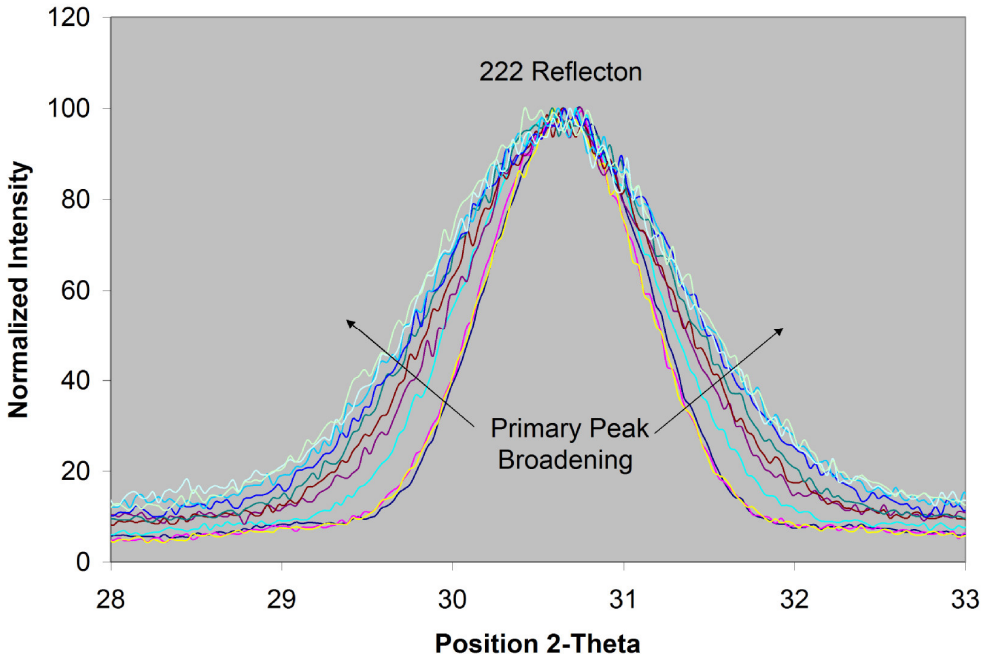

Figure 5.12: High-resolution x-ray diffraction spectra of the 222 reflection for colloidal ITO nanoparticle dispersions prepared with an increasing concentration of Sn precursor. The progressive peak broadening is indicative of a decrease in average particle size.

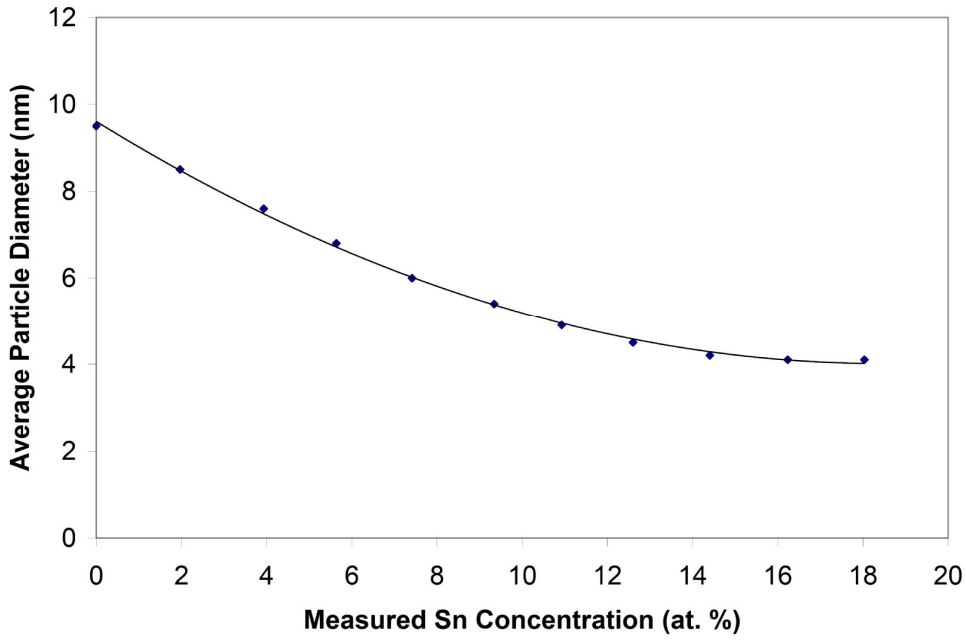

Figure 5.13: Variation of average particle diameter with incorporated Sn content for different dispersions of colloidal ITO. The trend line shown is of a simple second order polynomial character.

5.5.1 Composition-Structure Relations

Figure 5.14 presents TEM micrographs of samples doped with 0,2,4,6,8, and 10% Sn. It is immediately seen that much of the initial size decrease in moving from (~9.5nm at 0% Sn) to (~7nm at 5.6% Sn) was due to the increasing appearance of 6nm particles as more Sn precursor is added to the reaction solution. This initial size inhomogeneity is likely indicative of an analogous variation in Sn concentration. The smaller particles may be heavily doped (much greater than the average value determined by ICP) while the largest particles are poorly or perhaps, entirely undoped. In general, an ensemble of doped nanoparticles will exhibit a range of dopant population per particle thus, leading to inhomogeneity in effective concentration.[4] Dopant distributions among nanoparticles can be described theoretically using the binomial expressions given in Equations 5.7 and 5.8. Rather than signifying carrier concentration, the parameter n is now the total number of dopant ions per particle having N total cation sites available for substitution and x is the dopant mole fraction. For $n << N$, $P(n|N)$ simplifies to $P(n)$ as the Poisson distribution.

$$P(n \mid N) = \frac{(N)!}{n!(N-n)!}(xN)^n(1-(xN))^{N-n} \qquad \text{Equation 5.7}$$

$$P(n) = \frac{(xN)^n e^{-xN}}{n!} \qquad \text{Equation 5.8}$$

These expressions indicate that large variations in the doping levels of individual nanoparticles can arise from relatively ideal statistical dopant distributions within an ensemble of particles.

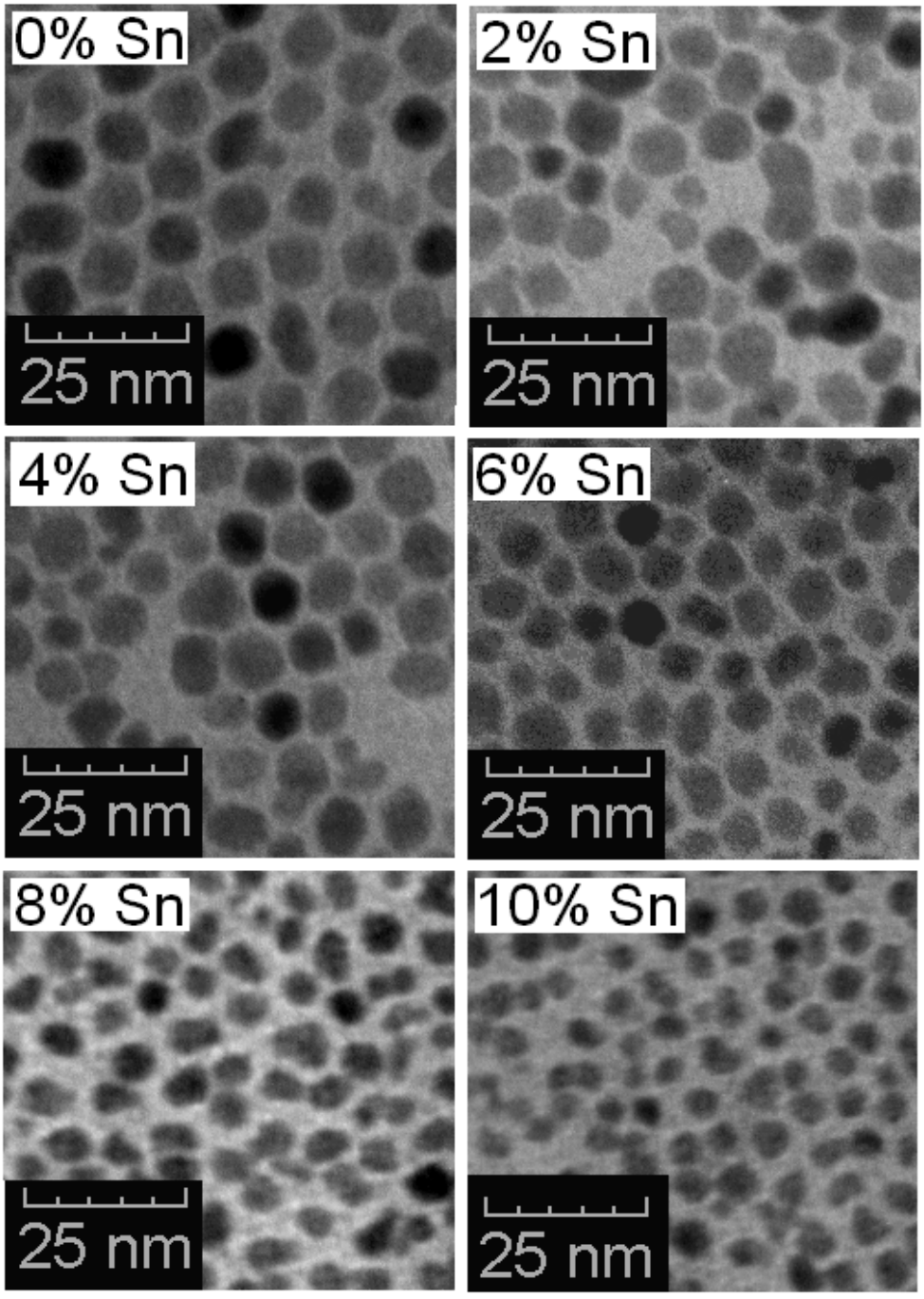

Figure 5.14: TEM images of a series of colloidal ITO dispersions prepared with the indicated Sn doping contents. The appearance of smaller particles on 2 and 4% Sn doping produces the rapid decrease in average particle size measured by x-ray diffraction. Those made with 8% and greater Sn contents display relatively narrow size distributions.

While the Poisson model can provide insight on dopant populations within an arbitrary system of particles, it does not explain why a doped colloidal ITO particle would be so much smaller than an undoped version. The diameters of samples incorporating 6-18% Sn progressively shift towards 4nm while showing no significant degree of size inhomogeneity. This trend may be understood by considering the kinetics of nucleation and growth processes for a nanoparticle system attempting to incorporate dissimilar atoms into its lattice. As discussed in section 5.2, it is estimated that the majority of particle nucleation is complete within a few seconds of reaction initiation and that core nuclei may be composed almost exclusively of the pure In_2O_3 lattice. What follows this event is primarily diffusive adsorption of both indium and tin precursors onto the growing nanoparticle surfaces. It is well known and verified by the present work, that the lattice structure of ITO is inherently distorted relative to undoped In_20_3. This may produce a thermodynamic barrier which inhibits further In_2O_3 growth around a Sn-doped particle, or equivalently, yields a greater solubility of ITO than undoped In_2O_3.[36] This effect can be represented in an analytical way by the Gibbs-Thompson relation,

$$S_r = S_B \exp\left[\frac{2\gamma V_m}{rRT}\right] \qquad \text{Equation 5.9}$$

where, S_r is the solubility of a nanoparticle of radius r, S_B is the solubility of the corresponding bulk material, V_m is the molar volume, and γ is again, the specific surface energy of the nanocrystal as in Equation 4.1. Surface or near-surface dopants may cause lattice strain that elevates the specific surface energy, γ, which would then increase the doped nanoparticle's solubility and inherent stability at the reduced dimensions observed.

Figure 5.15 presents the variation in average lattice parameter as the Sn content is increased. Also shown is the calculated number of Sn atoms per average particle over the same range. While the range from 0-4% Sn is heavily influenced by size and doping inhomogeneity, the 6-20% range offers some useful insight. The number of Sn atoms per particle is decreasing in part, because the efficiency of doping is being reduced from (94% at 6% Sn) to (90% at 14% Sn). Another reason may be that the number of particles incorporating Sn dopants is rapidly increasing. As these Sn atoms are confined to a progressively smaller volume, they are subsequently forced closer together. As a result, the lattice parameter of the material is progressively expanded due to the electrostatic repulsive force discussed in section 5.4. The number of Sn atoms per particle begins to rise from 14% to 18% doping because both particle size and doping efficiency have reached steady states. Thus, any additional Sn is forced into the ~4nm particle volume as confirmed by x-ray diffraction which indicates dopant atoms are fully incorporated within the bixbyite lattice. It is interesting to note that the lattice parameter appears to increase at a slower rate for these data points. This may be further indication of interstitial oxygen trapping by Sn as proposed by the Frank and Kostlin defect model. In this case, the increased electrostatic repulsion of additional Sn dopants may be partially screened by an increased number of interstitial oxygen ions.

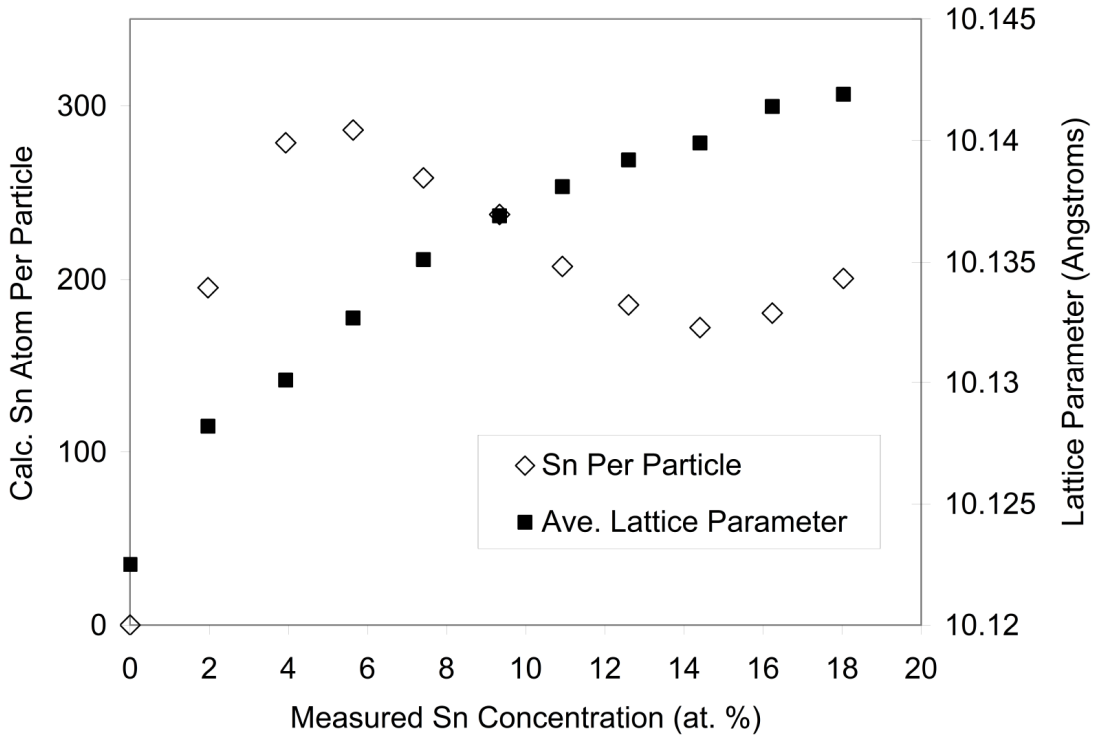

Figure 5.15: Variation of both average Sn atoms per particle and lattice parameter with a variation in the average Sn concentration as determined by ICP-MS analysis. While the data points corresponding to Sn concentrations up to 6% are heavily influenced by size and concentration inhomogeneity, those points from 8 to 20% offer useful insight. While fewer Sn atoms are found within each ITO nanoparticle, the reduced particle volume forces these dopants closer together. This may increase the electrostatic repulsive force between them and create the observed lattice parameter expansion.

5.5.2 Composition-Property Relations

The influence of Sn concentration and particle size on the optical properties of this system, were evaluated by the approaches outlined in section 5.3 of this chapter. The degree of band gap expansion for each sample (0 to 18% Sn) was determined and is presented in Figure 5.16. This analysis was performed at least 3 weeks following reaction initiation such that the generation of excess conduction band electrons could be assumed complete within each sample. Again, the two limiting cases were investigated (no quantum confinement and classic quantum confinement theory).

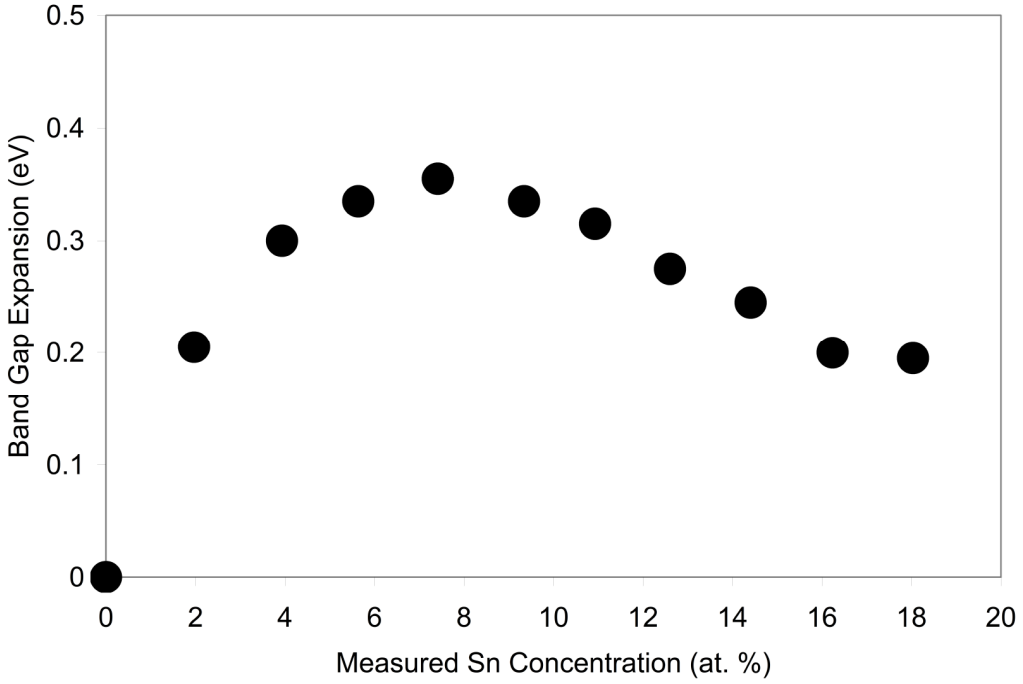

Figure 5.16: Variation in the measured band gap expansion of colloidal ITO as the Sn content is increased within the nanoparticle lattice. Expansion values displayed are relative to an undoped colloidal In_2O_3 nanoparticle system.

The ***free*** electron concentration for each sample was calculated using the bulk-like dispersion previously derived and presented in Equation 5.6. The variation of these values with incorporated Sn content is displayed in Figure 5.17 below. The trend observed for colloidal ITO is similar to those reported for sputter-coated thin film versions of the material.[3, 102] The peak in estimated free electron concentration of $1.84\times10^{20}\,cm^{-1}$ (~20 free electrons per particle) occurs at an incorporated Sn content of ~7.4% as determined by ICP-MS analysis. This optimum dopant concentration is slightly less than the majority of values reported for thin film ITO. Just as in the case of thin films, Sn atoms incorporated into a colloidal ITO particle are forced progressively closer together as their concentration in the lattice is increased. The Frank and Kostlin defect model dictates that this will increase the occurrence of nearest-neighbor $Sn^{\bullet}-O_i^{''}$ associates which then results in the increased trapping of interstitial oxygen and a decrease in free electron concentration.[54, 138] In the present case of colloidal ITO however, dopant-induced particle size reduction may exacerbate this behavior. As previously shown in Figure 5.15, a progressive increase in lattice parameter was observed as the Sn content was increased, even though the average number of Sn atoms per particle had decreased. This indicated that Sn dopants were being forced closer together within the nanoparticle boundaries. This behavior may increase the incidence of nearest-neighbor $Sn^{\bullet}-O_i^{''}$ associates and lead to trapping of interstitial oxygen at a lower Sn concentration than that observed in the thin-film (bulk) material form. The ability to produce a series of colloidal ITO dispersions in which the size is held constant while the Sn concentration is progressively increased would aid in the explanation of the observed quenching behavior.

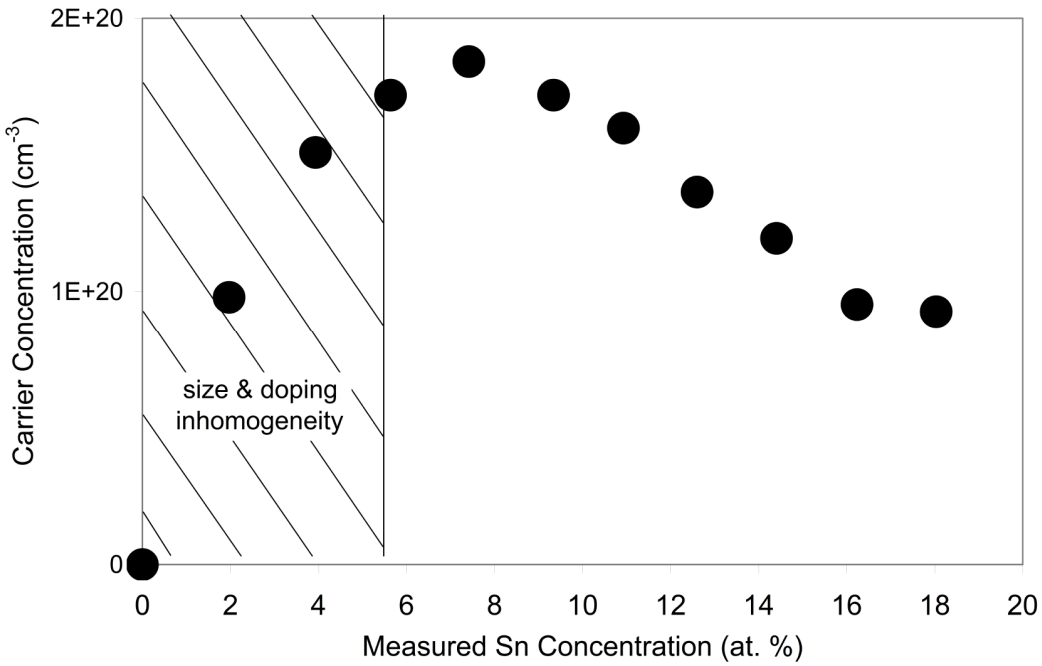

Figure 5.17: Variation in the estimated ***free*** electron concentration of colloidal ITO as the Sn content is increased within the nanoparticle lattice. Values displayed were calculated using Equation 5.6 with the assumption of bulk-like band dispersions for each colloidal system. Samples made with less than ~6% Sn display size and doping inhomogeneities.

Taking the average particle size into account, the above data indicates that approximately 20 excess free electrons are present per colloidal ITO particle when a Sn doping concentration of 7.4% is utilized. Estimation under the assumption of a quantum confinement influence requires the calculation of conduction band energy levels (1s, 1p, 1d, etc…) for each of the colloidal dispersions. This was again, done using the effective mass approximation and a radial spherical Bessel function as described in section 2.6.2 of the background chapter. The average particle size for each colloidal ITO dispersion was utilized as the input values. While those points corresponding to Sn concentrations less than 6% are significantly influenced by size and doping inhomogeneity, the remainder of this data can be considered reliable. As shown in Figure 5.18, the majority of expansion data points fall within the 1s to 1p conduction band energy levels with none moving

above the 1d level. When the size-distributions of each colloidal dispersion are taken into account for the calculation of energy level positions, the plot of Figure 5.19 is achieved. As discussed in section 5.3.2, an increased effective electron mass may extend the onset of quantum confinement to even smaller particle dimensions. This behavior coupled with a tendency of the EMA approach to overestimate the quantum confinement effect could indicate that the 1d state is occupied for data points up to ~14% Sn doping. Above this value however, a rapid size-induced rise in the 1d level coupled with a Sn-induced decrease in excess electron content may pin the systems to a 1p level state. Similar to the issue of temporal evolution of conduction band filling discussed in section 5.3.2, samples displaying a more monodisperse size-distribution and the inclusion of a Tight Binding model are necessary for a more definitive analysis of the quantum confinement effect in this system.

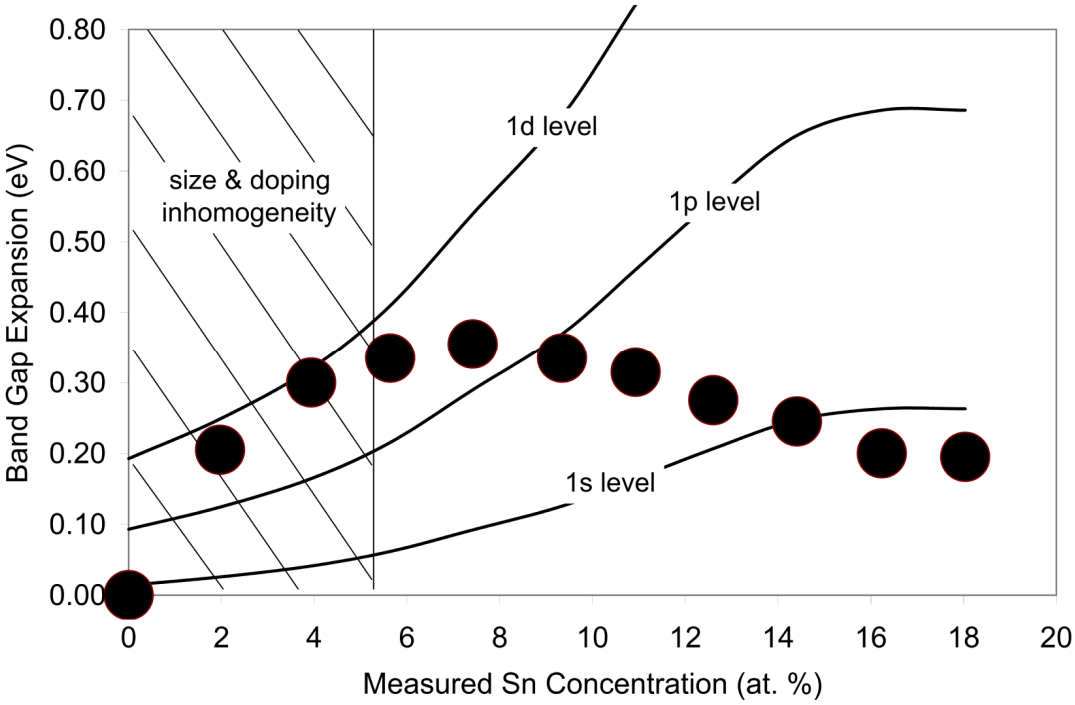

Figure 5.18: Variation in the measured band gap expansion of colloidal ITO as the Sn content is increased within the nanoparticle lattice. The location of conduction band energy states were calculated using the EMA and a radial spherical Bessel function. Energy level positions were determined for each of the eleven colloidal nanoparticle samples displayed using their average particle size as input values.

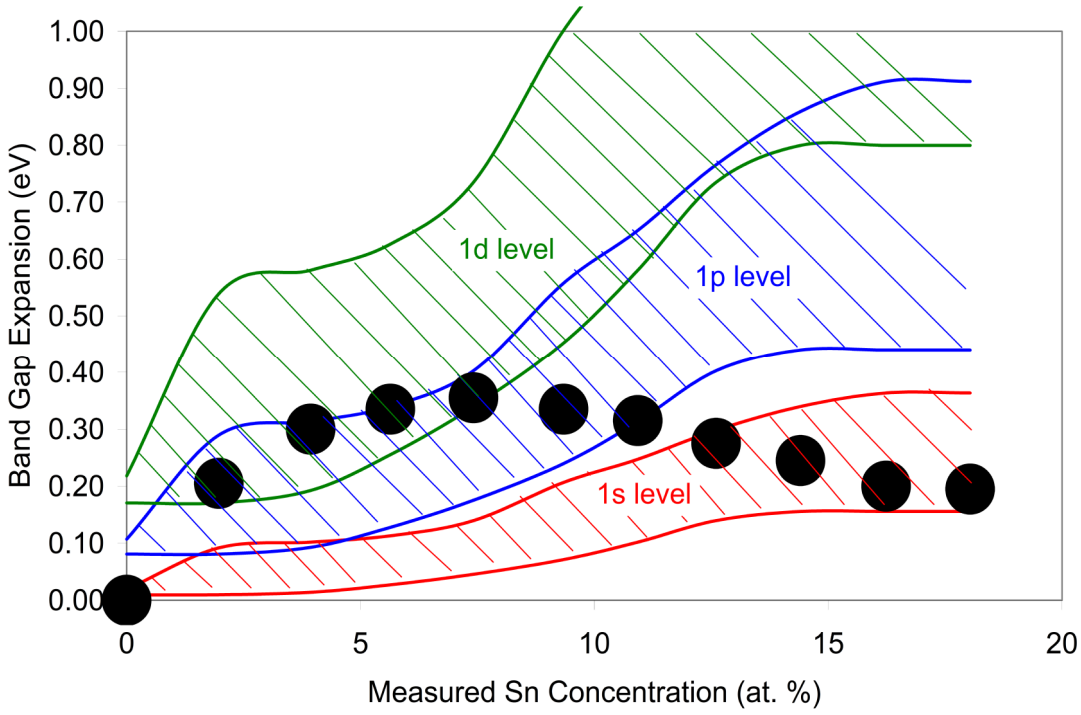

Figure 5.19: Variation in the measured band gap expansion of colloidal ITO as the Sn content is increased within the nanoparticle lattice. The location of conduction band energy states were calculated using the EMA and a radial spherical Bessel function. Energy level positions were determined for each of the eleven colloidal nanoparticle samples displayed using their particle size-distributions as input values. These distributions were determined for each sample by an analysis of TEM images.

A common method utilized to correlate electro-optical data taken from various thin-film studies is to plot their measured band gaps against the measured carrier concentrations to the 2/3 power (E_g *vs.* $n^{2/3}$ plot). This is done as a consequence of the $n^{2/3}$ influence inherent in the Burstein-Moss conduction band filling expression (Equation 2.41).[49, 67, 72] Figure 5.20 presents a plot of this type which utilizes data obtained for the Sn concentration series described above. The slope of this line is equal to the reduced effective mass ($0.22m_o$) and when extended to $n^{2/3} = 0$, an estimate for the band gap of undoped In_2O_3 may be attained. The 3.48eV value indicated by this procedure is 0.07eV less than that directly measured for the undoped colloidal In_2O_3 sample. An EMA calculation for the ~9.5nm undoped colloidal In_2O_3 system can account for only 0.01eV of the expansion and as previously discussed, this effect may be overestimated as well. A reasonable explanation for the anomaly is that this "undoped" system is in fact, slightly degenerate in nature. It is well known that pure In_2O_3 maintains a low level of regular lattice, structural oxygen vacancies which yield modest degeneracy.[38] If the 1s level is occupied by two electrons per particle, valence to conduction band transitions will be forced into the 1p level. According to (typically over-estimating) EMA calculations, this would be located approximately ~0.09eV higher than in an analogous bulk material. Thus, it is certainly possible that a combination of quantum confinement and modest degeneracy is present in the undoped colloidal In_2O_3 nanoparticle system.

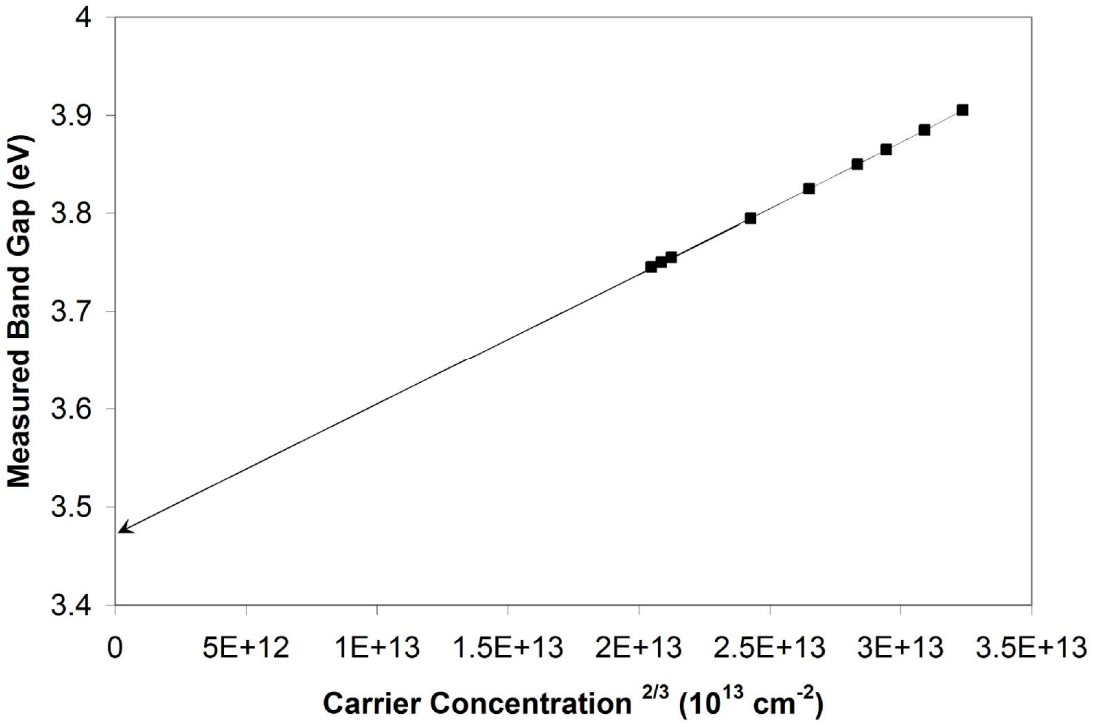

Figure 5.20: Correlation of experimentally measured band gaps of colloidal ITO dispersions with their estimated carrier concentrations to the two-thirds power ($n^{2/3}$). When extended to $n = 0$, this relationship provides the expected band gap of the undoped In_2O_3 lattice.

5.6 Summary

The intrinsic properties of single crystalline ITO particles produced in this dissertation work were investigated by monitoring the evolution of absorption edge progression and excess conduction band electron generation on time scales ranging from milliseconds to hours in length. The ability to perform this analysis is due to the inherent transparency of the colloidal nanoparticle form. In-situ spectroscopy was able to provide additional experimental support of models proposed by both Schwartz[36] and Erwin[30] for the compositional structure of doped nanoparticles formed in a solution of both host and dopant species. Continued monitoring of the colloidal dispersion's optical properties provided a means to map the effects of conduction band filling and energy level occupation by methods which are novel for an ITO nanoparticle system. Through this analysis, it was found that the quantum confinement effect may allow significantly fewer excess conduction band electrons to expand the band gap of a colloidal ITO nanoparticle system. When the rate of band gap expansion was correlated with a progressive expansion in lattice parameter over the same period, experimental support for the Frank and Kostlin defect model for ITO was achieved. Finally, the basic relationships between composition, structure, morphology, and functional properties were established by an analysis of Sn concentration variation.

CHAPTER 6

BATCH-SCALE PROCESSING OF COLLOIDAL ITO

6.1 Introduction

A key to the adoption of any material system for wide-spread industrial use is the development of synthesis routes capable of producing multi-gram or even kilogram quantities in a manner that is both rapid and cost-effective. An additional requirement which is becoming increasingly common is that the process inflict a minimum of environmental impact in terms of materials used and waste produced. The colloidal ITO synthesis process developed in this dissertation work relies on common metal fatty-acid salts and relatively cheap hydrocarbon solvents. The procedure outlined in chapter four is also rapid, taking just 5-6 hours from initial precursor weighing to final product dispersal. As previously discussed, the concentration of precursors in solution must attain a critical level of supersaturation (C_{SS}) for nucleation and growth of colloidal ITO nanoparticles to occur.[4] Injection of primary amine precursors above the critical nucleation temperature T_c, achieves this saturation level but, becomes increasingly cumbersome to perform when large reaction volumes for the synthesis of multi-gram quantities are required. Furthermore, because the octadecylamine precursor used is a solid at room temperature, copious amounts of chloroform are required to dissolve any unreacted material when very large amounts (10s of grams) are utilized. In response, modifications to both the synthesis approach and choice of amine precursor were made such that multi-gram quantities of high-quality colloidal ITO nanoparticles could be made in a manner suitable for industrial adoption. As will be shown, the primary trade-

off for the benefit of this large volume reaction is a broadening of the particle size-distribution.

6.2 Non-Injection Synthesis Route to Colloidal ITO

The approach taken was to combine all reactants together (metal carboxylates and amine) in a 1000ml flask at room temperature such that supersaturation conditions were already achieved. Slow heating of this solution to a point just above the critical nucleation temperature, T_c, allowed for nucleation and growth of colloidal nanoparticles as shown in Figure 6.1. This kinetic model assumes that the solution temperature has just moved above T_c and is subsequently held at that point (or slightly higher) throughout the time period displayed.

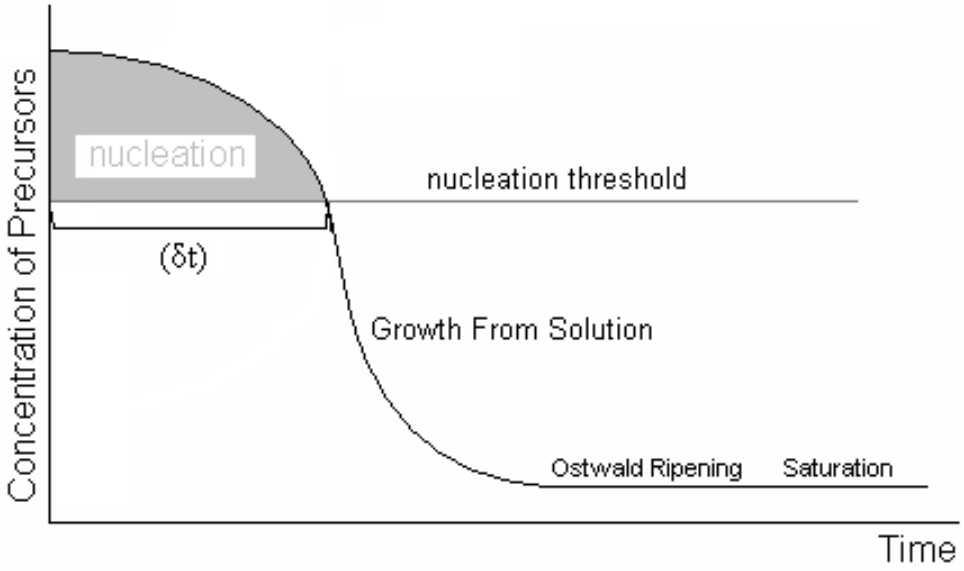

Figure 6.1: Kinetic model of nucleation and growth for a non-injection approach to colloidal nanoparticle synthesis. It is assumed that the solution temperature has just reached T_c at time *t=0,* where it is held for the duration of the modeled period.

Once nucleation of embryos has commenced, the concentration of precursors will progressively decrease to a point below that required for homogeneous nucleation. Unlike the case of rapid amine injection, no temperature drop is performed in the above method. This leads to a longer nucleation period $\delta(t)$ and an associated broadening of the particle size-distribution.[101] While the nuclei formed at time t_1 are growing, additional nuclei at times t_2, t_3, t_n are being formed which leads to a range of final particle sizes when the precursor concentration falls below C_{SS}.[101, 110, 139] While growth from solution will tend to occur most rapidly on those particles with the highest surface energy (i.e., the smallest particles), the final size distribution will typically be larger than that found in the rapid injection technique previously described.[101] Whereas octadecylamine was used in the rapid injection method, oleylamine was used for the current non-injection technique. While both compounds are C18 amines, oleylamine is more "user friendly" because it is a liquid at room temperature and thus, does not require heating prior to injection.

6.3 Specific Procedures and Reaction Analysis

Materials: Indium acetate (99.99%), tin acetate (99.99%), myristic acid, oleylamine, and 1-octadecene were obtained from Sigma-Aldrich. Chloroform, n-hexane, and acetone were obtained from VWR Scientific. All chemicals were used as-received.

Synthesis: $In(Ac)_3$ (27 mmol), $Sn(Ac)_2$ (3 mmol), myristic acid (MA) (90 mmol), and oleylamine (OA) (90 mmol) were combined with 400 ml of octadecene (ODE) in a 3-neck flask of 1000ml capacity. The flask was then attached to a standard Schlenk line assembly, purged with argon several times, and degassed under vacuum at 110 °C for two hours. The entire solution was then raised to 250 ˚C at a rate of 5 ˚C per min, under

high purity argon flow. The solution became faint yellow as the temperature rose past ~220 ˚C which indicated that particle nucleation had commenced and the critical temperature T_c for the onset of homogeneous nucleation was likely found in the 200-220 ˚C range for the specific precursor ratios used in this sample. The solution color shifted very rapidly to dark green as the temperature moved above 230 ˚C and appeared almost black at its target point of 250 ˚C due to the high concentration of ITO particles in solution. FT-IR analysis of an aliquot taken from this solution at 250 ˚C presents a very different reaction progression than that seen when octadecylamine was used as the primary nucleophile (Figure 6.2). Only a very weak signal from free carboxylic acid at 1710cm^{-1} remains and the appearance of the asymmetric stretching mode of an amide peak near 1690cm-1 is now very evident.[124] The prominent peaks at ~1630cm^{-1} and ~1537cm^{-1} are assigned to scissoring and bending modes of N-H and the characteristic double carbon bond of the oleylamine compound, respectively.[126]

Although 30 times more material was made by this non-injection approach, the use of 1 oleylamine instead of octadecylamine made the purification process considerably easier. A significant amount of the amine precursor is often present in solution following synthesis and, in the case of octadecylamine, will begin to solidify as the reaction is reduced to room temperature for product collection. Its complete removal then requires the use of a large volume of chloroform and repeated centrifugation. As oleylamine is a liquid at room temperature, this collection process required only one centrifugation step with a minimum of chloroform stabilization. Following washing with acetone to remove any side products, approximately 8 grams of high quality colloidal ITO nanoparticles were re-dispersed in hexane. The entire process took only five hours.

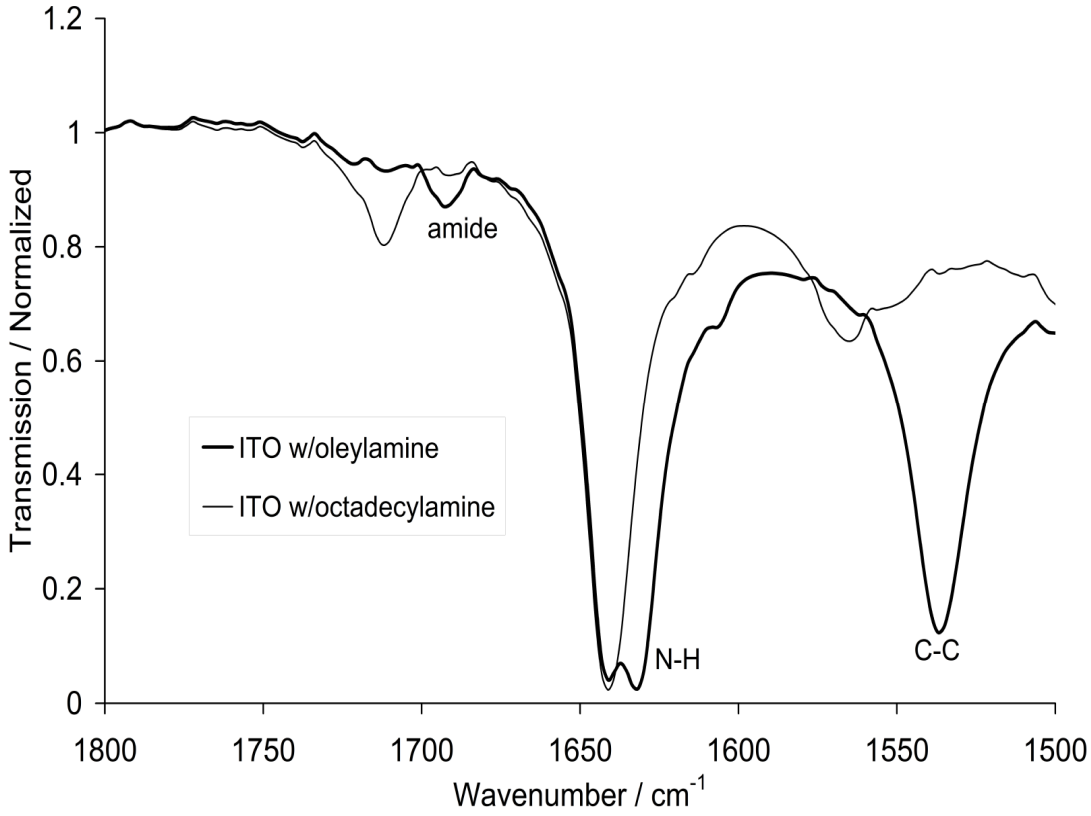

Figure 6.2: FT-IR analysis comparing the use of different amines for colloidal ITO synthesis. The spectra corresponding to octadecylamine was taken an hour after its injection and the one corresponding to oleylamine was taken once the reaction temperature had reached 250 °C .

6.4 Basic Properties of the Batch-Scale System

A combination of ICP and x-ray analysis revealed the ITO system was of the pure bixbyite structure with a tin concentration of 9.45% (Figure 6.3). Application of the Scherrer equation to the 222 reflection indicates an average particle diameter of 6.5nm which is almost 20% larger than the system made by the rapid injection technique with octadecylamine. This may be a factor of the more bulky R-groups and their double-bond formations which are inherent to oleylamine. Recall that the very bulky tertiary amine used in previous work on In_2O_3 produced particle sizes well over 20nm in diameter. The TEM image in Figure 6.4 also shows that the size distribution of the colloidal ITO made by non-injection is significantly broadened and was entirely expected from an extended nucleation event.[101, 110]

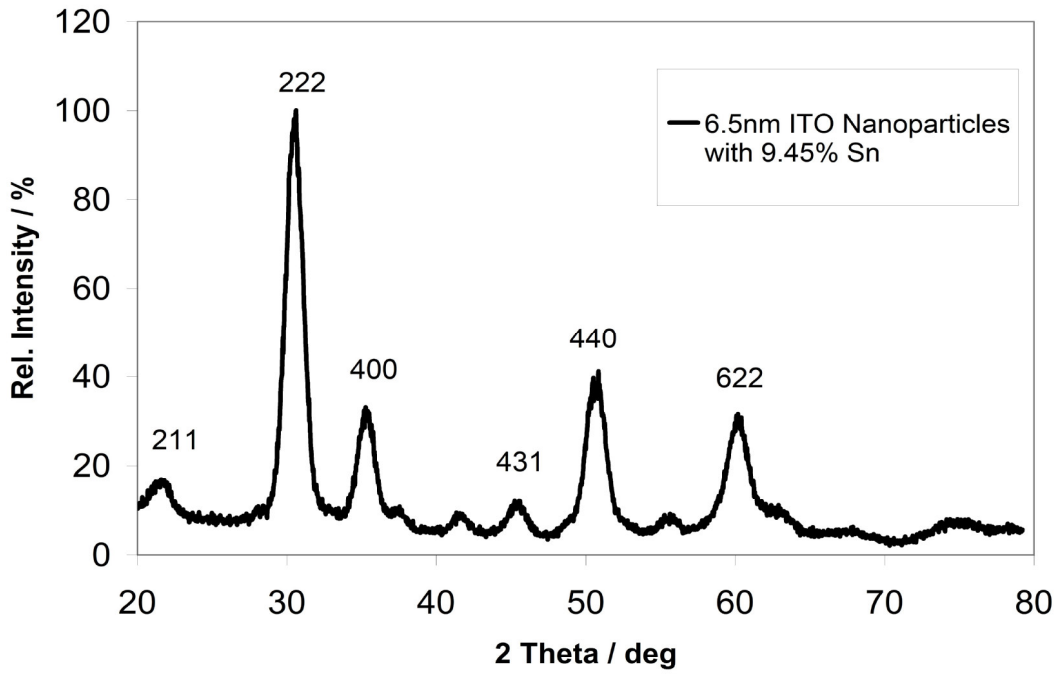

Figure 6.3: X-ray diffraction spectra of the colloidal ITO produced by the non-injection technique. Peak positions are well correlated to the pure In_2O_3 bixbyite phase.

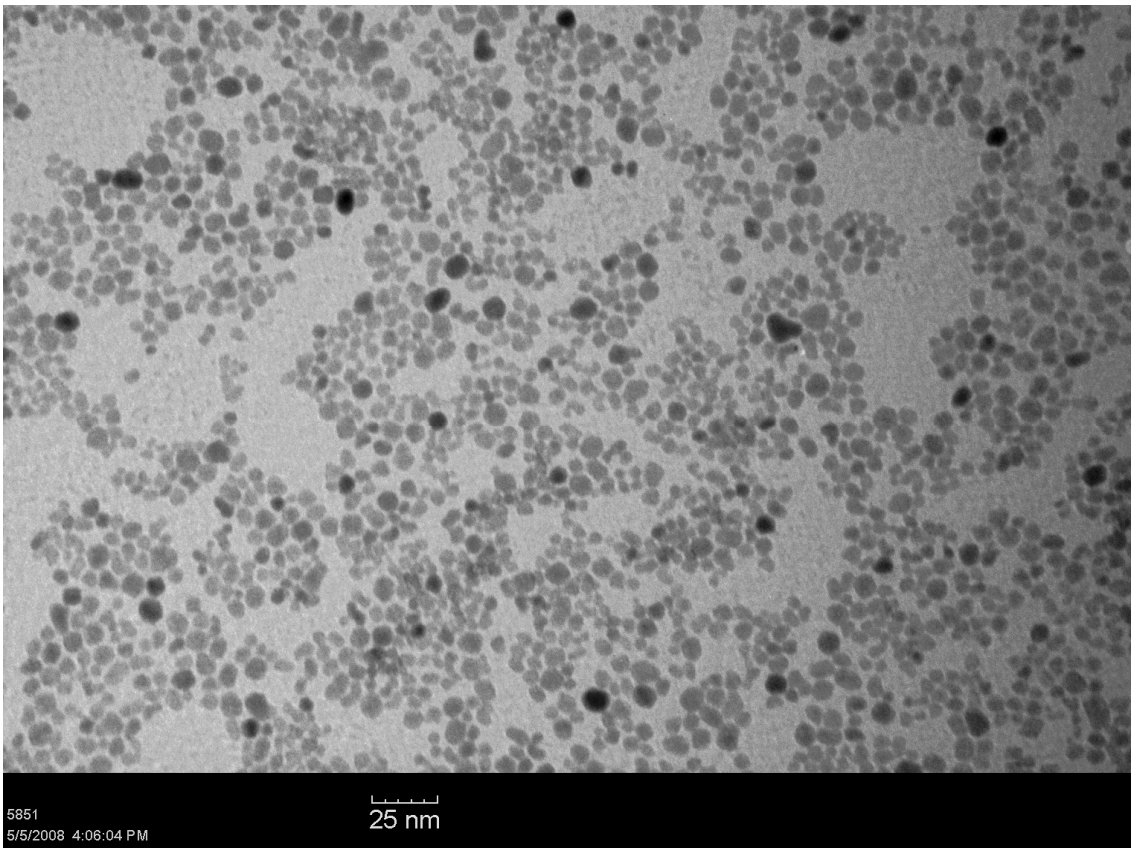

Figure 6.4: TEM image (290X) of the colloidal ITO produced by non-injection synthesis. The system displays a much wider size-distribution than that found in an analogous dispersion made using a rapid injection approach.

6.5 Electrical Analysis of Pressed Pellets

An additional way to verify the synthesis of ITO with high free electron concentration is through an analysis of the material's conductive ability. A well-established method to achieve this in conductive nanopowders is to perform Four-Point-Probe analysis on disk-shaped pressed pellets of the material.[140] In this way, shape factors can be utilized to remove any ambiguity associated with slight variations between pellets prepared for analysis. The resistivity (p) of a semi-infinite wafer with equal probe spacing is given by:

$$p = 2\pi s \frac{V}{I} \qquad \text{Equation 6.1}$$

where, s is the distance between probe tips, V is the applied voltage, and I is the current. As samples are not infinite in extent, correction factors must be multiplied by the right hand side of this equation.[141] There is extensive literature on the evaluation of geometric correction factors treating different specimen geometries in combination with different probe arrangements. The current work makes use of the methodology developed by Kelekanjeri et. al. in which, a closed-form analytical expression was obtained for the potential difference between the voltage probes.[141]

Good conductivity within a pellet requires that particles are in intimate contact. The boundary layer between adjacent particles will act as a source of resistance and therefore, sintering of the pellet to minimize the influence of these grain boundaries is needed.[140] Organic ligands that suppress the agglomeration of colloidal ITO in solution will prevent this close particle contact and must therefore, be removed. This requires heating the material in an atmosphere that contains oxygen so that CO_2 gas is formed as the organic

structures break down. Following evaporation of the dispersing solvent at 80 ˚C, the colloidal nanoparticles were heated in either air or a pure oxygen environment at 400 ˚C for three hours. Both air and pure oxygen atmospheres were utilized for this step in order to study their effects on final pellet conductivity. Recall that the Frank and Kostlin model of free electron generation in ITO relies on the removal of interstitial oxygen under a reducing atmosphere.[52, 54] Heating of the ITO particles to burn off organics in the presence of oxygen will naturally reverse this reduction process and decrease the free electron concentration. This was previously shown to happen in the colloidal ITO system at a temperature of only 150 °C (Figure 5.10). The resultant fine powder is composed of loosely agglomerated nanoparticles and EXTREME caution must be exercised when handling such a material. Inhalation and/or absorption through the skin are potential avenues to a dangerous exposure.[142] Precisely 120mg of material was formed into a 10mm diameter pellet using a Specac hydraulic press (5.5 tons of force for 30 seconds). Three pellets of each type material (heated in air or oxygen) were prepared and annealed at 700 ˚C for five hours in a highly reducing nitrogen-hydrogen atmosphere to once again, remove interstitial oxygen and promote free electron generation. Note that if organic ligands were not burned off prior to annealing in this reducing environment, amorphous carbon would form throughout the pellet volume. While this would certainly aid in conductivity (carbon is highly conductive), the value measured would not be an accurate estimate of the ITO material's intrinsic character.[143]

Four-Point probe analysis indicated that ligand removal in pure oxygen has a deleterious effect on pellet conductivity as compared to the samples prepared using an ambient air atmosphere. Samples made with powder prepared in oxygen displayed a

conductivity of 23 ±2 S/cm while those made with powder prepared in air indicated a conductivity of 28 ±3 S/cm. High conductivity in sputter-coated ITO thin-films has historically relied heavily on deposition atmosphere and therefore, the present results were not unexpected.[57] In the present case, it is theorized that the use of pure oxygen gas effectively locked in a higher concentration of interstitial oxygen. Band gap expansion analysis of the type described in chapter five (assuming a bulk-like dispersion), indicated that the colloidal ITO particles had an average free electron concentration of $1.81\times10^{20}\,cm^{-1}$ prior to being formed into a pellet. This estimate is within the range of values reported for sputter-coated thin film ITO samples that displayed conductivities on the order of 1,000 S/cm.[38] The cause of such a comparatively low conductivity in the present case of pressed pellets made from this material can be identified by close inspection of their surfaces. Figure 6.5 presents SEM micrographs of a representative sample following the 700 ˚C anneal. As seen in the upper image (higher magnification), the size of individual ITO particles has now increased from ~5nm (as prepared in solution) to approximately 30nm following the high temperature procedures. Sintering of particles is also evident and is the primary aspect that provides for a conductive pathway throughout the pellet volume and along its surface. However, the lower magnification image (bottom) clearly displays the widespread occurrence of large void spaces which will naturally break up this conductive pathway. This highlights the need for subsequent work on the development of suitable deposition procedures for this colloidal form of ITO.

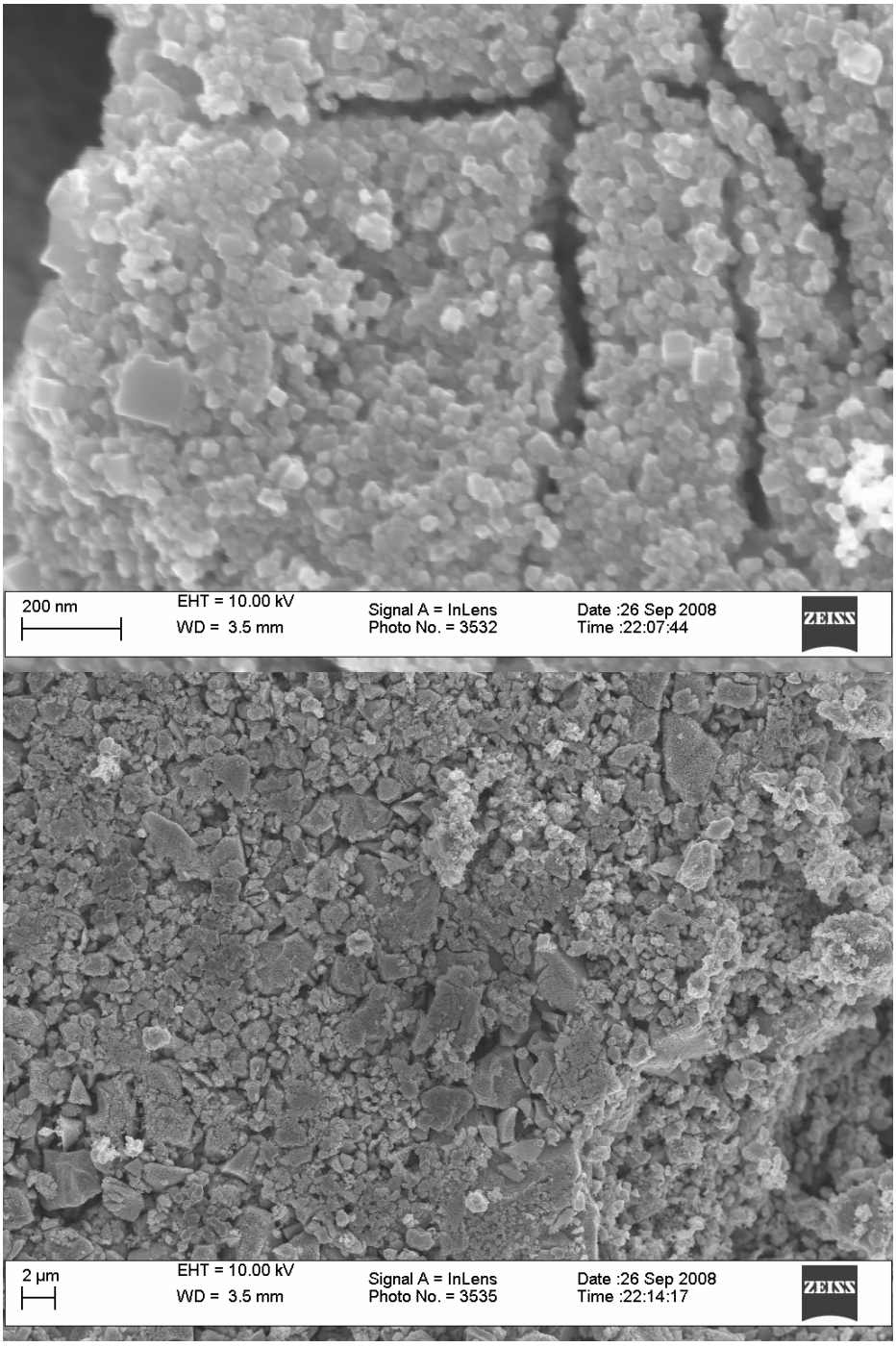

Figure 6.5: Higher (top) and lower (bottom) magnification SEM images of the surface of a 10mm pressed pellet made with ITO nanoparticles. The significant occurrence of void spaces will naturally interrupt the conductive pathway and increase sheet resistance.

Figure 6.6 displays an image of a 400nm cube-shaped ITO particle discovered on the surface of a pressed pellet. The inset image in this figure is a JCrystal rendering of an ideal bixbyite structure oriented in approximately the same position. The apparent perfection of the 400nm particle may be indicative of the single crystalline seed material from which it was formed. Close inspection of individual ~30nm particles around this larger version indicate that the cube-like bixbyite structure is repeatedly found.

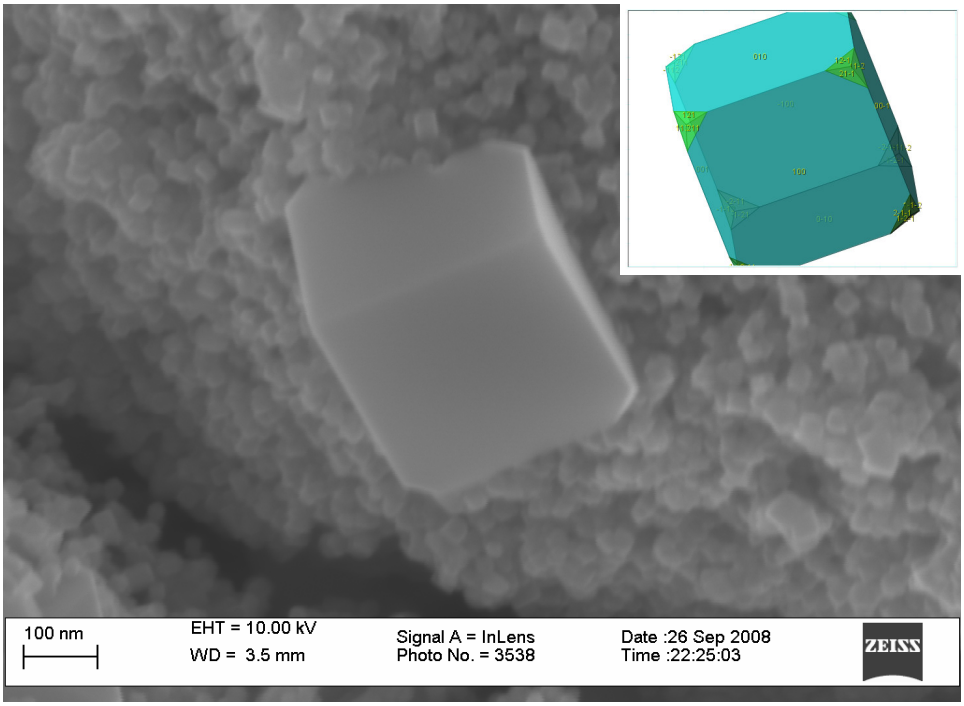

Figure 6.6: SEM image of a ~400nm ITO particle along the surface of a pressed pellet. Inset image displays a JCrystal rendering of the bixbyite structure in a similar orientation.

6.6 Summary

A simple and rapid technique was developed for the synthesis of multi-gram quantities of colloidal ITO. This was accomplished by a modification of the basic approach outlined in chapter four and relies on the slow heating of a super-saturated solvent solution of metal carboxylates and primary amines. A slight broadening of the particle size distribution was observed but, is considered acceptable in light of the thirty-fold increase in material produced. In theory, this process would be capable of producing kilogram quantities of high-quality, solution-dispersible, single crystalline, colloidal ITO nanoparticles in a manner suitable for industry adoption. Electrical characterization of disk-shaped, sintered pellets made from colloidal ITO provided final evidence of the material's degenerate nature. The low level of conductivity observed in these pellets highlights the need for additional work on the development of deposition procedures for the colloidal nanoparticle form of ITO.

CHAPTER 7

CONCLUSIONS

The principal objective of this research was to develop a colloidal nanoparticle form of Indium Tin Oxide, commonly referred to as ITO. This was motivated by a desire to expand the growing field of doped colloidal semiconductor nanoparticles into the relatively narrow materials class of Transparent Conductive Oxides (TCOs). Currently, there is an interest in solution-dispersible forms of nanocrystalline ITO for application to inkjet printing and dip-coating procedures.[45] In this respect, the present dissertation work has been an immediate success as the colloidal ITO system produced is among the most advanced of its kind yet reported. When dispersed in non-polar solvents (hexane, toluene, chloroform, etc…), the colloidal ITO system forms an optically clear solution with absolutely no incidence of agglomeration and can remain in this state at room temperature for months and potentially, years. Average particle diameters on the order of 5-6 nanometers with a narrow size distribution of ~15% are typically formed with individual particles displaying an essentially single crystalline character. Optical properties of the colloidal dispersion display the presence of a long wavelength IR reflection band and a blue-shift in the absorption edge position. Both of these features are characteristic of ITO with a high free electron concentration.[38, 67] This colloidal nanoparticle form was produced by a synthesis protocol which relies on readily available metal fatty-acid salts, primary amines, and a simple non-coordinating hydrocarbon solvent. FT-IR analysis of the reaction indicated that the entire process is driven by a series of intense nucleophilic substitution reactions (aminolysis, condensation, and

hydrolysis).[116, 122] Aminolysis is expected to be the primary ITO-generating reaction with additional material being produced by a secondary condensation/hydrolysis cascade reaction.

The optical clarity of the colloidal system developed in this work has allowed the fundamental materials physics of single crystalline ITO nanoparticles to be probed. In-situ spectroscopy during the first 30 seconds of system formation revealed that the onset of a long wavelength reflection edge associated with free electrons in the colloidal ITO lattice did not occur until core nuclei had developed and begun to grow. This could be indicative of a structure comprised of an undoped In_2O_3 core covered by an ITO shell and may be viewed as additional experimental evidence for the model of doped nanoparticle composition previously proposed by both Schwartz[36] and Erwin[30]. The subsequent slow generation of additional excess conduction band electrons over the next 120 hours could be observed by a progressive and measureable expansion of the material's intrinsic band gap. The number of excess conduction band electrons required to produce the observed band gap expansion were estimated assuming both bulk (free electron) and quantized (confined electron) models. Analyzing the system with a typical bulk-like parabolic conduction band dispersion indicated that approximately 14 free electrons per particle could produce the observed band gap expansion. In contrast, the assumption of a confined electron scenario predicted that the same effect could be accomplished with just 8 excess conduction band electrons per particle. It must be noted however, that the EMA model used for this quantized case is well known to over-estimate the quantum confinement effect and its associated degree of band gap expansion.[133] It also remains unclear what impact an increase in the effective electron mass would have on the degree

of conduction band energy level separation (i.e., 1s, 1p, 1d, etc…). The effective electron mass is well known to increase as the concentration of excess conduction band electrons are increased in a degenerate semiconductor.[43, 74-83] This could theoretically suppress the onset of quantum confinement until even smaller particle sizes are reached. A reduction in the particle size distribution coupled with analysis at much shorter time points than those utilized in the present work may provide an extremely detailed map of the conduction band structure in the colloidal ITO system.

Correlation of the measured band gap expansion to an increase in the measured lattice parameter of colloidal ITO over the same 120 hour period was able to provide experimental support for the Frank and Kostlin defect model of free electron generation.[1, 52, 54, 138] Both progressions achieved steady-state values at approximately 72 hours following reaction initiation. This expansive process could be reversed by heating the material to just 150 °C in an oxidizing atmosphere followed by re-dispersal in solution. The resultant contraction of both band gap and lattice parameter are consistent with a loss of excess conduction band electrons and an increase in interstitial oxygen content, respectively.[52] Establishment of additional fundamental relationships between composition, structure, and intrinsic functional properties were also achieved. A series of samples with a progressive increase in Sn-dopant concentration from 0 to ~18% (determined by ICP-MS analysis) was produced. As the incorporated Sn content increased, the average particle size of colloidal ITO was observed to decrease. This behavior was explained using the Gibbs-Thompson relation to correlate a variation in particle solubility with dopant-induced lattice strain.

A variation in the degree of band gap expansion over this range was then investigated with the intention of establishing the optimum system composition with respect to the maximum concentration of excess conduction band electrons achieved. The maximum degree of band gap expansion occurred at an incorporated Sn concentration of 7-8% which is in the lower range of optimum dopant concentrations reported for thin film forms of ITO.[3] Assuming a bulk-like conduction band dispersion character, the estimated free electron concentration achieved at this doping level was $1.84\times10^{20}\,cm^{-3}$ or ~20 electrons per particle. This value is within the range of those reported for sputter-coated thin film forms of ITO as well.[60, 63] When the measured band gaps of each colloidal ITO sample in the 0-18% Sn-dopant concentration range were plotted against their free electron concentrations to the two-thirds power ($n^{2/3}$ plot), a band gap determination for the pure, undoped end member (0% Sn) was achieved. This value was 0.07eV less than that observed in a direct experimental measurement of an undoped colloidal In_2O_3 sample made using the same synthesis procedure. A likely explanation for this difference is that the undoped material is slightly degenerate in nature. It is known that pure In_2O_3 is characterized by a low level of regular lattice oxygen vacancies that yield a moderate level of degeneracy.[38]

As previously discussed, the rapid injection synthesis technique is capable of forming systems with very narrow particle size distributions and this property is extremely important for studies of fundamental physics. However, this process becomes increasingly cumbersome to perform when large scale reaction volumes for the synthesis of multi-gram quantities are required. Accordingly, a non-injection technique was developed to produce multi-gram quantities of highly-quality, solution dispersible, single

crystals of colloidal ITO. A thirty-fold increase in material production was achieved with an acceptable increase in particle size-distribution. It is expected that this method can be scaled up to produce kilogram quantities of high-quality material as well. The low level of conductivity achieved in pressed pellets made from this material highlights the need for subsequent work on handling and deposition procedures for this colloidal nanoparticle form of ITO.

New synthesis routes to the formation of high quality doped colloidal semiconductor nanoparticles are appearing with increasing regularity in the scientific literature and this underscores the increasing level of interest in these systems.[4, 30, 35, 36, 144-146] Within the last year, a group in Korea has successfully synthesized ITO in the colloidal nanoparticle form.[147] Their process utilized the slow heating of a combination of metal carboxylates and chlorides with pure oleylamine as both capping agent and coordinating solvent. Accordingly, research and development of this new material form has already begun to expand. Colloidal ITO may one day find use in inkjet printing, dip-coating, and a variety of composite systems. Beyond these very practical applications, it is the wish of this author that the use of colloidal ITO to investigate the phenomenon of electron confinement in heavily degenerate semiconductors be expanded.

REFERENCES

1. Ingram, B. J.; Gonzalez, G. B.; Kammler, D. R.; Bertoni, M. I.; Mason, T. O., Chemical and structural factors governing transparent conductivity in oxides. *Journal of Electroceramics* **2004,** *13* (1/2/3), 167-175.

2. Schubert, E. F., *Physical Foundations of Solid-State Devices*. 2007.

3. Elfallal, I.; Pilkington, R. D.; Hill, A. E., Formulation of a statistical thermodynamic model for the electron concentration in heavily doped metal oxide semiconductors applied to the tin-doped indium oxide system. *Thin Solid Films* **1993,** *223* (2), 303-10.

4. Bryan, J. D.; Gamelin, D. R., Doped semiconductor nanocrystals: Synthesis, characterization, physical properties, and applications. *Prog. Inorg. Chem.* **2005,** *54*, 47-126.

5. Gilstrap, R. A., Jr.; Capozzi, C. J.; Carson, C. G.; Gerhardt, R. A.; Summers, C. J., Synthesis of a nonagglomerated indium tin oxide nanoparticle dispersion. *Adv. Mater. (Weinheim, Ger.)* **2008,** *20* (21), 4163-4166.

6. Roest, A. L. Electronic Properties of Assemblies of ZnO Quantum Dots. Universiteit Utrecht, 2003.

7. Faraday, M., Experimental Relations of Gold (and Other Metals) to Light. *Philosophical Transactions of the Royal Society, London* **1857,** *147*.

8. Edwards, P. P.; Thomas, J. M., Gold in a metallic divided state-from Faraday to present-day nanoscience. *Angew. Chem., Int. Ed.* **2007,** *46* (29), 5480-5486.

9. Swanson, J. N., Repeated Colloidal Gold Tests in Rheumatoid Arthritis. *Ann Rheum Dis* **1949,** *8* (3), 232-7.

10. Tsai, C.-Y.; Shiau, A.-L.; Chen, S.-Y.; Chen, Y.-H.; Cheng, P.-C.; Chang, M.-Y.; Chen, D.-H.; Chou, C.-H.; Wang, C.-R.; Wu, C.-L., Amelioration of collagen-induced arthritis in rats by nanogold. *Arthritis Rheum* **2007,** *56* (2), 544-54.

11. Kogan, M. J.; Bastus, N. G.; Amigo, R.; Grillo-Bosch, D.; Araya, E.; Turiel, A.; Labarta, A.; Giralt, E.; Puntes, V. F., Nanoparticle-Mediated Local and Remote Manipulation of Protein Aggregation. *Nano Lett.* **2006,** *6* (1), 110-115.

12. Pissuwan, D.; Valenzuela, S. M.; Cortie, M. B., Therapeutic possibilities of plasmonically heated gold nanoparticles. *Trends Biotechnol.* **2006,** *24* (2), 62-67.

13. Pissuwan, D.; Valenzuela, S.; Cortie, M., Gold nanoparticles for photothermal therapeutics. *Mater. Aust.* **2006,** *39* (4), 20.

14. Huang, D.; Liao, F.; Molesa, S.; Redinger, D.; Subramanian, V., Plastic-Compatible Low Resistance Printable Gold Nanoparticle Conductors for Flexible Electronics. *Journal of the Electrochemical Society* **2003,** *150* (7), G412-G417.

15. Porel, S.; Singh, S.; Harsha, S. S.; Rao, D. N.; Radhakrishnan, T. P., Nanoparticle-Embedded Polymer: In Situ Synthesis, Free-Standing Films with Highly Monodisperse Silver Nanoparticles and Optical Limiting. *Chem. Mater.* **2005,** *17* (1), 9-12.

16. Brus, L., Electronic wave functions in semiconductor clusters: experiment and theory. *J. Phys. Chem.* **1986,** *90* (12), 2555-60.

17. Brus, L. E., Electron-electron and electron-hole interactions in small semiconductor crystallites: the size dependence of the lowest excited electronic state. *J. Chem. Phys.* **1984,** *80* (9), 4403-9.

18. Brus, L. E., A simple model for the ionization potential, electron affinity, and aqueous redox potentials of small semiconductor crystallites. *J. Chem. Phys.* **1983,** *79* (11), 5566-71.

19. Kanskaya, L. M.; Kokhanovskii, S. I.; Seisyan, R. P.; Efros, A. L. *Observation in indium antimonide (InSb) of a Wannier-Mott exciton and its quasiunidimensional states*; USSR.: 1982; pp 136-41.

20. Peng, X.; Manna, U.; Yang, W.; Wickham, J.; Scher, E.; Kadavanich, A.; Allvisatos, A. P., Shape control of CdSe nanocrystals. *Nature (London)* **2000,** *404* (6773), 59-61.

21. Peng, X.; Thessing, J., Controlled synthesis of high quality semiconductor nanocrystals. *Struct. Bonding (Berlin, Ger.)* **2005,** *118* (Semiconductor Nanocrystals and Silicate Nanoparticles), 79-119.

22. Peng, Z. A.; Peng, X., Nearly Monodisperse and Shape-Controlled CdSe Nanocrystals via Alternative Routes: Nucleation and Growth. *J. Am. Chem. Soc.* **2002,** *124* (13), 3343-3353.

23. Peng, Z. A.; Peng, X., Formation of high-quality CdTe, CdSe, and CdS nanocrystals using CdO as precursor. *J. Am. Chem. Soc.* **2001,** *123* (1), 183-184.

24. Qu, L.; Peng, X., Control of Photoluminescence Properties of CdSe Nanocrystals in Growth. *J. Am. Chem. Soc.* **2002,** *124* (9), 2049-2055.

25. Kang, I.; Wise, F. W., Electronic structure and optical properties of PbS and PbSe quantum dots. *J. Opt. Soc. Am. B* **1997,** *14* (7), 1632-1646.

26. Murray, C. B.; Sun, S.; Gaschler, W.; Doyle, H.; Betley, T. A.; Kagan, C. R., Colloidal synthesis of nanocrystals and nanocrystal superlattices. *IBM J. Res. Dev.* **2001,** *45* (1), 47-56.

27. Battaglia, D.; Peng, X., Formation of High Quality InP and InAs Nanocrystals in a Noncoordinating Solvent. *Nano Lett.* **2002,** *2* (9), 1027-1030.

28. Micic, O. I.; Sprague, J. R.; Curtis, C. J.; Jones, K. M.; Machol, J. L.; Nozik, A. J.; Giessen, H.; Fluegel, B.; Mohs, G.; Peyghambarian, N., Synthesis and Characterization of InP, GaP, and GaInP2 Quantum Dots. *J. Phys. Chem.* **1995,** *99* (19), 7754-9.

29. Nozik, A. J.; Micic, O. I., Colloidal quantum dots of Group IIIA-VA semiconductors. *MRS Bulletin* **1998,** *23* (2), 24-30.

30. Erwin, S. C.; Zu, L.; Haftel, M. I.; Efros, A. L.; Kennedy, T. A.; Norris, D. J., Doping semiconductor nanocrystals. *Nature (London, United Kingdom)* **2005,** *436* (7047), 91-94.

31. Gan, C.; Xiao, M.; Battaglia, D.; Pradhan, N.; Peng, X., Size dependence of nonlinear optical absorption and refraction of Mn-doped ZnSe nanocrystals. *Applied Physics Letters* **2007,** *91* (20), 201103/1-201103/3.

32. Gan, C.; Zhang, Y.; Battaglia, D.; Peng, X.; Xiao, M., Fluorescence lifetime of Mn-doped ZnSe quantum dots with size dependence. *Applied Physics Letters* **2008,** *92* (24), 241111/1-241111/3.

33. Pradhan, N.; Peng, X., Efficient and Color-Tunable Mn-Doped ZnSe Nanocrystal Emitters: Control of Optical Performance via Greener Synthetic Chemistry. *J. Am. Chem. Soc.* **2007,** *129* (11), 3339-3347.

34. Zhang, Y.; Gan, C.; Muhammad, J.; Battaglia, D.; Peng, X.; Xiao, M., Enhanced Fluorescence Intermittency in Mn-Doped Single ZnSe Quantum Dots. *J. Phys. Chem. C* **2008,** *112* (51), 20200-20205.

35. Pradhan, N.; Goorskey, D.; Thessing, J.; Peng, X., An Alternative of CdSe Nanocrystal Emitters: Pure and Tunable Impurity Emissions in ZnSe Nanocrystals. *J. Am. Chem. Soc.* **2005,** *127* (50), 17586-17587.

36. Schwartz, D. A.; Norberg, N. S.; Nguyen, Q. P.; Parker, J. M.; Gamelin, D. R., Magnetic Quantum Dots: Synthesis, Spectroscopy, and Magnetism of Co2+- and Ni2+-Doped ZnO Nanocrystals. *J. Am. Chem. Soc.* **2003,** *125* (43), 13205-13218.

37. Schwartz, D. A.; Gamelin, D. R., Reversible 300 K ferromagnetic ordering in a diluted magnetic semiconductor. *Adv. Mater. (Weinheim, Ger.)* **2004,** *16* (23-24), 2115-2119.

38. Edwards, P. P.; Porch, A.; Jones, M. O.; Morgan, D. V.; Perks, R. M., Basic materials physics of transparent conducting oxides. *Dalton Trans.* **2004,** (19), 2995-3002.

39. Badeker, K., *Annals of Physics* **1907,** *22* (749).

40. Chopra, K. L.; Major, S.; Pandya, D. K., Transparent conductors - a status review. *Thin Solid Films* **1983,** *102* (1), 1-46.

41. Al-Dahoudi, N.; Aegerter, M. A., Wet Coating Deposition of ITO Coatings on Plastic Substrates. *J. Sol-Gel Sci. Technol.* **2003,** *26* (1/2/3), 693-697.

42. Ulrich Schwarz-Schampera, P. M. H., Bundesanstalt fur Geowissenschaften und Rohstoffe, *Indium: Geology, Mineralogy, and Economics*. Springer: 2002; p 257.

43. Hamberg, I.; Granqvist, C. G., Evaporated tin-doped indium oxide films: basic optical properties and applications to energy-efficient windows. *Journal of Applied Physics* **1986,** *60* (11), R123-R159.

44. geology.com Indium Price Supported by LCD Demand and New Uses for the Metal. http://geology.com/articles/indium.shtml.

45. Buehler, G.; Thoelmann, D.; Feldmann, C., One-pot synthesis of highly conductive indium tin oxide nanocrystals. *Adv. Mater. (Weinheim, Ger.)* **2007,** *19* (17), 2224-2227.

46. Kim, K. Y.; Park, S. B., Preparation and property control of nano-sized indium tin oxide particle. *Mater. Chem. Phys.* **2004,** *86* (1), 210-221.

47. Song, J. E.; Lee, D. K.; Kim, H. W.; Kim, Y. I.; Kang, Y. S., Preparation and characterization of monodispersed indium-tin oxide nanoparticles. *Colloids Surf., A* **2005,** *257-258*, 539-542.

48. Ba, J.; Fattakhova Rohlfing, D.; Feldhoff, A.; Brezesinski, T.; Djerdj, I.; Wark, M.; Niederberger, M., Nonaqueous Synthesis of Uniform Indium Tin Oxide Nanocrystals and Their Electrical Conductivity in Dependence of the Tin Oxide Concentration. *Chem. Mater.* **2006,** *18* (12), 2848-2854.

49. Gupta, L.; Mansingh, A.; Srivastava, P. K., Band gap narrowing and the band structure of tin-doped indium oxide films. *Thin Solid Films* **1989,** *176* (1), 33-44.

50. Bel Hadj Tahar, R.; Ban, T.; Ohya, Y.; Takahashi, Y., Tin doped indium oxide thin films: Electrical properties. *Journal of Applied Physics* **1998,** *83* (5), 2631-2645.

51. Mott, N., On metal-insulator transitions. *Journal of Solid State Chemistry* **1990,** *88* (1), 5-7.

52. Frank, G.; Koestlin, H., Electrical properties and defect model of tin-doped indium oxide layers. *Appl. Phys., [Part] A* **1982,** *A27* (4), 197-206.

53. Omata, T.; Fujiwara, H.; Otsuka-Yao-Matsuo, S.; Ono, N., Electron trapping center and SnO2 -doping mechanism of indium tin oxide. *Appl. Phys. A: Mater. Sci. Process.* **2000,** *71* (6), 609-614.

54. Gonzalez, G. B.; Mason, T. O.; Quintana, J. P.; Warschkow, O.; Ellis, D. E.; Hwang, J. H.; Hodges, J. P.; Jorgensen, J. D., Defect structure studies of bulk and nano-indium-tin oxide. *Journal of Applied Physics* **2004,** *96* (7), 3912-3920.

55. Brewer, S. H.; Franzen, S., Calculation of the electronic and optical properties of indium tin oxide by density functional theory. *Chem. Phys.* **2004,** *300* (1-3), 285-293.

56. Zhou, J. Indium Tin Oxide (ITO) Deposition, Patterning, and Schottky Contact Fabrication. Rochester Institute of Technology, Rochester, 2005.

57. Fan, J. C. C.; Bachner, F. J.; Foley, G. H., Effect of oxygen pressure during deposition on properties of rf-sputtered tin-doped indium oxide films. *Applied Physics Letters* **1977,** *31* (11), 773-5.

58. Sreenivas, K.; Rao, T. S.; Mansingh, A.; Chandra, S., Preparation and characterization of rf sputtered indium tin oxide films. *Journal of Applied Physics* **1985,** *57* (2), 384-92.

59. Szczyrbowski, J.; Dietrich, A.; Hoffmann, H., Optical and electrical properties of RF-sputtered indium-tin oxide films. *Phys. Status Solidi A* **1983,** *78* (1), 243-52.

60. Buchanan, M.; Webb, J. B.; Williams, D. F., The influence of target oxidation and growth-related effects on the electrical properties of reactively sputtered films of tin-doped indium oxide. *Thin Solid Films* **1981,** *80* (4), 373-82.

61. Higuchi, M.; Uekusa, S.; Nakano, R.; Yokogawa, K., Postdeposition annealing influence on sputtered indium tin oxide film characteristics. *Jpn. J. Appl. Phys., Part 1* **1994,** *33* (1A), 302-6.

62. Balasubramanian, N.; Subrahmanyam, A., Effect of substrate temperature on the electrical and optical properties of reactively evaporated indium tin oxide films. *Mater. Sci. Eng., B* **1988,** *B1* (3-4), 279-81.

63. Bregman, J.; Shapira, Y.; Aharoni, H., Effects of oxygen partial pressure during deposition on the properties of ion-beam-sputtered indium-tin oxide thin films. *Journal of Applied Physics* **1990,** *67* (8), 3750-3.

64. Haitjema, H.; Elich, J. J. P., Physical properties of pyrolytically sprayed tin-doped indium oxide coatings. *Thin Solid Films* **1991,** *205* (1), 93-100.

65. Boycheva, S.; Sytchkova, A. K.; Piegari, A., Optical and electrical characterization of r.f. sputtered ITO films developed as art protection coatings. *Thin Solid Films* **2007,** *515* (24), 8474-8478.

66. Drude, P., Electron theory of metals. II. Galvanomagnetic and thermomagnetic effects. *Annalen der Physik (Weinheim, Germany)* **1900,** *3*, 369-402.

67. Coutts, T. J.; Young, D. L.; Li, X., Characterization of transparent conducting oxides. *MRS Bulletin* **2000,** *25* (8), 58-65.

68. Al-Dahoudi, N. Wet Chemical Deposition of Transparent Conducting Coatings Made of Redispersable Crystalline ITO Nanoparticles on Glass and Polymeric Substrates. University of Saarland, Aachen, Germany, 2003.

69. Lu, J. G.; Fujita, S.; Kawaharamura, T.; Nishinaka, H.; Kamada, Y.; Ohshima, T.; Ye, Z. Z.; Zeng, Y. J.; Zhang, Y. Z.; Zhu, L. P.; He, H. P.; Zhao, B. H., Carrier concentration dependence of band gap shift in n-type ZnO:Al films. *Journal of Applied Physics* **2007,** *101* (8), 083705/1-083705/7.

70. Burstein, E., Anomalous optical absorption limit in InSb. *Phys. Rev.* **1954,** *93*, 632-3.

71. Moss, T. S., The interpretation of the properties of indium antimonide. *Proc. Phys. Soc., London* **1954,** *67B*, 775-82.

72. Hamberg, I.; Granqvist, C. G.; Berggren, K. F.; Sernelius, B. E.; Engstroem, L., Band-gap widening in heavily tin-doped indium oxide. *Phys. Rev. B: Condens. Matter* **1984,** *30* (6), 3240-9.

73. Sanon, G.; Rup, R.; Mansingh, A., Band-gap narrowing and band structure in degenerate tin oxide (SnO2) films. *Phys. Rev. B: Condens. Matter* **1991,** *44* (11), 5672-80.

74. Jarzebski, Z. M., Preparation and physical properties of transparent conducting oxide films. *Phys. Status Solidi A* **1982,** *71* (1), 13-41.

75. Qu, Y.; Gessert, T. A.; Ramanathan, K.; Dhere, R. G.; Noufi, R.; Coutts, T. J., Electrical and optical properties of ion beam sputtered aluminum-doped zinc oxide films as a function of film thickness. *Journal of Vacuum Science & Technology, A Vacuum, Surfaces, and Films* **1993,** *11* (4, Pt. 1), 996-1000.

76. Sarkar, A.; Ghosh, S.; Chaudhuri, S.; Pal, A. K., Studies on electron transport properties and the Burstein-Moss shift in indium-doped zinc oxide films. *Thin Solid Films* **1991,** *204* (2), 255-64.

77. Brehme, S.; Fenske, F.; Fuhs, W.; Nebauer, E.; Poschenrieder, M.; Selle, B.; Sieber, I., Free-carrier plasma resonance effects and electron transport in reactively sputtered degenerate ZnO:Al films. *Thin Solid Films* **1999,** *342* (1,2), 167-173.

78. Singh, A. V.; Mehra, R. M.; Yoshida, A.; Wakahara, A., Doping mechanism in aluminum-doped zinc oxide films. *Journal of Applied Physics* **2004,** *95* (7), 3640-3643.

79. Ohhata, Y.; Shinoki, F.; Yoshida, S., Optical properties of r.f. reactive sputtered tin-doped indium trioxide films. *Thin Solid Films* **1979,** *59* (2), 255-61.

80. Nagatomo, T.; Maruta, Y.; Omoto, O., Electrical and optical properties of vacuum-evaporated indium-tin oxide films with high electron mobility. *Thin Solid Films* **1990,** *192* (1), 17-25.

81. Chen, M.; Pei, Z. L.; Wang, X.; Yu, Y. H.; Liu, X. H.; Sun, C.; Wen, L. S., Intrinsic limit of electrical properties of transparent conductive oxide films. *J. Phys. D: Appl. Phys.* **2000,** *33* (20), 2538-2548.

82. Young, D. L.; Coutts, T. J.; Kaydanov, V. I.; Gilmore, A. S.; Mulligan, W. P., Direct measurement of density-of-states effective mass and scattering parameter in transparent conducting oxides using second-order transport phenomena. *Journal of Vacuum Science & Technology, A Vacuum, Surfaces, and Films* **2000,** *18* (6), 2978-2985.

83. Fujiwara, H.; Kondo, M., Effects of carrier concentration on the dielectric function of ZnO:Ga and In2O3:Sn studied by spectroscopic ellipsometry: Analysis of free-carrier and band-edge absorption. *Phys. Rev. B: Condens. Matter* **2005,** *71* (7), 075109/1-075109/10.

84. Wolff, P. A., Theory of the band structure of very degenerate semiconductors. **1962**, 220-6.

85. Heisenberg, W., Über den anschaulichen Inhalt der quantentheoretischen Kinematik und Mechanik. *Zeitschrift für Physik* **1927,** *43*.

86. AllenMcC http://commons.wikimedia.org/wiki/Main_Page.

87. Chintamani Nagesa Ramachandra Rao, P. J. T., and G. U. Kulkami, *Nanocrystals: synthesis, properties, and applications*. Springer: 2007; p 180.

88. Merzbacher, E., *Quantum Mechanics*. John Wiley: 1994.

89. Gaponenko, S. V., *Optical Properties of Semiconductor Nanocrystals*. Cambridge University Press: Cambridge, 1998.

90. Fong, C. Y.; Klein, B. M.; Nelson, J. S., Energy spacing in charging a quantum dot: the effect of the electron-electron interactions. *Modell. Simul. Mater. Sci. Eng.* **1996,** *4* (5), 433-441.

91. Roest, A. L.; Kelly, J. J.; Vanmaekelbergh, D.; Meulenkamp, E. A., Staircase in the electron mobility of a ZnO quantum dot assembly due to shell filling. *Phys. Rev. Lett.* **2002,** *89* (3), 036801/1-036801/4.

92. Roest, A. L.; Kelly, J. J.; Vanmaekelbergh, D., Coulomb blockade of electron transport in a ZnO quantum-dot solid. *Applied Physics Letters* **2003,** *83* (26), 5530-5532.

93. Roest, A. L.; Houtepen, A. J.; Kelly, J. J.; Vanmaekelbergh, D., Electron-conducting quantum-dot solids with ionic charge compensation. *Faraday Discuss.* **2003,** *125*, 55-62.

94. Vanmaekelbergh, D.; Liljeroth, P., Electron-conducting quantum dot solids: novel materials based on colloidal semiconductor nanocrystals. *Chem. Soc. Rev.* **2005,** *34* (4), 299-312.

95. Szymanski, H. A., *IR: Theory and Practice of Infrared Spectroscopy*. Plenum Press: New York, 1964.

96. Ammann, A. A., Inductively coupled plasma mass spectrometry (ICP MS): a versatile tool. *J. Mass Spectrom.* **2007,** *42* (4), 419-427.

97. Cullity, B. D., *Elements of X-ray Diffraction*. Addison-Wesley: Philippines, 1978.

98. Hunter, D. N., Thin-film nanocapacitor and its characterization. *European Journal of Physics* **2007,** *28*.

99. La Mer, V. K.; Dinegar, R. H., Theory, production, and mechanism of formation of monodispersed hydrosols. *J. Am. Chem. Soc.* **1950,** *72*, 4847-54.

100. LaMer, V. K., Kinetics in phase transitions. *J. Ind. Eng. Chem. (Washington, D. C.)* **1952,** *44*, 1270-7.

101. Peng, X.; Wickham, J.; Alivisatos, A. P., Kinetics of II-VI and III-V Colloidal Semiconductor Nanocrystal Growth: "Focusing" of Size Distributions. *J. Am. Chem. Soc.* **1998,** *120* (21), 5343-5344.

102. McGinley, C.; Borchert, H.; Pflughoefft, M.; Al Moussalami, S.; de Castro, A. R. B.; Haase, M.; Weller, H.; Moller, T., Dopant atom distribution and spatial confinement of conduction electrons in Sb-doped SnO2 nanoparticles. *Phys. Rev. B: Condens. Matter* **2001,** *64* (24), 245312/1-245312/9.

103. Murray, C. B.; Kagan, C. R.; Bawendi, M. G., Synthesis and characterization of monodisperse nanocrystals and close-packed nanocrystal assemblies. *Annu. Rev. Mater. Sci.* **2000,** *30*, 545-610.

104. Thessing, J.; Qian, J.; Chen, H.; Pradhan, N.; Peng, X., Interparticle Influence on Size/Size Distribution Evolution of Nanocrystals. *J. Am. Chem. Soc.* **2007,** *129* (10), 2736-2737.

105. Katari, J. E. B.; Colvin, V. L.; Alivisatos, A. P., X-ray Photoelectron Spectroscopy of CdSe Nanocrystals with Applications to Studies of the Nanocrystal Surface. *J. Phys. Chem.* **1994,** *98* (15), 4109-17.

106. Alivisatos, A. P., Semiconductor clusters, nanocrystals, and quantum dots. *Science (Washington, D. C.)* **1996,** *271* (5251), 933-7.

107. Alivisatos, A. P., Perspectives on the physical chemistry of semiconductor nanocrystals. *J. Phys. Chem.* **1996,** *100* (31), 13226-13239.

108. Yu, W. W.; Peng, X., Formation of high-quality CdS and other II-VI semiconductor nanocrystals in noncoordinating solvents: Tunable reactivity of monomers. *Angew. Chem., Int. Ed.* **2002,** *41* (13), 2368-2371.

109. Li, L. S.; Pradhan, N.; Wang, Y.; Peng, X., High Quality ZnSe and ZnS Nanocrystals Formed by Activating Zinc Carboxylate Precursors. *Nano Lett.* **2004,** *4* (11), 2261-2264.

110. Vossmeyer, T.; Katsikas, L.; Giersig, M.; Popovic, I. G.; Diesner, K.; Chemseddine, A.; Eychmueller, A.; Weller, H., CdS Nanoclusters: Synthesis, Characterization, Size Dependent Oscillator Strength, Temperature Shift of the Excitonic Transition Energy, and Reversible Absorbance Shift. *J. Phys. Chem.* **1994,** *98* (31), 7665-73.

111. Dzyaloshinskii, I. E.; Lifshits, E. M.; Pitaevskii, L. P., General theory of the van der Waal's forces. *Usp. Fiz. Nauk* **1961,** *73*, 381-422.

112. Boyd, R. T. M. a. R. N., *Organic Chemistry*. 6th ed.; 1992.

113. Qu, L.; Peng, Z. A.; Peng, X., Alternative Routes toward High Quality CdSe Nanocrystals. *Nano Lett.* **2001,** *1* (6), 333-337.

114. Peng, X., Green chemical approaches toward high-quality semiconductor nanocrystals. *Chem.--Eur. J.* **2002,** *8* (2), 334-339.

115. Pradhan, N.; Battaglia, D. M.; Liu, Y.; Peng, X., Efficient, Stable, Small, and Water-Soluble Doped ZnSe Nanocrystal Emitters as Non-Cadmium Biomedical Labels. *Nano Lett.* **2007,** *7* (2), 312-317.

116. Zhang, Z.; Lu, M.; Xu, H.; Chin, W.-S., Shape-controlled synthesis of zinc oxide: a simple method for the preparation of metal oxide nanocrystals in non-aqueous medium. *Chem.--Eur. J.* **2007,** *13* (2), 632-638.

117. Pinna, N.; Garnweitner, G.; Antonietti, M.; Niederberger, M., Non-aqueous synthesis of high-purity metal oxide nanopowders using an ether elimination process. *Adv. Mater. (Weinheim, Ger.)* **2004,** *16* (23-24), 2196-2200.

118. Zhang, Z.; Zhong, X.; Liu, S.; Li, D.; Han, M., Aminolysis route to monodisperse titania nanorods with tunable aspect ratio. *Angew. Chem., Int. Ed.* **2005,** *44* (22), 3466-3470.

119. Niederberger, M.; Garnweitner, G.; Pinna, N.; Antonietti, M., Nonaqueous and Halide-Free Route to Crystalline BaTiO3, SrTiO3, and (Ba,Sr)TiO3 Nanoparticles via a Mechanism Involving C-C Bond Formation. *J. Am. Chem. Soc.* **2004,** *126* (29), 9120-9126.

120. Jana, N. R.; Chen, Y.; Peng, X., Size- and Shape-Controlled Magnetic (Cr, Mn, Fe, Co, Ni) Oxide Nanocrystals via a Simple and General Approach. *Chem. Mater.* **2004,** *16* (20), 3931-3935.

121. Chen, Y.; Kim, M.; Lian, G.; Johnson, M. B.; Peng, X., Side Reactions in Controlling the Quality, Yield, and Stability of High Quality Colloidal Nanocrystals. *J. Am. Chem. Soc.* **2005,** *127* (38), 13331-13337.

122. Narayanaswamy, A.; Xu, H.; Pradhan, N.; Kim, M.; Peng, X., Formation of Nearly Monodisperse In2O3 Nanodots and Oriented-Attached Nanoflowers: Hydrolysis and Alcoholysis vs Pyrolysis. *J. Am. Chem. Soc.* **2006,** *128* (31), 10310-10319.

123. Peter Vollhardt and Neil E. Schore, t. E., *Organic Chemistry: Structure and Function*. W. H. Freeman & Company: 2007.

124. Mohapatra, S.; Mallick, S. K.; Maiti, T. K.; Ghosh, S. K.; Pramanik, P., Synthesis of highly stable folic acid conjugated magnetite nanoparticles for targeting cancer cells. *Nanotechnology* **2007,** *18* (38), 385102/1-385102/9.

125. Swanson, H. E.; Gilfrich, N. T.; Ugrinic, G. M., Standard x-ray diffraction powder patterns. *Natl. Bur. Stand. Circ. (U. S.)* **1955,** *5* (No. 539), 75 pp.

126. Chen, M.; Feng, Y.-G.; Wang, X.; Li, T.-C.; Zhang, J.-Y.; Qian, D.-J., Silver nanoparticles capped by oleylamine: Formation, growth, and self-organization. *Langmuir* **2007,** *23* (10), 5296-5304.

127. Shukla, N.; Liu, C.; Jones, P. M.; Weller, D., FTIR study of surfactant bonding to FePt nanoparticles. *J. Magn. Magn. Mater.* **2003,** *266* (1-2), 178-184.

128. Crouch, J. D. J. I. a. S. R., *Spectrochemical Analysis*. Prentice Hall: New Jersey, 1988.

129. Qu, L.; Yu, W. W.; Peng, X., In Situ Observation of the Nucleation and Growth of CdSe Nanocrystals. *Nano Lett.* **2004,** *4* (3), 465-469.

130. Caglar, Y.; Ilican, S.; Caglar, M.; Yakuphanoglu, F., Effects of In, Al and Sn dopants on the structural and optical properties of ZnO thin films. *Spectrochim. Acta, Part A* **2007,** *67A* (3-4), 1113-1119.

131. Weijtens, C. H. L.; Van Loon, P. A. C., Influence of annealing on the optical properties of indium tin oxide. *Thin Solid Films* **1991,** *196* (1), 1-10.

132. Kormann, C.; Bahnemann, D. W.; Hoffmann, M. R., Preparation and characterization of quantum-size titanium dioxide. *J. Phys. Chem.* **1988,** *92* (18), 5196-201.

133. Quang, N. H.; Truc, N. T.; Niquet, Y.-M., Tight-binding versus effective mass approximation calculation of electronic structures of semiconductor nanocrystals and nanowires. *Comput. Mater. Sci.* **2008,** *44* (1), 21-25.

134. Parent, P.; Dexpert, H.; Tourillon, G.; Grimal, J. M., Structural study of tin-doped indium oxide thin films using x-ray absorption spectroscopy and x-ray diffraction. II. Tin environment. *Journal of the Electrochemical Society* **1992,** *139* (1), 282-5.

135. Parent, P.; Dexpert, H.; Tourillon, G.; Grimal, J. M., Structural study of tin-doped indium oxide thin films using x-ray absorption spectroscopy and x-ray diffraction. I. Description of the indium site. *Journal of the Electrochemical Society* **1992,** *139* (1), 276-81.

136. Nadaud, N.; Lequeux, N.; Nanot, M.; Jove, J.; Roisnel, T., Structural studies of tin-doped indium oxide (ITO) and In4Sn3O12. *Journal of Solid State Chemistry* **1998,** *135* (1), 140-148.

137. Gonzalez, G. B.; Cohen, J. B.; Hwang, J.-H.; Mason, T. O.; Hodges, J. P.; Jorgensen, J. D., Neutron diffraction study on the defect structure of indium-tin-oxide. *Journal of Applied Physics* **2001,** *89* (5), 2550-2555.

138. Gonzalez, G. B.; Cohen, J. B.; Hwang, J.-H.; Mason, T. O.; Hodges, J. P.; Jorgensen, J. D., Defect structure of indium tin oxide and its relationship to conductivity. *Adv. Sci. Technol. (Faenza, Italy)* **2000,** *29* (Mass and Charge Transport in Inorganic Materials, Part A), 137-144.

139. Guzelian, A. A.; Katari, J. E. B.; Kadavanich, A. V.; Banin, U.; Hamad, K.; Juban, E.; Alivisatos, A. P.; Wolters, R. H.; Arnold, C. C.; Heath, J. R., Synthesis of Size-Selected, Surface-Passivated InP Nanocrystals. *J. Phys. Chem.* **1996,** *100* (17), 7212-19.

140. Nutz, T.; Felde, U. z.; Haase, M., Wet-chemical synthesis of doped nanoparticles: Blue-colored colloids of n-doped SnO2:Sb. *J. Chem. Phys.* **1999,** *110* (24), 12142-12150.

141. Kelekanjeri, V. S. K. G.; Gerhardt, R. A., A closed-form solution for the computation of geometric correction factors for four-point resistivity measurements on cylindrical specimens. *Meas. Sci. Technol.* **2008,** *19* (2), 025701/1-025701/12.

142. Rothen-Rutishauser, B.; Grass, R. N.; Blank, F.; Limbach, L. K.; Muhlfeld, C.; Brandenberger, C.; Raemy, D. O.; Gehr, P.; Stark, W. J., Direct Combination of Nanoparticle Fabrication and Exposure to Lung Cell Cultures in a Closed Setup as a Method To Simulate Accidental Nanoparticle Exposure of Humans. *Environ. Sci. Technol.* **2009,** *43* (7), 2634-2640.

143. Mominuzzaman, S. M.; Krishna, K. M.; Soga, T.; Jimbo, T.; Umeno, M., Optical absorption and electrical conductivity of amorphous carbon thin films from camphor: a natural source. *Jpn. J. Appl. Phys., Part 1* **1999,** *38* (2A), 658-663.

144. Jayakumar, O. D.; Gopalakrishnan, I. K.; Kadam, R. M.; Vinu, A.; Asthana, A.; Tyagi, A. K., Magnetization and structural studies of Mn doped ZnO nanoparticles: Prepared by reverse micelle method. *J. Cryst. Growth* **2007,** *300* (2), 358-363.

145. Xue, H. T.; Zhao, P. Q., Synthesis and magnetic properties from Mn-doped CdS/SiO2 core-shell nanocrystals. *J. Phys. D: Appl. Phys.* **2009,** *42* (1), 015402/1-015402/5.

146. Norris, D. J.; Efros, A. L.; Erwin, S. C., Doped nanocrystals. *Science (Washington, DC, United States)* **2008,** *319* (5871), 1776-1779.

147. Choi, S.-I.; Nam, K. M.; Park, B. K.; Seo, W. S.; Park, J. T., Preparation and Optical Properties of Colloidal, Monodisperse, and Highly Crystalline ITO Nanoparticles. *Chem. Mater.* **2008,** *20* (8), 2609-2611.